Plasma Diagnostics for Non–Standard Supernova Remnants in the Galactic Center Region

— Origin of Recombining Plasma and Missing Branch of SNR Evolution —

Makoto Sawada

Department of Physics, Graduate School of Science, Kyoto University
Kitashirakawa Oiwake-cho, Sakyo-ku, Kyoto, 606-8502, Japan
sawada@cr.scphys.kyoto-u.ac.jp

This thesis was submitted to the Department of Physics,
Graduate School of Science, Kyoto University
on January 5 2011
in partial fulfillment of the requirements
for the degree of Doctor of Philosophy in physics.

Abstract

The standard picture of hot plasmas in supernova remnants (SNRs) is described by the shock heating and following ionization and recombination processes. This standard scenario and the observational results of SNRs predict that the plasmas have shell-like morphologies and ionization dominant states. This thesis is intended to explore new evidence in the thermal structure of SNR plasmas, a missing branch in SNR evolution. For this purpose, we investigate the thermal plasmas for three non–shell-like SNRs in the Galactic center (GC) region. One of the SNRs, G 1.2–0.0, has peculiar morphology both in the X-ray and radio bands, but the X-ray spectrum is thermal origin. Another SNR G 357.7–0.1 has jet-induced plasmas; twin thermal plasmas are found in the both ends of the spiral radio structures. The other SNR, W 28 is an archetype of mixed-morphology SNRs (MM SNRs); the thermal X-rays are found in the central region surrounded by non-thermal radio shells.

G 1.2–0.0 is a new X-ray source in the vicinity of the Sagittarius D (Sgr D) H II region discovered by the GC mapping project. The X-rays are found from the north of the extended area of the H II region. Unlike the H II region, the radio emission is found to have non-thermal origin. The X-ray spectra are characterized by emission lines from highly ionized atoms, and fitted with optically thin thermal plasma models with enhanced abundances of heavy elements. The interstellar absorption is consistent with the object being in the GC distance. The thermal X-rays and non-thermal radio coincide in position with the size of $\sim$10 pc, and hence this is likely to be a single source, a new SNR in the GC region. The origin and the dynamics of the SNR are not clear but at least far from those for the standard SNRs. The thermal structure of the SNR plasma is found to be either a collisional ionization equilibrium (CIE) plasma or a recombining plasma (RP).

G 357.7–0.1 is a mysterious radio source with a bright "head" and faint "tail", both are connected by multi-spiral structures, and hence called the Tornado nebula. We discovered two diffuse X-ray sources at the head and tail of Tornado. Emission lines from highly ionized atoms are found in the spectra, which are fitted with an optically thin thermal plasma model. The X-ray morphologies, plasma temperatures, interstellar absorptions, and fluxes of these two sources are very similar to each other. The distances are estimated from the X-ray absorptions and are similar to that of Tornado. Thus, the X-ray sources are twin thermal plasmas associated to Tornado. We interpret the origin of the X-ray sources to be, unlike the standard SNRs, due to shock excitation of bipolar outflows from an equatorial supernova explosion of a massive star. The thermal structure of the SNR plasma is found to be either a CIE or an ionizing plasma.

W 28 is a MM SNR in the GC region. The X-ray emission is very bright with the spectra exhibiting emission lines from highly ionized atoms. Optically thin thermal plasma in CIE, either one-temperature or multi-temperature model failed to reproduce the data with line-like

and bump-like residuals at Si Lymanα energy and at 2.4–5.0 keV, respectively. The bumps probably correspond to radiative recombination continua from He-like Si and S. Simple recombining plasma model nicely fit the bump structures, but failed to fit low energy bands. The full-band spectra can be fitted with a multi-ionization temperature plasma with a common electron temperature.

All of the three non-standard SNRs have different and distinct nature. Among them, only the archetype MM SNR W 28 exhibits a clear RP. Since the standard SNRs cannot produce RP, we further examine the RP structure of W 28. W 28 is found to have different ionization temperatures among elements: The values for Si and S are higher than those for the lighter (Ne and Mg) and the heavier (Fe) elements. The multi-ionization temperatures are interpreted as elemental difference of ionization and recombination timescales. The spatially resolved analysis found the radial decreases both in the ionization and electron temperatures. These results are naturally explained as follows. The plasma is shock-heated to high temperature, and then electron temperature quickly drops so that recombining process is now going on. As one plausible scenario, we propose a rarefaction model: the plasma breaks-out from dense circum-stellar medium into a tenuous interstellar space.

Contents

List of Figures

List of Tables

Chapter 1

Introduction

The universe is full of hot plasmas in different spatial scales. They are, for example, supernova remnants (SNRs), massive star forming regions, superbubbles, galaxy winds, and intergalactic medium. Most of these plasmas are originated from supernova (SN) explosions, which are the major source of energy and heavy metals in our universe. The hot plasma emits X-rays and hence the study of the SNR plasmas in the X-ray band is essential to understand the physical process of the plasma formation and its fates on the chemical composition, hot environments, and the Galactic structure as a whole.

The standard evolution of thermal plasmas in SNRs is a dynamical time sequence of shock-heated gas. At first, a large fraction of the expanding velocity is converted into the random velocity (thermal energy). The shock-heated temperature is proportional to the mass of the plasma particles (electrons and ions); the ion temperature is more than 1000 times higher than the electron temperature (hereafter, $T_{\rm e}$). Subsequently, the energy of ions is transferred to the electrons, and hence $T_{\rm e}$ gradually increases. Then the high temperature electrons slowly ionize the ions to higher ionization states. Here we define the ionization temperature ($T_{\rm z}$) as a parameter to represent populations of ionization states; $T_{\rm z}$ is equal to $T_{\rm e}$ in collisional ionization equilibrium (CIE).

For isolated SNe in undisturbed and uniform environments, this sequence produces shell-like morphology in both the X-ray and radio bands. Since the typical timescale of ionization in SNR plasmas (density is $\sim$1 cm^{-3}) is 10^{12-13} s (Smith & Hughes 2010), the X-rays are owing to ionization dominant plasmas. In fact, most of the shell-like SNRs in the young-intermediate ages have lower $T_{\rm z}$ than $T_{\rm e}$, which is called an under-ionized or ionizing plasma, where ionization dominates over recombination (e.g. Kinugasa & Tsunemi 1999). We call these SNRs as the standard SNRs.

The SN environments are not always as simple as those assumed in the standard evolu-

tionary scenario. SNe occur predominantly in the star forming regions, where the SNe may interplay with molecular clouds, H II regions and high energy radiation fields due to massive stars, and cosmic ray particles. These interaction would largely modify the standard scenario of the SNR formation and evolution.

Recent studies with the X-ray Imaging Spectrometer (XIS) onboard Suzaku have discovered strong radiative recombination continua (RRCs) in the X-ray spectra of three SNRs, IC 443, W 49B, and G 359.1–0.5 (Yamaguchi et al. 2009; Ozawa et al. 2009b; Ohnishi et al. 2011). These strong RRCs appear when the recombination process dominates over the ionization process (recombining plasma: RP). In fact, the X-ray spectra of these SNRs can be fit by neither CIE plasma, ionizing plasma, nor any combination of them. Detailed spectroscopic analysis with the RP code revealed that T_z of these SNRs are 1.5–3 times higher than T_e.

These SNRs are classified to be mixed-morphology SNRs (MM SNRs: Rho & Petre 1998), which have a radio shell with centrally-filled thermal X-rays. Together with the RP, this morphology is beyond the evolution scheme of the standard SNRs, Thus the RP may be a key to investigate a possible missing branch in the SNR evolution.

All of the three MM SNRs are associated with shock-exited molecular clouds and GeV/TeV γ-ray emission. Generally, MM SNRs are often found in the disk and the central region in our Galaxy, where the most active regions in star formation. Therefore other non-standard SNRs, not only MM SNRs, may be also found from these regions.

In order to investigate the new scenario of the evolution of non-standard SNRs, we searched for the non-standard SNRs in the Galactic center (GC) mapping and the RP survey projects, and then study three non-standard SNRs, a newly identified SNR in the Sagittarius D (Sgr D: G 1.2–0.0), the Tornado nebula (G 357.7–0.1), and a MM SNR W 28 .

This thesis is organized as follows. The review of the standard SNRs and non-standard SNRs are given in chapter 2. Chapters 3 and 4 are devoted for the structural and thermal evolution of SNR plasmas, respectively. Summary on thermal X-ray emission from SNRs is also given in chapter 4. The instruments used in this study are described in chapter 5. The observations, analyses and brief pictures of the three SNRs are given in chapters 6, 7, and 8. Discussion for the recombination dominant plasma in W 28 based on the detailed plasma diagnostics are given in chapter 9 together with proposal of a possible missing branch of evolutionary scenario. Chapter 10 is the conclusion of this thesis.

Throughout this thesis, we respectively use east and north to indicate the positive direction in the Galactic longitude and latitude, adopt 8 kpc for the distance of the GC, and give values of statistical uncertainties at the 1-σ confidence interval, otherwise noticed.

Chapter 2

Standard and Non-Standard SNRs

Contents

2.1 Standard SNRs

About 300 SNRs have been discovered in our Galaxy (Green 2009). Most of them are first identified in the radio band. Among them, more than ∼100 have been detected so far in the X-ray band.

SNRs have been categorized into three classes based on the radio morphology: shell-like SNRs, Plerions, and composites. The shell-like SNRs have limb-brightened structure while the Plerions have centrally-peaked structure. The composite SNRs have both limb-brightened and centrally-peaked radio emission. Although the radio emission of all these SNRs is due to synchrotron radiation from non-thermal electrons, the origin of the accelerated electrons is different among the classes: limb-brightened emission is because of the electrons accelerated by the blast wave of the SN explosion, while the filled-center emission is due to the electrons powered by central pulsars. The latter is now broadly known as "pulsar-wind nebulae" (PWNe).

The three classes respectively have the similar morphology between radio and X-rays but have the different X-ray natures (table 2.1). Most of shell-like SNRs have thermal X-ray emission from hot plasmas formed by shock-wave heating[1], while the Plerions have non-thermal synchrotron X-ray emission from PWNe. We hereafter call these three classes (shell-like SNRs, Plerions, and composites) "the standard SNRs". In this thesis, we focus on thermal plasmas in SNRs. Thus, "the standard SNR plasmas" indicates the shell-like SNRs.

The standard evolution of thermal plasmas in SNRs has been established by theoretical and observational studies of isolated remnants in the undisturbed, uniform environments. It is a dynamical sequence from shock heating to thermal equilibrium (reviewed in the following chapters 3 and 4). Here, we briefly summarize the characteristics of the standard SNR plasmas based on their formation/evolution mechanism.

The hot plasmas in SNRs are formed by the shock heating of SN blast waves. Hence,

[1]Some of the shell-like SNRs, young SNRs in particular, also emit non-thermal synchrotron X-rays due to very energetic electrons.

Table 2.1—: Properties of the standard SNRs.

Class	Morphology	X-ray nature
Shell-like	limb brightened	thermal∗
Plerions	centrally peaked	non-thermal
Composites	central peak + limb	non-thermal (center) + thermal∗ (limb)

∗ Some of shell-like SNRs also emit non-thermal X-rays.

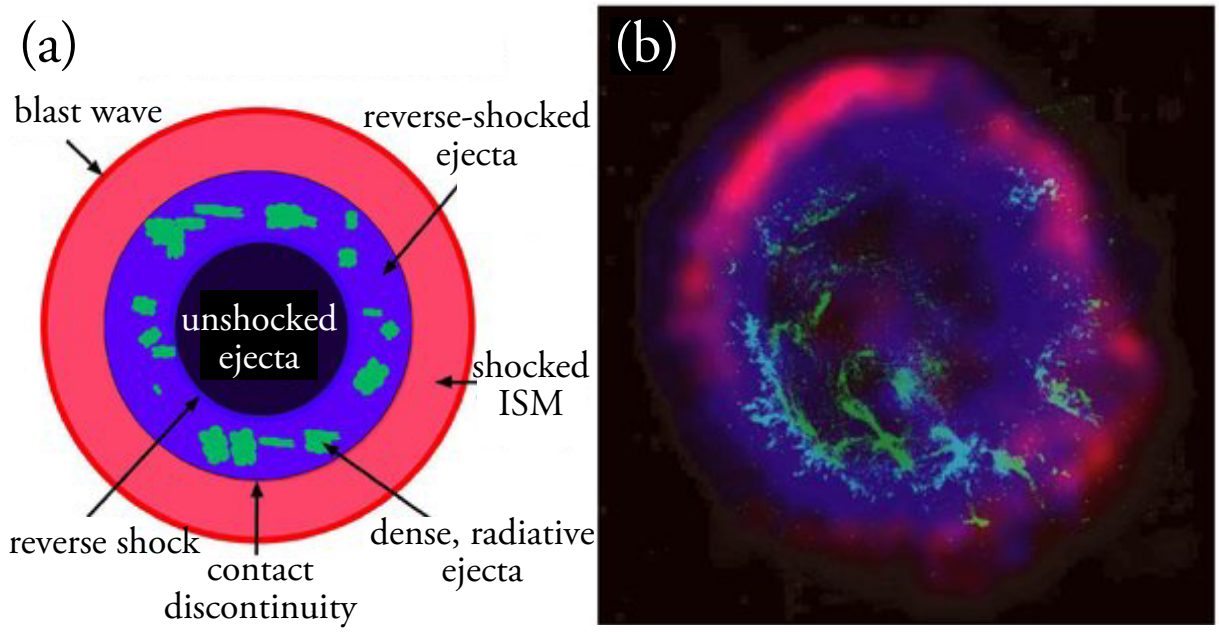

Fig. 2.1.—: Shell structure of standard SNR plasmas (Sandstrom et al. 2009): (a) a schematic view of cross section of a standard shell-like SNR and (b) a composite image of the shell-like SNR 1E 0102–72 in the Small Magellanic Cloud with the 6 cm radio continuum in red, the optical [O III] line emission in green, and the 0.6–3.0 keV X-ray emission in blue.

the X-ray emission is believed to have limb-brightened structures along the expanding blast waves (figure 2.1). In fact, many X-ray–bright SNRs detected by early X-ray surveys such as Cassiopeia A and Tycho's SNR have shell-like morphologies both in the X-ray and radio bands.

In hot plasmas, the transfer of energy occurs to achieve thermal equilibrium. Just after the shock heating, the thermal energies of particles are proportional to their masses. Thus, protons have most of thermal energy of an SNR at this phase. The energy is gradually transferred to electrons due to Coulomb collisions to reach equipartition. Then, the heated electrons start to ionize atoms. Since the ionization states is very low at this stage, the ionization process dominates over the recombination process. This ionization-dominant phase lasts until the CIE is reached. We call the thermal plasma in the transitional phase "ionizing plasmas". Actually, the observed X-ray spectra of shell-like SNRs have been well reproduced as ionizing plasmas (e.g. Kinugasa & Tsunemi 1999).

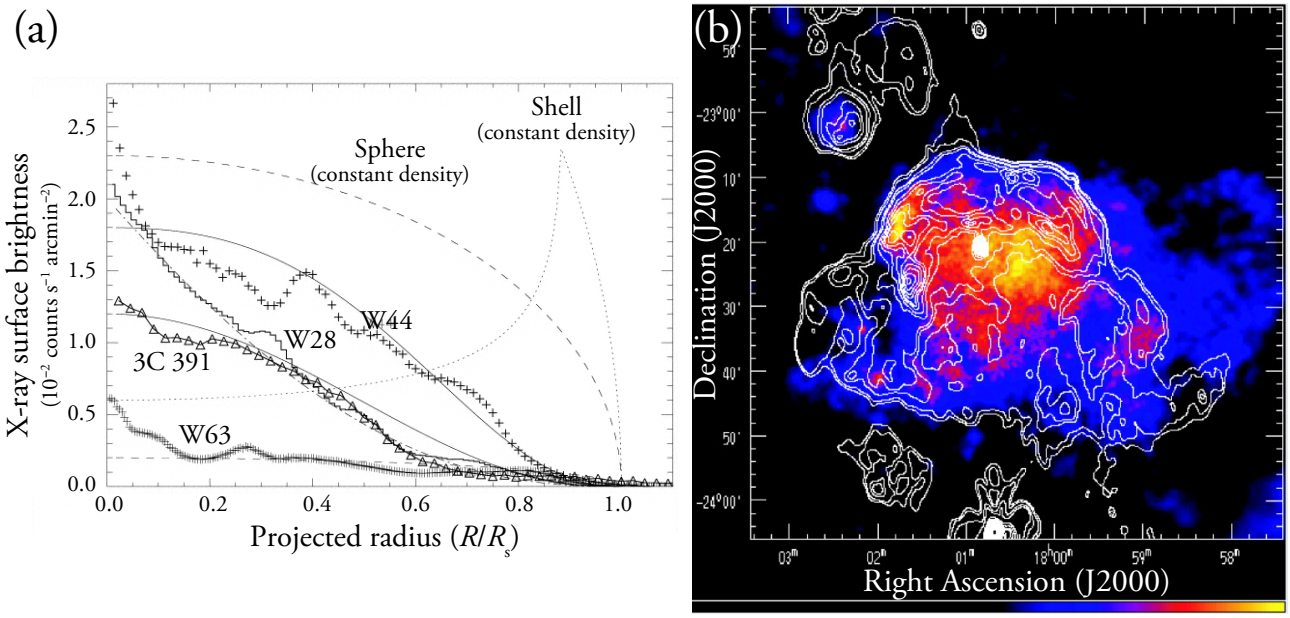

Fig. 2.2.—: Structure of MM SNRs. (a) X-ray surface brightness profiles of the MM SNRs W 44, 3C 391, W 28, and W 63 with ROSAT. Model profiles for various density distributions are also plotted: a Sedov shell, a sphere with a constant density, and the best distributions for each remnant. The plot was made by Rho & Petre (1998). (b) A composite image of the MM SNR W 28 (Rho & Borkowski 2002). The X-ray and radio emission is shown in color and white contours, respectively.

2.2 Non-Standard SNRs

The X-ray surveys during recent decades have drastically increased the number of X-ray emitting SNRs. One of the most remarkable results is that more than half of the SNR plasmas does not show shell-like structures; the X-ray emission is irregularly distributed inside the radio structure. They are also clearly distinguished from Plerions and composites by the the thermal origin of the X-ray emission. Hence, the unique structures of these "non-standard" SNRs cannot be categorized into any known class of the standard SNRs.

Rho & Petre (1998) pointed out that some of these non-standard SNRs have a common appearance: centrally-peaked X-ray structure filling inside the complete radio shell. These remnants are named "mixed-morphology" SNRs (MM SNRs). Figure 2.2 shows the difference in the X-ray morphology between MM SNRs and the standard shell-like SNR. The authors listed the possible 19 members of the MM SNRs, although some of them have irregular shapes.

2.3 Galactic Distribution and Environments of SNRs

The trials to establish the nature of the non-standard SNRs have been made. Rho & Petre (1998) investigated the Galactic distribution of SNRs for each classes (shell-like, Plerionic, composite, and non-standard SNRs). They found that the mean Galactic latitude for 15 non-standard SNRs, 9 composites, 12 shell-like, and 6 Plerionic SNRs are $1^\circ.92 \pm 0^\circ.17$, $1^\circ.42 \pm 0^\circ.08$, $5^\circ.0 \pm 0^\circ.25$, and $2^\circ.07 \pm 0^\circ.25$, respectively. The scale height of the non-standard SNRs is much larger than that of shell-like SNRs. This trend may indicate the possible influence of the environments on the formation of the non-standard SNRs. Star formation in a galaxy is much active in its inner-disk and central region, where the environment is complex and far from that assumed in the standard evolutionary scenario which produces shell-like SNRs. Based on the latest SNR catalog by Green (2009), we plot the update version of the Galactic SNR distribution (but for only non-standard SNRs and shell-like SNRs) in figure 2.3. The smaller mean distance from the Galactic plane for the non-standard SNRs is confirmed with this latest datasets ($1^\circ.3$ for non-standards and $4^\circ.0$ for standard shell-like SNRs).

Interplay with pre-existing circumstellar matter (CSM), rarefied H II regions, ambient molecular clouds, high energy radiation fields, and cosmic ray particles would affect the formation and the evolution of SNR plasmas there. In fact, spatial correlations of the non-standard SNRs with molecular clouds (Rho & Petre 1998; Yusef-Zadeh et al. 2003a; McDonnell et al. 2008; Jiang et al. 2010), H II regions (Goudis 1976; Koo et al. 2002; Brogan et al. 2006), and γ-ray sources (Hewitt et al. 2009; Jiang et al. 2010) have been pointed out so far.

The concentration of the non-standard SNRs is similar to those of Plerionic and composites. This may also indicate their massive progenitors. The massive stars are formed in the star-forming complex in the Galactic disk and explode near the birth region because their lives ($\sim$ a few Myr) are too short to escape far from their natal clouds.

2.4 Plasma Structure of Non-Standard SNRs

The plasma structures of the non-standard SNRs have also been investigated. Kawasaki et al. (2002, 2005) studied the difference in the X-ray spectra between MM SNRs and shell-like SNRs using the ASCA satellite. The authors found that the ionization states of MM SNRs are systematically higher than those of shell-like SNRs. The thermal structure of MM SNRs can be well described as nearly CIE plasmas while that of shell-like SNRs is of ionizing plasmas. Furthermore, they found that the two MM SNRs, IC 443 and W 49B, have recombining plasmas — the reversed state of ionizing plasmas — the ions are over-ionized and thus the recombination process dominates over the ionization. However, these discoveries were not confirmed by

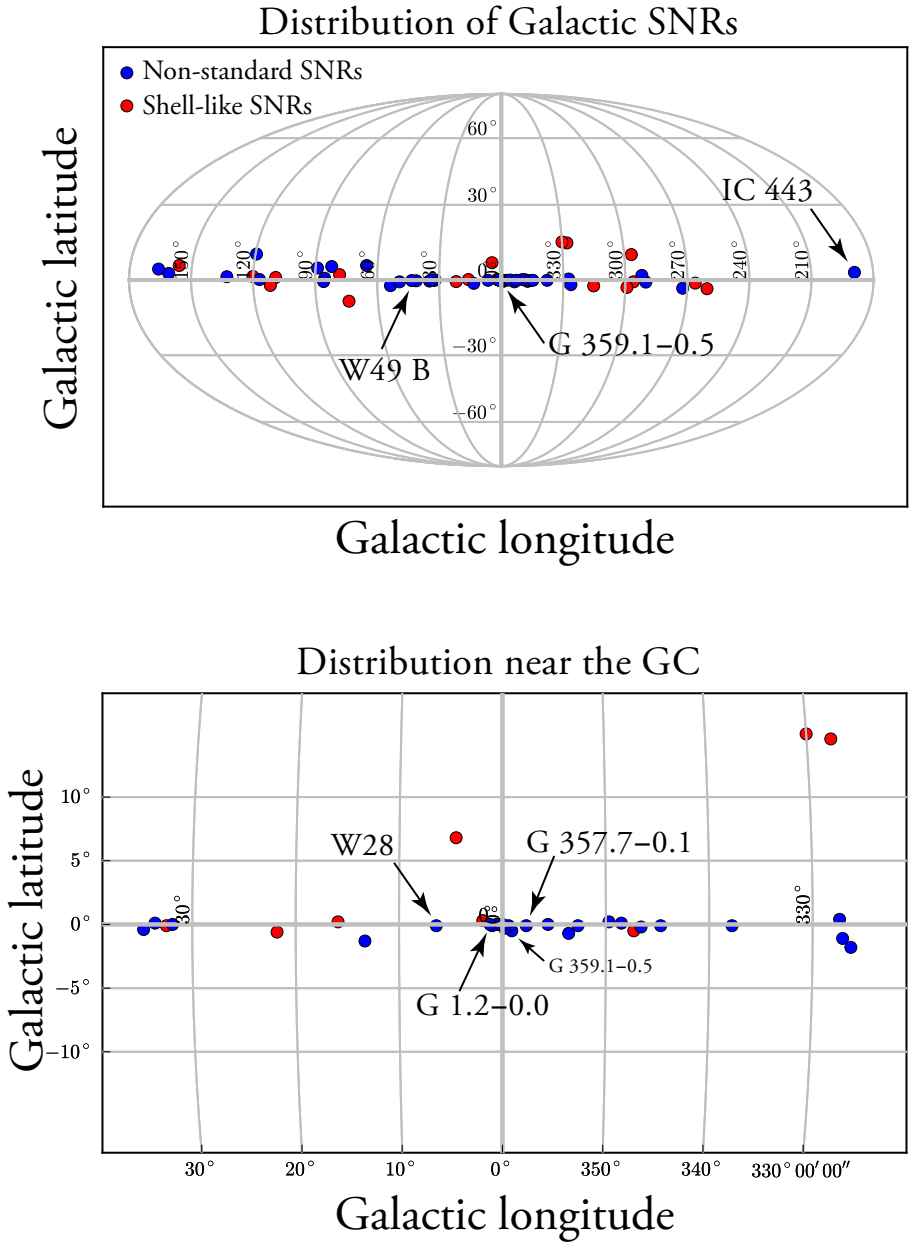

Fig. 2.3.—: Distribution of Galactic SNRs. 43 non-standard SNRs and 21 shell-like SNRs are plotted. Their positions are taken from Green (2009) and references therein. The recent results by the Suzaku GC mapping ($|l| < 2°$) are also taken into account to compensate the information (SNRs in Sgr C: Tsuru et al. 2009, Sgr A: Mori et al. 2008, Sgr B1: Nobukawa et al. 2008, Sgr B2: Koyama et al. 2007b, Sgr D: Sawada et al. 2009). The location of the three known SNRs which exhibit recombining plasmas and our three targets are shown with arrows.

the follow-up observations with XMM-Newton (Troja et al. 2008; Miceli et al. 2006).

Recent studies with the XIS onboard Suzaku have discovered bump-like features in the spectra of the three Galactic MM SNRs, IC 443, W 49B, and G 359.1–0.5 (Yamaguchi et al. 2009; Ozawa et al. 2009b; Ohnishi et al. 2011). The authors concluded that these features are due to strong RRCs, which is clear evidence of recombining plasmas. Such plasmas are beyond the scheme of the standard scenario. Thus, there must be a missing branch of the SNR evolution. All of the SNRs where the recombining plasma have been discovered so far are associated with shocked molecular clouds and GeV/TeV γ-ray emission.

Chapter 3

Dynamical Evolution of SNRs

Contents

SNRs are formed by shock interaction of supersonically expanding ejecta with the outer CSM and interstellar medium (ISM). The gas is compressed and heated by the shock waves and obtains a high temperature of 10^{6-8} K (0.1–10 keV), which leads an X-ray emission. We here describe the dynamical evolution of standard SNR plasmas.

The dynamical evolution of SNRs can be divided into several phases. Their conditions are mainly determined by the ratio between the mass of the ejecta ($M_{\rm Ej}$) and that of the swept-up ISM ($M_{\rm ISM}$). Here, we assume uniform density for the ambient ISM. The detailed descriptions are shown in Truelove & McKee (1999) for the young stages (from free expansion phase through Sedov phase) and Cioffi et al. (1988) for the evolved stage (radiative cooling phase).

3.1 Free Expansion Phase

In the very initial phase, the ejecta expand without deceleration since $M_{\rm ISM}$ is negligible compared to $M_{\rm Ej}$. SN 1987A in the Large Magellanic Cloud is believed to be in this phase.

The expansion velocity ($\sim 10^4$ km s^{-1}) is much larger than the speed of sound in the ambient gas (~ 10 km s^{-1}), and hence shock wave (blast wave) precedes the ejecta. Since most of the explosion energy (E) is released kinetically (only a few percent of the energy converted into thermal energy), the expansion velocity ($v_{\rm s}$) and the radius ($R_{\rm s}$) of the shock front can be respectively expressed by

$$v_{\rm s} = \sqrt{\frac{2E}{M_{\rm Ej}}} = 8.5 \times 10^8 \left(\frac{E}{10^{51}\ {\rm erg}}\right)^{1/2} \left(\frac{M_{\rm Ej}}{1.4\ M_\odot}\right)^{-1/2}\ {\rm cm\ s^{-1}}\ , \tag{3.1}$$

$$R_{\rm s} = v_{\rm s} t\ , \tag{3.2}$$

where t is the elapsed time after the SN explosion. The mass of the ISM swept-up by the blast wave is described as

$$M_{\rm ISM} = \frac{4}{3}\pi R_{\rm s}^3 \mu m_{\rm H} n_0\ , \tag{3.3}$$

where μ, $m_{\rm H}$, and n_0 are mean atomic weight with chemical abundance of solar values, mass of hydrogen atom, and hydrogen number density of the ISM, respectively. Since the free expansion phase continues until that $M_{\rm ISM}$ becomes comparable to $M_{\rm Ej}$, the timescale can be estimated from equation 3.1, 3.2, and 3.3 to be

$$t \sim 2.5 \times 10^2 \left(\frac{E}{10^{51}\ {\rm erg}}\right)^{-1/2} \left(\frac{M_{\rm Ej}}{1.4\ M_\odot}\right)^{5/6} \left(\frac{\mu}{1.4}\right)^{-1/3} \left(\frac{n_0}{1\ {\rm cm^{-3}}}\right)^{-1/3}\ {\rm yr}\ . \tag{3.4}$$

Therefore, this phase typically continues for a few 100 yr, although the timescale can be differ depending on the ambient density.

3.2 Adiabatic Phase

When $M_{\rm ISM}$ becomes much larger than $M_{\rm Ej}$, $M_{\rm ISM} \gtrsim 10 M_{\rm Ej}$ for example, the blast wave is decelerated by the swept-up ISM. However, energy loss via radiation is still negligible compared with its initial energy. Therefore, the SNR expands adiabatically. In this stage, the time evolution of the shock can be approximated with that generated by a point explosion in a uniform medium, which is well explained by a self-similar solution derived by Sedov (1959). Thus, this phase is also called "Sedov phase". The structural evolution can be characterized only by two parameters, E and n_0. The radius ($R_{\rm s}$) and velocity ($v_{\rm s}$) of the blast wave, and the mean temperature just behind the shock front ($T_{\rm s}$) are written as

$$R_{\rm s} = 4 \times 10^{19} \left(\frac{t}{10^4 \text{ yr}} \right)^{2/5} \left(\frac{E}{10^{51} \text{ erg}} \right)^{1/5} \left(\frac{n_0}{1 \text{ cm}^{-3}} \right)^{-1/5} \text{ cm} \tag{3.5}$$

$$v_{\rm s} = \frac{dR_{\rm s}}{dt} = 5 \times 10^7 \left(\frac{t}{10^4 \text{ yr}} \right)^{-3/5} \left(\frac{E}{10^{51} \text{ erg}} \right)^{1/5} \left(\frac{n_0}{1 \text{ cm}^{-3}} \right)^{-1/5} \text{ cm s}^{-1} \tag{3.6}$$

$$T_{\rm s} = 3 \times 10^6 \left(\frac{t}{10^4 \text{ yr}} \right)^{-6/5} \left(\frac{E}{10^{51} \text{ erg}} \right)^{2/5} \left(\frac{n_0}{1 \text{ cm}^{-3}} \right)^{-2/5} \text{ K} . \tag{3.7}$$

In this phase, the density of the swept-up ISM is much higher than that of the ejecta, and hence X-ray emission is dominated by the ISM. Therefore, we can determine $T_{\rm s}$ and n_0 from an X-ray spectrum of the SNR. If the distance to the SNR is known, $R_{\rm s}$ is also determined observationally. Then, the age of the SNR (t) and the explosion energy (E) can be derived according to equation 3.5 and 3.7.

The Sedov phase continues for a few 10,000 yr. Until the end of this phase, $\sim 70\%$ of the initial explosion energy is converted into thermal energy of swept-up ISM (Chevalier 1974).

3.3 Radiative Cooling Phase

In the Sedov phase, the temperature behind the shock ($T_{\rm s}$) decreases with time, according to equation 3.7. Then, the cooling rate gradually increases, and hence the evolution is no longer adiabatic.

As shown in figure 3.1, when the temperature drops to about a few $\times 10^5$ K, electrons efficiently recombine with the heavy elements such as carbon and oxygen which are dominant in ISM of solar abundance. In this phase, the gas radiates ultraviolet line emission efficiently. Since the pressure in the shell becomes lower as the temperature decreases, the shell materials are further compressed, and cool more rapidly. Hence a dense shell is formed, while the interior

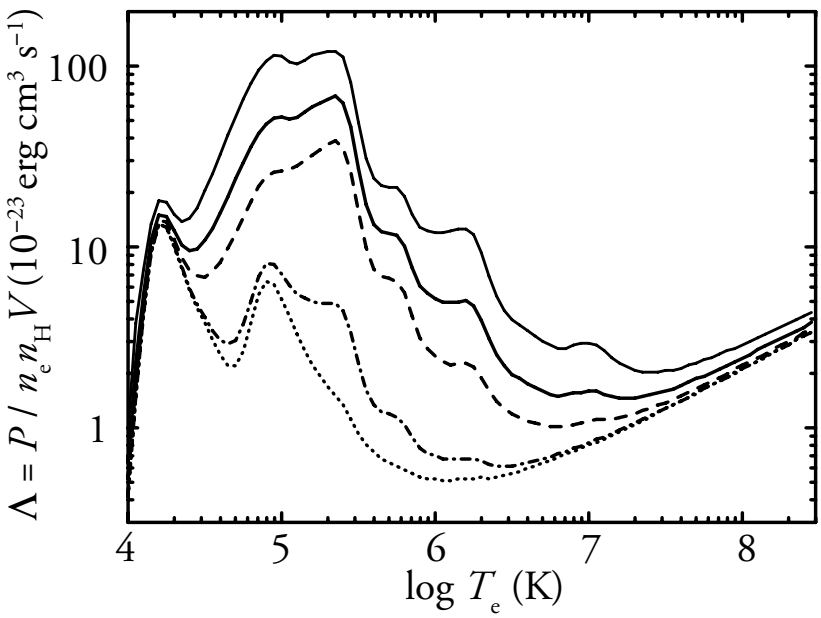

Fig. 3.1.—: Cooling coefficient for an optically thin thermal plasma (Sutherland & Dopita 1993). Curves with 1, 0.3, 0.1, 0.01, and 0.001 times solar abundances are shown from top to bottom as a function of plasma temperature.

is still hot and expands adiabatically. The shell is driven by the pressure of the internal gas according to PV^γ = const., where P and V are the mean pressure and the volume of the internal gas respectively, and γ is the specific heat ratio ($= C_p/C_V$). The value of γ is 5/3 for the non-relativistic single atomic gas. Then, the shock expands with the time dependence of

$$R_{\rm s} \propto t^{2/7} \ . \tag{3.8}$$

This stage is called pressure-driven snowplow phase (McKee & Ostriker 1977). Cygnus Loop in our Galaxy is believed to undergo this phase.

As the temperature cools down further, the pressure can be ignored and the cool shell expands at a constant radial momentum ($M_s v_{\rm s}$ = const., where M_s is the mass of the shell) with the time dependence of

$$R_{\rm s} \propto t^{1/4} \ . \tag{3.9}$$

This stage is called momentum-conserving snowplow phase (Cioffi et al. 1988).

When the shock speed becomes comparable to that of the proper motion of surrounding ISM (10–20 km s^{-1}), the SNR loses its boundary with the outside and went out into the ISM. This phase is called as "Disappearance phase". The age of SNRs in this phase is larger than $\sim 10^6$ yr.

3.4 Transition between Free Expansion and Adiabatic Phases

In § 3.1 and § 3.2, we considered the limited situations of $M_{\rm ISM} \ll M_{\rm Ej}$ and $M_{\rm ISM} \gg M_{\rm Ej}$ (although energy loss is negligible). However, the transition phase between these two stages, when $M_{\rm ISM}$ is comparable to $M_{\rm Ej}$, is very important, because the most of young (standard) SNRs, such as Cassiopeia A and SN 1006, are probably in this stage. Figure 3.2 shows the realistic evolution of the blast wave between the self-similar limits of the free expansion phase and the Sedov phase.

In this transition phase, the interaction with ISM cannot be ignored, although it is not dominant yet. The swept-up ISM pushes back on the ejecta, which are thus decelerated. It causes another shock wave to propagate inward through the ejecta, called as "reverse shock" (McKee 1974). Therefore, the ejecta are compressed and heated by the reverse shock. The boundary between the ISM (shocked by the blast wave) and the ejecta (shocked by the reverse shock) is called the "contact discontinuity". The typical structure of SNRs in this transitional phase is given by the shells as previously shown in figure 2.1a. Only between the two shock waves, the material is hot enough to emit X-rays and this forms the bright shell of young SNRs. In the central region, ejecta are not hot because they are still unshocked and hence freely expanding. We can not directly receive any information from such ejecta as they have no

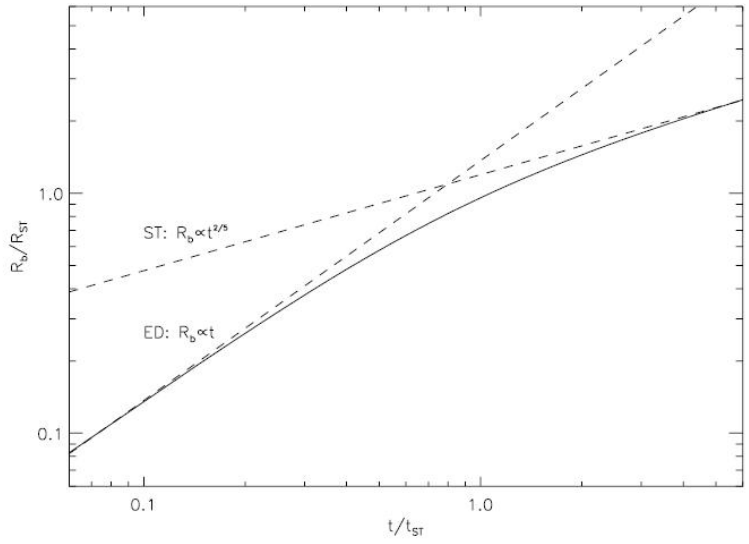

Fig. 3.2.—: Time evolution of shock wave position (solid curve) derived by a simulation of uniform ejecta expanding into a uniform ISM (Truelove & McKee 1999). The time and position are respectively normalized by the values at the transition ($t_{\rm ST}$ and $R_{\rm ST}$) from ejecta-dominated (ED) free expansion phase to Sedov-Taylor (ST) phase. The time evolution in each phase is also given in dashed curves.

X-ray emission. As was shown in figure 2.1b, 1E 0102–72 in the Small Magellanic Cloud is a typical case in this transitional phase.

As shown in figure 3.3, not only blast wave but also reverse shock initially propagate outward (as seen by an outside observer). After $M_{\rm ISM}$ becomes greater than $M_{\rm Ej}$, the reverse shock propagates back to the centre. In the case that uniform ejecta expand in homogeneous ISM, approximate shock trajectories in the moderate transition phase ($0.5 < t^* < 2.2$, in figure 3.3) are given as

$$R_b^* = (1.42t^* - 0.254)^{2/5} \tag{3.10}$$

$$R_r^* = t^*(0.779 - 0.106t^* - 0.533 \ln t^*) \tag{3.11}$$

for the blast wave and reverse shock, respectively (Truelove & McKee 1999). R^* and t^* are dimensionless values of radius and time normalized by these characteristic quantities: $R^* \equiv R/R_{\rm ch}$ and $t^* \equiv t/t_{\rm ch}$. $R_{\rm ch}$ and $t_{\rm ch}$ are those when $M_{\rm ISM} = M_{\rm Ej}$ is achieved. The shock trajectories for the cases that the ejecta distribution is not uniform but is power-law or exponential like are calculated by Truelove & McKee (1999) and Dwarkadas & Chevalier (1998) in details.

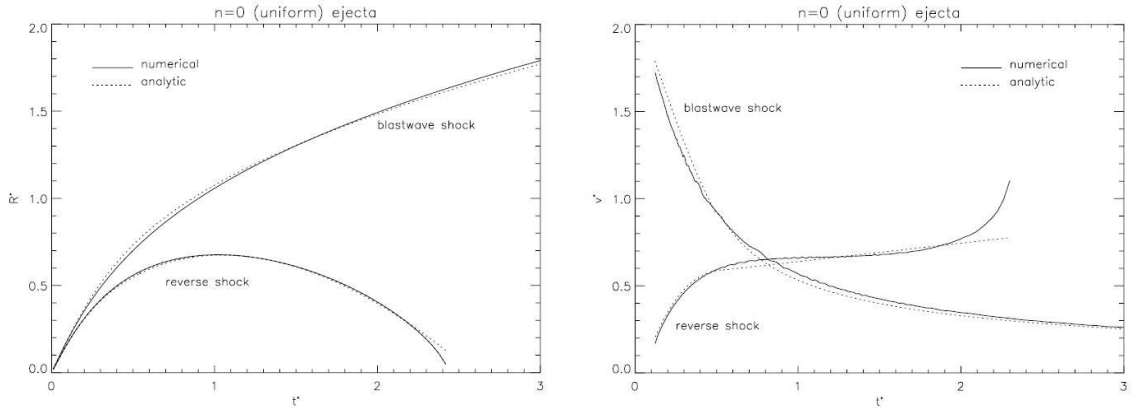

Fig. 3.3.—: Shock positions (left) and velocities (right) for blast wave and reverse shock in remnants of uniform ejecta (Truelove & McKee 1999). Note that the reverse shock velocity is measured in the frame of the unshocked ejecta ahead of it.

Chapter 4

Physical Processes and Thermal Evolution of SNRs

Contents

In this chapter, we summarize essential information to understand observed spectra of SNR plasmas. Physical processes in thermal plasma (§ 4.1), X-ray emission mechanisms (§ 4.2), and thermal evolution in the post-shock region (§ 4.3) are explained. This review is based on Rybicki & Lightman (1986) and Kaastra et al. (2008) for § 4.1 and § 4.2, and Masai (1984, 1994), Hughes & Helfand (1985), and Smith & Hughes (2010) for § 4.3.

4.1 Physical Processes in Thermal Plasma

4.1.1 Collisional Excitation

Bounded electrons in ions can be excited to higher energy levels by collisions with free electrons. The excitation cross section for transition from i to j level is written as

$$Q_{ij} = \frac{\pi a_0^2}{\omega_i} \frac{E_{\rm H}}{E_{ij}} \frac{\Omega(U)}{U} \ \ {\rm cm}^2, \tag{4.1}$$

where $U = E_{ij}/E$ is the ratio of the excitation energy E_{ij} and the energy of the exciting free electron E, $E_{\rm H}$ is the Rydberg energy of 13.6 eV, a_0 is the Bohr radius of $5.29{\times}10^{-9}$ cm, and ω_i is the statistical weight of the lower level i, respectively. $\Omega(U)$ is the dimensionless parameter called collision strength. This parameter does not have strong dependence on the atomic number Z for transitions on an isoelectronic sequence. Mewe (1972) introduced an approximated expression to describe collision strengths as follows:

$$\Omega(U) = A + \frac{B}{U} + \frac{C}{U^2} + \frac{2D}{U^3} + F \ln U \ . \tag{4.2}$$

The parameters A, B, C, D, and F have different values for each transition. This expression is useful because it can be integrated over a Maxwellian electron energy distribution analytically. The total excitation rate S_{ij} is given by

$$S_{ij} = 8.62 \times 10^{-18} \ \frac{\bar{\Omega}(y) T_{\rm e}^{-1/2} e^{-y}}{\omega_i} \ \ {\rm cm}^{-3} \ {\rm s}^{-1} \ , \tag{4.3}$$

where $y = E_{ij}/kT_{\rm e}$ is the ratio of the transition energy to the electron temperature and $\bar{\Omega}(y)$ is the Maxwellian-averaged collision strength. The rate can be approximated for the two asymptotic cases as follows:

$$S_{ij} \propto \begin{cases} T_{\rm e}^{-1/2} e^{-y} & (y \gg 1 \text{ and } \bar{\Omega}(y) \approx A + B + C + 2D) \\ T_{\rm e}^{-1/2} \ln y & (y \ll 1 \text{ and } \bar{\Omega}(y) \approx F \ln y) \end{cases} \tag{4.4}$$

However, not all transitions have asymptotic behavior. Forbidden transitions have $F = 0$ thus the excitation rates are much smaller in high energy region. Spin-forbidden transitions are even severe condition with $A = B = F = 0$.

In most cases for optically thin thermal plasma, such as plasmas in SNR and cluster of galaxies, the electron and radiation density is so low that the excited states are stable. Hence, the excited electrons will decay back to the ground level by radiative transitions. This means that the total line emission power can be directly given by the excitation rate.

4.1.2 Ionization

Collisional Ionization

Collisional ionization can occur when a bombarding free electron has a kinetic energy E higher than the binding energy I of the atomic shell where the target electron in an ion is bounded ($E > I$). The ionization cross section is given by the approximated formula by Lotz (1968):

$$\sigma_{\rm c.ioni} = 4.5 \times 10^{-20} \ \frac{N_{\rm e} \ \ln(E/I)}{EI} \ \ {\rm cm}^2 \ , \tag{4.5}$$

where $N_{\rm e}$ is the total number of electrons bounded to the shell. This formula indicate that the higher the electron energy is the less the ionizing power is. The cross section at the very threshold $E = I$ is zero.

In a thermal plasma, the total number of direct ionization per unit volume per unit time can be calculated by integrating the above cross section over Maxwellian electron energy distribution as follows:

$$C_{\rm c.ioni} \approx \begin{cases} \left(\dfrac{2\sqrt{2}aN_{\rm e}}{\sqrt{\pi m_{\rm e}}}\right) \ \dfrac{n_{\rm e}n_{\rm i}\sqrt{kT_{\rm e}}e^{-I/kT_{\rm e}}}{I^2} & (kT_{\rm e} \ll I) \\ \left(\dfrac{2\sqrt{2}aN_{\rm e}}{\sqrt{\pi m_{\rm e}}}\right) \ \dfrac{n_{\rm e}n_{\rm i}\ln(kT_{\rm e}/I)}{I\sqrt{kT_{\rm e}}} & (kT_{\rm e} \gg I) \end{cases} \tag{4.6}$$

With low temperatures, the ionization rate approaches to zero since the electrons do not have sufficient energies to ionize ions. With high temperatures, the rate again approaches to zero although the plasma has enough electrons which can ionize ions. This is because the ionization cross section reduces in higher energies (equation 4.5).

In most cases, only the collisional ionization for the electrons in outer two or three shells are important because of the dependence on I in equation 4.6.

Auto-Ionization (Inner-Shell Ionization)

Even if the case of $E \ll I$, collisional ionization can occur because of a process called auto-ionization. This process is described as follows. An electron is excited to a higher state by collision. If this state is unstable, the excited electron escapes from the bounding ion by an Auger transition. The vacancy left after the previous process is filled by another electron in the outermost shell. The two electrons can be reversed in this process. Energy conservation requires the excited electron to come from a inner shell. This process is important for Alkaline ions such as Li-like and Na-like ones, where both the excitation of inner-shell electron and vacancy-filling by outermost electron can easily occur.

Photo-Ionization

The cross section of photo-ionization as a function of the photon energy $E_{\rm ph}$ and the ionization potential I is given as follows:

$$\sigma_{\rm p.ioni} = \sigma_0 \left(\frac{I}{E_{\rm ph}}\right)^3 \ {\rm cm}^2 \tag{4.7}$$

$$= \frac{64\pi n g(E_{\rm ph}, n)\alpha_0^2}{3\sqrt{3}Z^2}\left(\frac{I}{E_{\rm ph}}\right)^3 \ {\rm cm}^2 \ , \tag{4.8}$$

where n and α are the principal quantum number and the fine structure constant, respectively. The Gaunt factor $g(E_{\rm ph}, n)$ is of order of unity and only has gradual dependence on $E_{\rm ph}$. K-shell ionization has the largest cross section for this process.

The total number of photo-ionization can be calculated by integrating with a given ionizing photon spectrum $F(E_{\rm ph})$ as follows:

$$C_{\rm p.ioni} = c \int_I^\infty n_{\rm i}\sigma(E_{\rm ph})F(E_{\rm ph})dE_{\rm ph} \ . \tag{4.9}$$

Comptonization

Compton scattering of bounded electrons also causes ionization of ions. Differential cross section for Compton scattering is given by

$$\frac{d\sigma_{\rm comp}}{d\Omega} = a_0^2\left(\frac{1}{1+\epsilon(1-\cos\theta)}\right)^2\left(\frac{1+\cos^2\theta}{2}\right)\left(1+\frac{\epsilon^2(1-\cos^2\theta)}{(1+\cos^2\theta)\{1+\epsilon(1-\cos\theta)\}}\right) \ , \tag{4.10}$$

where $\epsilon = E_{\rm ph}/m_{\rm e}c^2$ is the normalized photon energy, θ is the scattering angle, and a_0 is the Bohr radius. For non-relativistic case ($\epsilon \ll 1$), the cross section can be written as follows:

$$\frac{d\sigma_{\rm comp}}{d\Omega} = \frac{3\sigma_{\rm T}}{16\pi}\left(1+\cos^2\theta\right) \ . \tag{4.11}$$

Here, $\sigma_{\rm T} = 8\pi/3a_0^2 = 6.65\times10^{-25}$ cm^2 is the Thomson scattering cross section. The energy transfer ΔE from the incident photon to the scattered electron is given by

$$\Delta E = E_{\rm ph}\frac{\epsilon(1-\cos\theta)}{1+\epsilon(1-\cos\theta)} \ . \tag{4.12}$$

For bounded electrons, ΔE should be higher than I. Hence, a critical angle $\theta_{\rm c}$ to cause Comptonization is defined as:

$$\cos\theta_{\rm c} = 1 - \frac{\epsilon I}{E_{\rm ph}-I} \ . \tag{4.13}$$

The total Comptonization cross section approaches to $\sigma_{\rm T}$ for the case of $E_{\rm ph} \gg I$, while it reaches 0 for $\theta_{\rm c}$ gets close to π. This process is important compared with photo-ionization if an incident photons have a hard spectrum.

4.1.3 Recombination

Radiative Recombination

A capture of a free electron leads emission of a photon. This radiation is called free-bound emission. This process is the inverse process of the photo-ionization. Hence, the cross sections of these two processes ($\sigma_{\rm rr}$ and $\sigma_{\rm p.ioni}$) are connected by a simple relation. This is so-called Milne relation:

$$\sigma_{\rm rr}(v) = g_n\left(\frac{\epsilon}{\beta}\right)^2 \sigma_{\rm p.ioni}(E_{\rm ph}) \ \ {\rm cm}^2 \ , \tag{4.14}$$

where g_n is the statistical weight of the quantum level into which the electron is captured and $\beta = v/c$ is the normalized velocity of the captured electron, which conserves $E_{\rm ph} = 1/2m_{\rm e}v^2 + I$. The recombination coefficient for a level n can be calculated by averaging this cross section over Maxwellian $f(v)$:

$$R_n = n_{\rm e}n_{\rm i}\int_0^\infty v f(v)\sigma_{\rm rr}(v)dv \ . \tag{4.15}$$

Using photo-ionization cross section (equation 4.7) and the Milne relation (equation 4.14), the above equation can be written as

$$R_n = \frac{128\sqrt{2\pi}n^3\alpha a_0^2 I_n^3 e^{I_n/kT_{\rm e}} n_{\rm e}n_{\rm i}}{3\sqrt{3m_{\rm e}kT_{\rm e}}Z^2kT_{\rm e}m_{\rm e}^3}\ E_1(I_n/kT_{\rm e}), \tag{4.16}$$

where $E_1(x) = \int_x^\infty e^{-t}/t\ dt$. The two asymptotic case is expressed as

$$R_n \propto \begin{cases} T_{\rm e}^{-\frac{1}{2}} & (kT_{\rm e} \ll I;\ \text{recombining plasma}) \\ \ln(I/kT_{\rm e}) T_{\rm e}^{-\frac{3}{2}} & (kT_{\rm e} \gg I;\ \text{ionizing plasma}) \end{cases} \tag{4.17}$$

In low temperature plasma, the recombination coefficient is so large that ionization cannot be efficiently occurs. On the contrary, the coefficient goes to zero in high temperature plasma because of cross section between photons and electrons approaches to zero.

Using a rough approximation of $I \propto (Z/n)^2$, we find

$$R_n \propto \begin{cases} n^{-1} & (kT_{\rm e} \ll I;\ \text{recombining plasma}) \\ n^{-3} & (kT_{\rm e} \gg I;\ \text{ionizing plasma}) \end{cases} \tag{4.18}$$

The above relations show that recombination mainly occurs to the lowest levels in ionizing plasmas such as standard SNRs (§ 2.1). On the other hand, in recombining plasmas, many electrons are populated in excited states because the recombination coefficient has flatter dependence on n. This leads succeeding radiative transitions of excited electrons, which is called cascade lines or recombination lines. Hence, line emission from ionizing plasmas are dominated by excitation lines while that from recombining plasmas (including photo-ionizing plasmas, where the electron temperature is lower than ionization potential or ionization temperature) have significant contribution from recombination lines.

The total radiative recombination rate $\alpha_{\rm rr}$ for Hydrogen-like ions is calculated by using an approximation by Seaton (1959) to be:

$$\alpha_{\rm rr} = \Sigma_n R_n = 5.197 \times 10^{-26} Z \lambda^{1/2}\ 0.4288 + 0.5 \ln \lambda + 0.469 \lambda^{-1/3}\ . \tag{4.19}$$

Here, $\lambda = E_{\rm H} Z^2 / kT_{\rm e}$.

Dielectronic Recombination

This is the inverse of the auto-ionization process and is described as follows. A free electron is caught by an ion to a quantum level $n''l''$. This cause an excitation of a bounded electron from nl to $n'l'$ at the same time. Here, n, n', and n'' are the principal quantum numbers while l, l', and l'' are the azimuthal quantum numbers. These processes realize doubly-excited state in the ion. This unstable state can be dissolved by auto-ionization and the ion goes back to its original state. Alternative process to relax the doubly-excited state of the ion is radiative transition of the one of the excited electrons, usually the originally bounded electron. A stable excited state with the electron at $n''l''$ state is then realized. Excitations with $l' = l + 1$ is frequently occurs in the process.

The final transition probability can be approximated by

$$\alpha_{\rm dr} = \frac{A}{T_{\rm e}^{3/2}} e^{-T_0/T_{\rm e}}(1 + Be^{-T_1/T_{\rm e}}) \ , \tag{4.20}$$

where A, B, T_0 and T_1 are adjustable parameters.

A single dielectronic recombination process produces multiple lines. For example, if the process occurs for a He-like ion at the ground state, it recombines to a Li-like ion as follows:

$$\mathrm{e} + 1\mathrm{s}^2 \rightarrow 1\mathrm{s}2\mathrm{p}3\mathrm{s} \rightarrow 1\mathrm{s}^2 3\mathrm{s} + h\nu_1 \rightarrow 1\mathrm{s}^2 2\mathrm{p} + h\nu_2 \rightarrow 1\mathrm{s}^2 2\mathrm{s} + h\nu_3 \ . \tag{4.21}$$

The final transition can also occur for the case of radiative recombination into the 3s shell. Because of the existence of the extra electron in the higher orbit, the line energy $h\nu_1$ of the 2p→1s transition is slightly different from that for the same transition in He-like ion. Therefore, these shifted-center lines of Li-like ions is called satellite lines for He-like lines. There also exists various satellite lines from ions with lower ionization states, such as Be-like and B-like ones. Satellite lines due to dielectronic recombination and inner-shell processes can not be resolved by the current X-ray detectors (e.g. X-ray charge-coupled devices with $E/\Delta E \sim$20 at FWHM at K-shell line energy of He-like Fe; see next chapter for details) but can be resolved by X-ray calorimeters ($E/\Delta E \gtrsim 1000$ at the same energy) in future.

4.2 Radiation Processes

4.2.1 Continuum Emission

Bremsstrahlung

Collisions between free electrons and ions cause Bremsstrahlung. The emissivity is given by

$$\epsilon_{\rm ff} = \frac{2\sqrt{2}\alpha\sigma_{\rm T} c n_{\rm e} n_{\rm i} Z_{\rm eff}^2}{\sqrt{3\pi}E} \left(\frac{m_{\rm e}c^2}{kT_{\rm e}}\right)^{1/2} g_{\rm ff} e^{-E/kT_{\rm e}} \ . \tag{4.22}$$

where E is the emitted photon energy and $g_{\rm ff}$ is the Gaunt factor, which is order of unity. $Z_{\rm eff}$ is the effective charge of ions, defined as

$$Z_{\rm eff} = \left(\frac{n^2 I}{E_{\rm H}}\right). \tag{4.23}$$

The asymptotic approximation of equation 4.22 is written as

$$\epsilon_{\rm ff} \propto \begin{cases} E^0 & (E \ll kT_{\rm e}) \\ E^{-0.4} & (E \lesssim kT_{\rm e}) \\ \exp\left(-\frac{E}{kT_{\rm e}}\right) & (E > kT_{\rm e}) \end{cases} \tag{4.24}$$

Thus, we can measure the electron temperature $T_{\rm e}$ of hot plasmas by observing the spectra near $E \sim kT_{\rm e}$. For astrophysical plasmas with the solar abundance, the contribution from H and He is largest for this emission.

Radiative Recombination Continua

This is so-called free-bound emission (§ 4.1.3). The emissivity can be immediately calculated by using the recombination rates as

$$\epsilon_{rr} = \Sigma_r n_{\rm e} n_{\rm i} R_r \tag{4.25}$$

The flux of this emission is proportional to $n_{\rm i}$, which means RRC would be important compared with Bremsstrahlung in metal-rich plasmas.

This emission is quite important in recombining plasmas due to its high recombination rate. In this case, $kT_{\rm e} \lesssim I$ is satisfied, and thus the spectrum of RRC can be approximated by

$$\epsilon_{\rm rr} \propto \begin{cases} 0 & (E < I) \\ \exp\left(-\frac{E}{kT_{\rm e}}\right) & (E > I) \end{cases} \tag{4.26}$$

Two-Photon Emission

This is the emission due to the process called two-photon decays. When a bounded electron is excited from 1s to 2s shell, it is not allowed to directly de-excited back to the original state by a radiative transition because of the mechanical selection rules. The electron will be back to the ground state after once excited to higher state by another collision. The alternative process, two photon emission, can occur if the electron density is very low. Because of the energy conservation, the total energy of the two photons is equal to the energy difference of 1s and 2s: $E_{\rm 2ph} = E_1 + E_2 = E_{\rm 1s} - E_{\rm 2s}$. The spectrum of this emission should be symmetrical around $E = 1/2 E_{\rm 2ph}$ and the flux should approach to zero toward $E = 0$ and $E = E_{\rm 2ph}$. An empirical expression of the spectrum is given by

$$F_{\rm 2ph}(E) \sim \sqrt{\sin\left(\pi E / E_{\rm 2ph}\right)} \tag{4.27}$$

As the process starts from the 1s→2s transition, it is important for H-like and He-like ions. A low electron density is essential to this process work because it suppress the secondary collision rate. The critical density is given by

$$n_{\rm e,\ crit} = \begin{cases} 7 \times 10^3\ Z^{9.5}\ {\rm cm}^{-3} & \text{(H-like ions)} \\ 2 \times 10^5\ (Z-1)^{9.5}\ {\rm cm}^{-3} & \text{(He-like ions)} \end{cases} \tag{4.28}$$

Hence, this emission is not negligible in most of optically thin thermal plasmas, for example, SNR plasmas ($n_{\rm e} \sim$1 cm^{-3}).

4.2.2 Line Emission

Whatever the process populating a bounded electron to an excited state (j) is, it spontaneously decays back to the ground or lower state (i) due to a radiative transition. If we set the spontaneous transition probability to be A_{ij} s^{-1}, the total line power P_{ij} can be written as

$$P_{ij} = A_{ij} n_j, \tag{4.29}$$

where n_j is the number density of ions in the excited state j. Assuming the low density plasma in which collisional de-excitation is negligible, we can calculate the relative population of ions in two states, for example, the ground state g and the excited state j as

$$n_{\rm g} n_{\rm e} S_{gj} = n_j A_{ij}\ , \tag{4.30}$$

where $n_{\rm g}$ is the number density of ions in the ground state and S_{gj} is the excitation rate from the ground state to j. The line flux is determined by using equation 4.29. In more general cases, the situation is more complicated because of the existence of the intermediate states between j and the ground state, excitations and cascades from other levels, and collisional excitation and de-excitation from and to other levels (the last one would be only important in high density plasmas).

Line emission is very important for plasma diagnostics of SNRs. As described in § 4.1.1, the excitation rate directly gives the line flux in low density plasmas. This means that the line flux ratio between two different transitions of the same ions will give the electron temperature of the plasma (equation 4.4). In particular, Kβ to Kα line ratio is most frequently used for this purpose.

We can also measure the chemical abundances of hot plasmas. The flux of Bremsstrahlung is almost proportional to $n_{\rm e} n_{\rm H}$, while the line intensities of ions are proportional to $n_{\rm e} n_{\rm i}$. Thus, we determine the relative abundance of ions ($n_{\rm i}/n_{\rm H}$) from the line-to-continuum flux ratio. It is worth noting that this estimation is only valid for the situations that the contribution to continuum emission from other components is negligible. This means, for example, that we may miscalculate the abundance in recombining plasmas if RRCs are not considered.

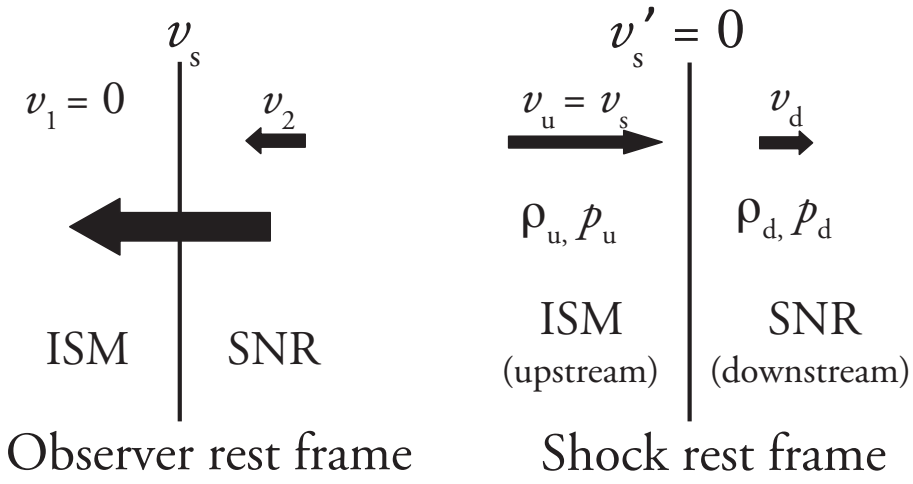

Fig. 4.1.—: A schematic view around the shock front in observer rest frame (left) and Shock rest frame (right). v, ρ, and p, are the velocity, density, and pressure, respectively.

4.3 Thermal Evolution

In the post-shock region of an SNR, the temperature is proportional to particle masses. Thus, the ion temperature is >1000 times higher than the electron temperature just after the shock heating. The electrons are then heated by ions through Coulomb collisions. The high-temperature electrons gradually ionize atoms of heavy elements. In the following subsections, we summarize these processes.

4.3.1 Shock-Wave Heating

The shock wave heating can be understood as the energy conversion from the kinetic energy to the thermal energy. Here, we briefly summarize this process.

We here take a coordinates to be the rest frame of the shock, and define upstream and downstream as figure 4.1. The tangential component of the gas velocity is assumed to be zero on both regions. Conservation of mass, momentum, and energy across the shock front can be written respectively as

$$\rho_{\rm u} v_{\rm u} = \rho_{\rm d} v_{\rm d} \tag{4.31}$$

$$\rho_{\rm u} v_{\rm u}^2 + p_{\rm u} = \rho_{\rm d} v_{\rm d}^2 + p_{\rm d} \tag{4.32}$$

$$\frac{1}{2} v_{\rm u}^2 + w_{\rm u} = \frac{1}{2} v_{\rm d}^2 + w_{\rm d} \ , \tag{4.33}$$

where ρ, v, p, and w are the mass density, velocity, pressure, and enthalpy of both upstream (subscript u) and downstream (subscript d), respectively. Assuming the fluid to be ideal gas, the enthalpy is given as

$$w = C_p T = \frac{\gamma p}{(\gamma - 1)\rho} \ , \tag{4.34}$$

where γ is the specific heat ratio ($= C_p/C_V$). From equations 4.31, 4.32, 4.33, and 4.34, so-called Rankine-Hugoniot relations between the physical conditions of the upstream and the downstream are obtained as

$$\frac{\rho_\mathrm{u}}{\rho_\mathrm{d}} = \frac{v_\mathrm{d}}{v_\mathrm{u}} = \frac{(\gamma+1)p_\mathrm{u} + (\gamma-1)p_\mathrm{d}}{(\gamma-1)p_\mathrm{u} + (\gamma+1)p_\mathrm{d}} \tag{4.35}$$

$$\frac{p_\mathrm{u}}{p_\mathrm{d}} = \frac{(\gamma+1)\rho_\mathrm{u} - (\gamma-1)\rho_\mathrm{d}}{(\gamma+1)\rho_\mathrm{d} - (\gamma-1)\rho_\mathrm{u}} \tag{4.36}$$

$$\frac{T_\mathrm{d}}{T_\mathrm{u}} = \frac{p_\mathrm{d}\rho_\mathrm{u}}{p_\mathrm{u}\rho_\mathrm{d}} = \frac{p_\mathrm{d}}{p_\mathrm{u}} \frac{(\gamma+1)p_\mathrm{u} + (\gamma-1)p_\mathrm{d}}{(\gamma-1)p_\mathrm{u} + (\gamma+1)p_\mathrm{d}} \ . \tag{4.37}$$

For the velocities of the gas, we obtain

$$v_\mathrm{u}^2 = \frac{1}{2\rho_\mathrm{u}}\{(\gamma-1)p_\mathrm{u} + (\gamma+1)p_\mathrm{d}\} \tag{4.38}$$

$$v_\mathrm{d}^2 = \frac{1}{2\rho_\mathrm{u}} \frac{\{(\gamma+1)p_\mathrm{u} + (\gamma-1)p_\mathrm{d}\}^2}{(\gamma-1)p_\mathrm{u} + (\gamma+1)p_\mathrm{d}} \ . \tag{4.39}$$

Assuming the strong shock ($p_\mathrm{d}/p_\mathrm{u} \gg 1$), equations 4.35, 4.37, 4.38, and 4.39 can be respectively rewritten as

$$\frac{\rho_\mathrm{u}}{\rho_\mathrm{d}} = \frac{v_\mathrm{d}}{v_\mathrm{u}} = \frac{\gamma-1}{\gamma+1} \tag{4.40}$$

$$\frac{T_\mathrm{u}}{T_\mathrm{d}} = \frac{p_\mathrm{d}}{p_\mathrm{u}} \frac{\gamma-1}{\gamma+1} \tag{4.41}$$

$$v_\mathrm{u}^2 = \frac{(\gamma+1)p_\mathrm{d}}{2\rho_\mathrm{u}} \tag{4.42}$$

$$v_\mathrm{d}^2 = \frac{(\gamma-1)^2 p_\mathrm{d}}{2(\gamma+1)\rho_\mathrm{u}} \ , \tag{4.43}$$

where, v_u equals to v_s, the shock velocity at the rest frame of the upstream (see figure 4.1), We can derive the mean post-shock temperature using equations 4.40 and 4.43:

$$kT_\mathrm{d} = \mu m_\mathrm{H} \frac{p_\mathrm{d}}{\rho_\mathrm{d}} = \frac{2(\gamma-1)}{(\gamma+1)^2} \mu m_\mathrm{H} v_s^2 \ , \tag{4.44}$$

where k, μ, and m_H are the Boltzmann constant, the mean atomic weight, and the hydrogen mass, respectively. For the non-relativistic single atomic gas ($\gamma = 5/3$), the upstream-to-downstream ratio of the density and velocity are respectively derived as $\rho_\mathrm{d}/\rho_\mathrm{u} = 4$ and $v_\mathrm{d}/v_\mathrm{u} = 1/4$. The post-shock temperature can be obtained as

$$kT_\mathrm{d} = \frac{3}{16} \mu m_\mathrm{H} v_s^2 \ . \tag{4.45}$$

4.3.2 Energy Transfer from Ions to Electrons toward Equipartition

As described in equation 4.45, the post-shock temperatures are proportional to the mean particle mass just after the shock passage. Hence the particles are in non-equipartition state at this phase: the ion temperature $T_{\rm i}$ is at least 1,000 times higher than the electron temperature $T_{\rm e}$. The electrons are heated by the ions via Coulomb collisions in the post-shock region. By defining the dimensionless temperatures normalized by $T_{\rm d}$ ($\theta_{\rm e} = T_{\rm e}/T_{\rm d}$ and $\theta_{\rm i} = T_{\rm i}/T_{\rm d}$), the equipartition time $t_{\rm eq}$ between electrons and ions can be written as (Spitzer 1962)

$$t_{\rm eq} = 5.87 \frac{A_{\rm e}^{\frac{1}{2}}}{\epsilon n_{\rm e} \ln\Lambda} T_{\rm d}^{\frac{3}{2}} (\theta_{\rm e} + \epsilon\theta_{\rm i})^{\frac{3}{2}} \ {\rm s} \ , \tag{4.46}$$

where $A_{\rm e}$ is the electron mass in units of amu, $\epsilon = m_{\rm e}/m_{\rm i}$ is the mass ratio between the electrons and ions, and $\ln\Lambda$ is the dimensionless parameter called Coulomb logarithm (Spitzer 1962), which takes on values $\approx$10. Λ for protons can be written as follows

$$\Lambda = \left(\frac{1}{4\pi n_{\rm e}}\right)^{\frac{1}{2}} \left(\frac{kT_{\rm e}}{e^2}\right)^{\frac{3}{2}} \ . \tag{4.47}$$

By introducing the characteristic time $t_{\rm s}$, the above equation can be rewritten as

$$t_{\rm eq} = t_{\rm s} (\theta_{\rm e} + \epsilon\theta_{\rm i})^{\frac{3}{2}} \ {\rm s} \ , \tag{4.48}$$

where

$$t_{\rm s} = 2.5 \times 10^2 \frac{T_{\rm d}^{\frac{3}{2}}}{n_{\rm e} \ln\Lambda} \ {\rm s} \ . \tag{4.49}$$

The equipartition process can be described by the following relations with the dimensionless time $\tau = t/t_{\rm s}$:

$$\frac{d\theta_{\rm e}}{d\tau} = (\theta_{\rm i} - \theta_{\rm e})(\theta_{\rm e} + \epsilon\theta_{\rm i})^{-\frac{3}{2}} \ , \tag{4.50}$$

$$\frac{d\theta_{\rm i}}{d\tau} = (\theta_{\rm e} - \theta_{\rm i})(\theta_{\rm e} + \epsilon\theta_{\rm i})^{-\frac{3}{2}} \ , \tag{4.51}$$

$$\theta_{\rm e} + \theta_{\rm i} = 2 \ . \tag{4.52}$$

$$\tag{4.53}$$

We take initial conditions to be

$$kT_{\rm e} \ = \ \frac{3}{16} \mu m_{\rm e} v_s^2 \ , \tag{4.54}$$

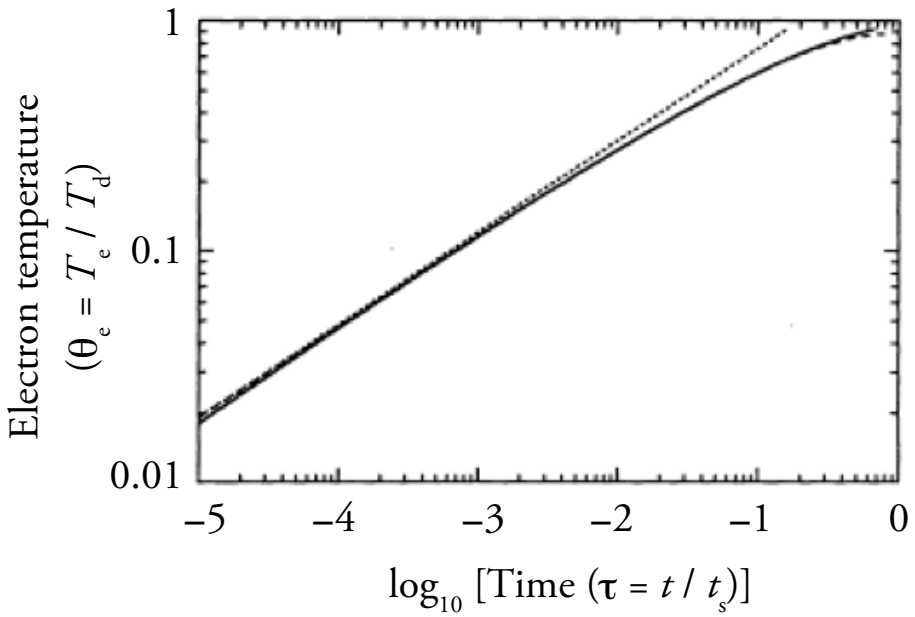

Fig. 4.2.—: Evolution of the normalized electron temperature $\theta_{\rm e}$ due to Coulomb collisions with the ions in the post-shock region (Masai 1994). The solid, dashed, and dotted lines indicate the analytic solution (equation 4.57) and its approximations up to the second (equation 4.60) and the first order (equation 4.61), respectively.

$$kT_{\rm i} = \frac{3}{16}\mu m_{\rm i} v_s^2 \ . \tag{4.55}$$

(4.56)

Then, an analytical solution can be found as follows:

$$\tau(x) = \left[\frac{1}{3}x^3 + (1+\epsilon)x + \frac{1}{2}(1+\epsilon)^{\frac{3}{2}} \ln\left|\frac{x-(1+\epsilon)^{\frac{1}{2}}}{x+(1+\epsilon)^{\frac{1}{2}}}\right|\right]_x^{x_0} , \tag{4.57}$$

with $x = \{(1-\epsilon)\theta_{\rm e} + 2\epsilon\}^{1/2}$, where $x_0 \approx (3\epsilon - \epsilon^2)^{1/2}$ is the initial value corresponding to the initial electron temperature of $\approx \epsilon T_{\rm d}$.

The condition of $T_{\rm e} \gg \epsilon T_{\rm d}$ or $x \gg x_0$ can be attained in a negligible short time. In this condition, the above equation is approximated by using $x \ll 1$:

$$\tau = \frac{1}{5}x^5\left(1 + \frac{5}{7}x^2 + \frac{5}{9}x^4 + \cdots\right) \approx \frac{1}{5}\theta_{\rm e}^{\frac{5}{2}} \ . \tag{4.58}$$

Hence, the time evolution of the electron temperature $T_{\rm e}$ due to Coulomb collisions can be expressed as

$$\frac{T_{\rm e}}{T_{\rm d}} = \theta_{\rm e} \approx x^{\frac{1}{2}} \tag{4.59}$$

$$\approx (5\tau)^{\frac{2}{5}} \left[1 - \frac{2}{7}(5\tau)^{\frac{2}{5}}\right] \tag{4.60}$$

$$\approx (5\tau)^{\frac{2}{5}} = (5\frac{t}{t_{\rm s}})^{\frac{2}{5}} \ . \tag{4.61}$$

We can estimate the electron temperature at the time t to be

$$T_{\rm e} = 0.21(T_{\rm d} \ln\Lambda)^{\frac{2}{5}} (n_{\rm e} t)^{\frac{2}{5}} \ {\rm K}. \tag{4.62}$$

We note that the electron temperature $T_{\rm e}$ scales as $(n_{\rm e}t)^{2/5}$.

4.3.3 Collisional Ionization toward Ionization Equilibrium

When the electron temperature of a SNR plasma becomes high enough, the ions are gradually ionized by collisions with high-temperature electrons. Both ionization and recombination processes take place to reach a steady state where they are balanced. This final state is called collisional ionization equilibrium (CIE). In plasmas before reaching CIE, the ionization balance is not reached and hence non-equilibrium ionization (NEI) goes on.

Since the standard scenario assumes uniform interstellar gas with no pre-existing ionization source as SN environments, the initial ionization states should be nearly neutral. Because of the initial condition, ionization process should dominate over recombination process in total. Such a plasma is called "ionizing plasma". The thermal evolution of the standard SNR plasmas is described as the gradual transition from ionizing plasmas to CIE plasmas. Hence, the recombining plasma, which is the inverse case of the ionizing plasma, can not be realized in the standard evolution.

Collisional Ionization Equilibrium

CIE is the state that the concentration of charge states of ions (hereafter, ion concentration) are uniquely determined by the electron temperature because the ionization and the recombination rates are balanced each other. Such a situation is realized in a relaxed plasma with no strong radiation field which contributes photo-ionization and Comptonization.

In CIE plasmas, the net change of the number of ions in any charge state is zero:

$$\begin{cases} n_{z+1}R_{z+1}(T_{\rm e}) - n_z R_z(T_{\rm e}) + n_{z-1}I_{z-1}(T_{\rm e}) - n_z I_{z-1}(T_{\rm e}) = 0 & (z>0) \\ n_1 R_1(T_{\rm e}) = n_0 I_0(T_{\rm e}) & (z=0), \end{cases} \tag{4.63}$$

where $R_z(T_{\rm e})$ is the total recombination rate from the charge state z to $z-1$ and $I_z(T_{\rm e})$ is the total ionization rate from z to $z+1$.

Non-Equilibrium Ionization

Non-equilibrium ionization (NEI) is the case that the ionization balance between the ion concentration and the electron temperature has not reached yet. Such a plasma can be observed if the system is disturbed by some processes suddenly, for example, shock heating or dynamic (adiabatic) cooling of electrons. Extra ionization due to high energy radiation field or supra-thermal electrons can also disturb CIE state. The plasma takes a finite time to recover CIE. In NEI plasmas, the change of the number of each charge state is not zero. If the charge states are low compared with the electron temperature, the plasma is called ionizing plasma because the ionization process dominates over the recombination process. The inverse case is called recombining plasma.

We can write the time evolution of the number of ions in each charge state as follows:

$$\frac{1}{n_{\rm e}(t)}\frac{d}{dt}n_z = n_{z+1}R(T_{\rm e})_{z+1} - n_z R_z(T_{\rm e}) + n_{z-1}I_{z-1}(T_{\rm e}) - n_z I_{z-1}(T_{\rm e}) \ . \tag{4.64}$$

The equation is scaled by $n_{\rm e}$ because both the ionization and recombination are caused by collisions with electrons. This equation can be converted to a matrix form:

$$\frac{1}{n_{\rm e}(t)}\frac{d}{dt}\vec{n} = -\boldsymbol{A}(T_{\rm e})\cdot\vec{n} \ , \tag{4.65}$$

where $\vec{n}$ is the ion concentration vector with a length of $(Z+1)$ and $\boldsymbol{A}$ is the transition matrix with a size of $(Z+1)^2$. This matrix is given by

$$\boldsymbol{A} = \begin{pmatrix} I_0 & -R_1 & & & & & 0 \\ -I_0 & I_1+R_1 & \ddots & & & & \\ & -I_1 & \ddots & -R_j & & & \\ & & \ddots & I_j+R_j & \ddots & & \\ & & & -I_j & \ddots & -R_{Z-1} & \\ & & & & \ddots & I_{Z-1}+R_{Z-1} & -R_Z \\ 0 & & & & & -I_{Z-1} & R_Z \end{pmatrix} . \tag{4.66}$$

For convenience, we define $\vec{m} = \vec{n} = \vec{n}_{\rm eq}$, where $\vec{n}_{\rm eq}$ is the ion concentration in CIE. Using $\boldsymbol{V}(T_{\rm e})$ as the matrix of the eigenvectors of $\boldsymbol{A}(T_{\rm e})$ with eigenvalues $\vec{\lambda}$, we can write

$$\frac{1}{n_{\rm e}(t)}\frac{d}{dt}\vec{m}' = -\boldsymbol{\Lambda}\cdot\vec{m}' \ , \tag{4.67}$$

where $\vec{m}' = \boldsymbol{V}(T_{\rm e})^{-1}\vec{m}$ and $\boldsymbol{\Lambda} = \vec{\lambda}\boldsymbol{I}$. The solution can be written as

$$\vec{m}'(t) = \vec{c}\exp\left(-n_{\rm e}\vec{\lambda}t\right) \ , \tag{4.68}$$

where $\vec{c}$ is determined by the initial condition. We can calculate the ion concentration for charge state i as

$$m_i(t) = \Sigma_j V_{ji} m'_j = \Sigma_j V_{ji} c_j \exp(-n_{\rm e}\lambda_j t) \ . \tag{4.69}$$

These equations generally solved numerically. The exponential form of equation 4.68 indicates that ions have characteristic density-weighted timescale to reach CIE. Hence, the time evolution of NEI plasmas can be described by the integral of density-weighted timescale,

$$\tau = \int n_{\rm e} dt \ . \tag{4.70}$$

The typical timescale to reach CIE is $\tau = 10^{12-13}$ cm^{-3} s. In some real cases, we should also take the time evolution of the electron temperature $T_{\rm e}(t)$ into consideration but most of popular plasma codes which calculate NEI plasmas are assuming constant $T_{\rm e}$.

Ionization Temperature

We define an ionization temperature $T_{\rm z}$ in order to characterize the ion concentration of a hot plasma (see figure 4.3). This temperature is equal to that of the CIE plasma which realizes the observed ion concentration. By this definition, we re-define the CIE, ionizing, and recombining plasmas as follows:

$$\begin{cases} T_{\rm z} = T_{\rm e}, \ \dfrac{dT_{\rm z}}{dt} = 0 & \text{(CIE)}, \\ T_{\rm z} < T_{\rm e}, \ \dfrac{dT_{\rm z}}{dt} > 0 & \text{(ionizing)}, \\ T_{\rm z} > T_{\rm e}, \ \dfrac{dT_{\rm z}}{dt} < 0 & \text{(recombining)}. \end{cases} \tag{4.71}$$

As shown in figure 4.3, plasmas in each ionization temperature are dominated by only two or three ionization states. Hence, it is convenient to define average charges $\bar{z}$ as follows:

$$\bar{z} = \Sigma \ z \cdot n_z \ . \tag{4.72}$$

As shown in figure 4.4, average charges monotonically increase with respect to the ionization temperature. Because the ions with complete valence shells have higher ionization potentials, the curves have the plateaux at Ne-like and He-like ionization states.

SNR plasmas have ionization temperatures of 0.1–10 keV and are dominated by He-like, H-like and bared ions. Thus, we can determine the ionization temperature by the line flux ratio between H-like and He-like Kα lines. Similarly, the flux ratio of K-shell RRCs from H-like and He-like ions is the indicator of the ionization temperature.

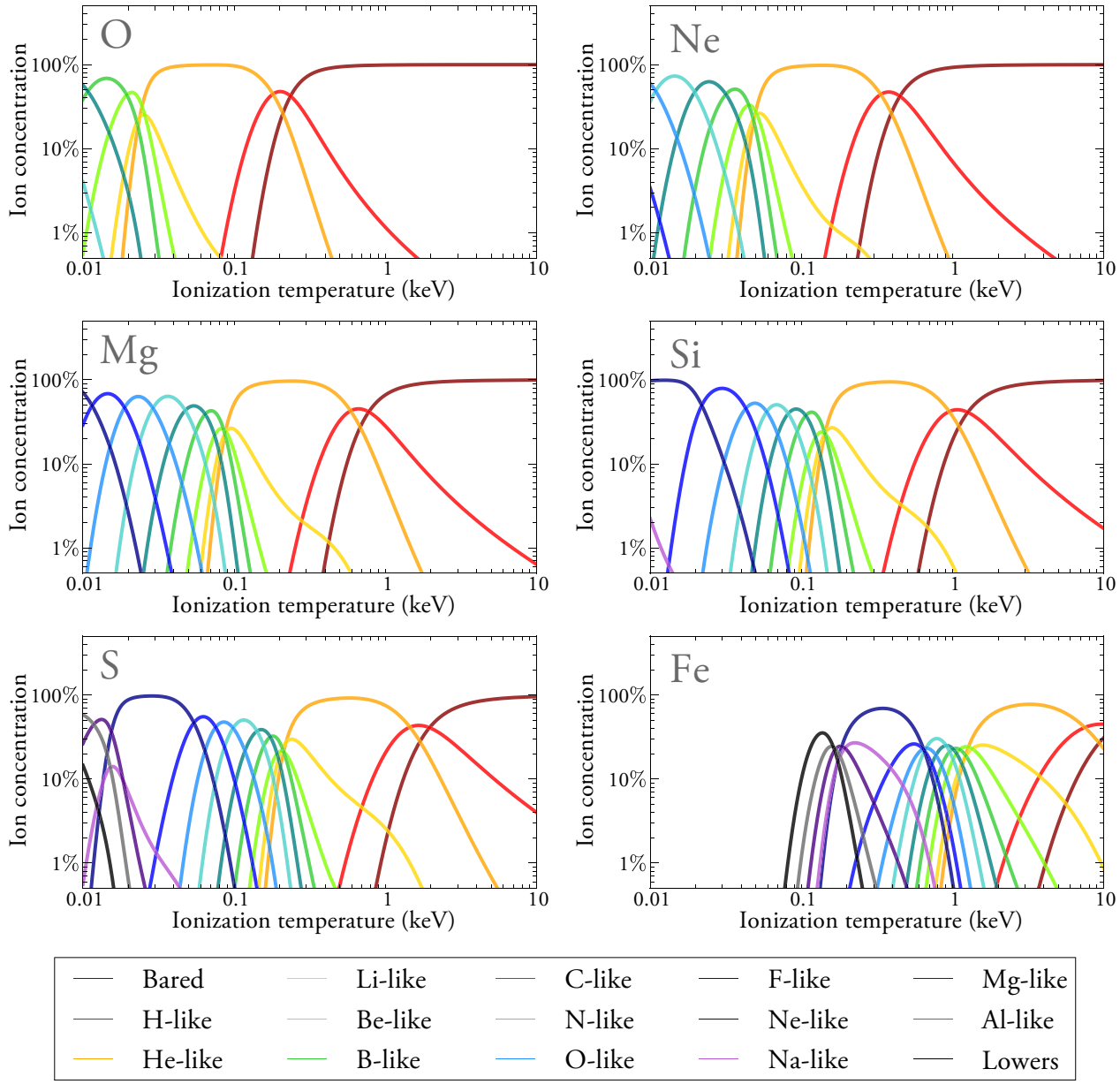

Fig. 4.3.—: Ion concentrations with respect to the ionization temperatures for (a) O, (b) Ne, (c) Mg, (d) Si, (e) S from Arnaud & Rothenflug (1985) and (f) Fe from Arnaud & Raymond (1992).

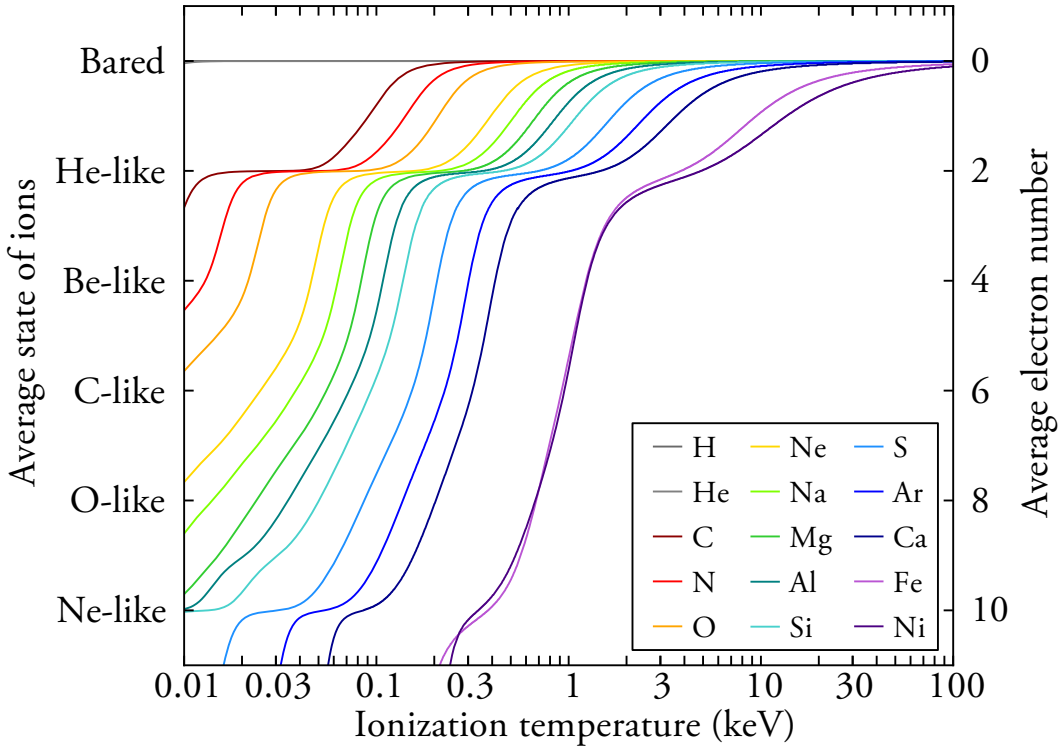

Fig. 4.4.—: Average charges with respect to the ionization temperatures. Ion concentrations are from Arnaud & Raymond (1992) for Fe and Arnaud & Rothenflug (1985) for the others.

Chapter 5

Instruments

Contents

5.1 Overview of the Suzaku Satellite

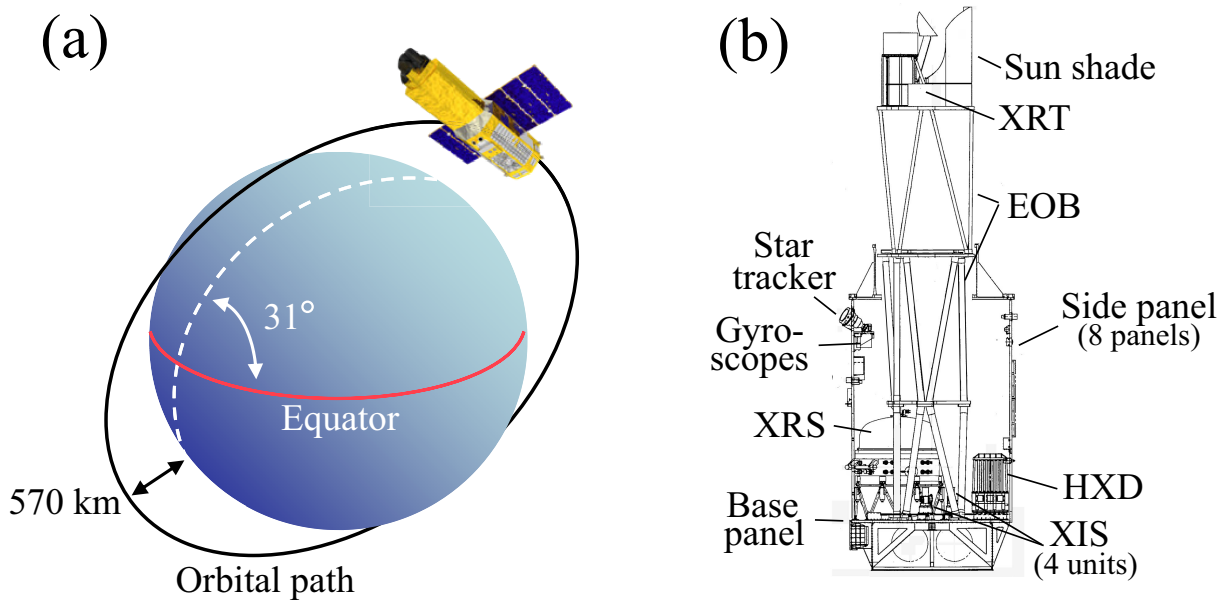

Fig. 5.1.—: (a) Schematic view of the Suzaku satellite in orbit (Mitsuda et al. 2007). (b) Schematic cross-section of Suzaku with the internal structure after the EOB extension (Mitsuda et al. 2007).

Suzaku is the fifth Japanese satellite for X-ray astronomy developed under Japan–US collaboration. It was successfully launched and put into Low-Earth Orbit by the sixth M-V rocket from the Uchinoura Space Center on 2005 July 10. The satellite orbits every ∼96 minutes with a near circular path of an altitude of ∼570 km and an inclination angle of ∼31°. Figure 5.1(a) shows a schematic view of Suzaku in the orbit. The spacecraft length is 6.5 m along the telescope axis after extending the extensible optical bench (EOB) and the total weight is ∼1700 kg.

The electric power of ∼660 W is provided by the solar panels fixed on the satellite. This configuration constrains the pointing direction to be 65°–110° from the Sun. Because of the Sun angle restriction, observation targets are occulted by the Earth every orbital path except for objects near the orbital pole. The average observation efficiency is ∼45%.

Suzaku is equipped with two imaging detectors combined with X-Ray Telescopes (XRTs: Serlemitsos et al. 2007) and one non-imaging hard X-ray detector (HXD: Takahashi et al. 2007; Kokubun et al. 2007). One of the imaging detector is X-ray Imaging Spectrometer (XIS: Koyama et al. 2007a), which uses X-ray Charge-Coupled Devices (CCDs). The other is X-Ray Spectrometer (XRS: Kelley et al. 2007), which uses an X-ray micro-calorimeter. Unfortunately, the XRS has not been functional owing to the evaporation of the liquid helium coolant since a few weeks after the launch. The configuration of the detectors are shown in figure 5.2. The

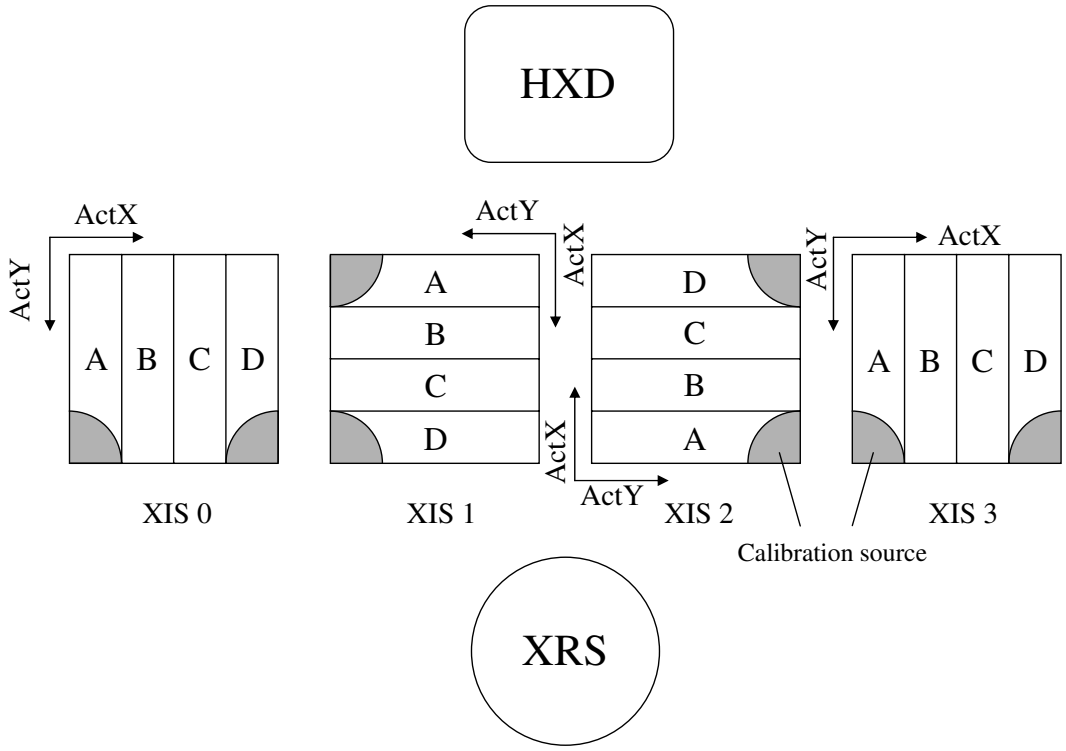

Fig. 5.2.—: Configuration of the detectors in the Suzaku satellite. (the Suzaku technical description). The definition of the XIS coordinates is also shown.

detailed descriptions of the XRS and the HXD will not discussed any further as we do not use them.

5.2 XRT

5.2.1 Overview of the XRT

Five XRT modules are installed on the top plate of the EOB. One is designated as XRT-S, dedicated for the XRS. The other four modules are adapted for each XIS camera and referred to as XRT-I0, I1, I2, and I3 (figure 5.3).

X-rays are reflected by smooth surfaces of high-electron-density material at very shallow angles of $\leq 1^\circ$ (grazing incidence). Since the reflection is non-dispersive, circular X-ray mirrors for grazing incidence can focus X-rays over a broad energy band. In this configuration, only a fraction of the geometric area of the telescope can be used to collect X-ray photons for imaging,

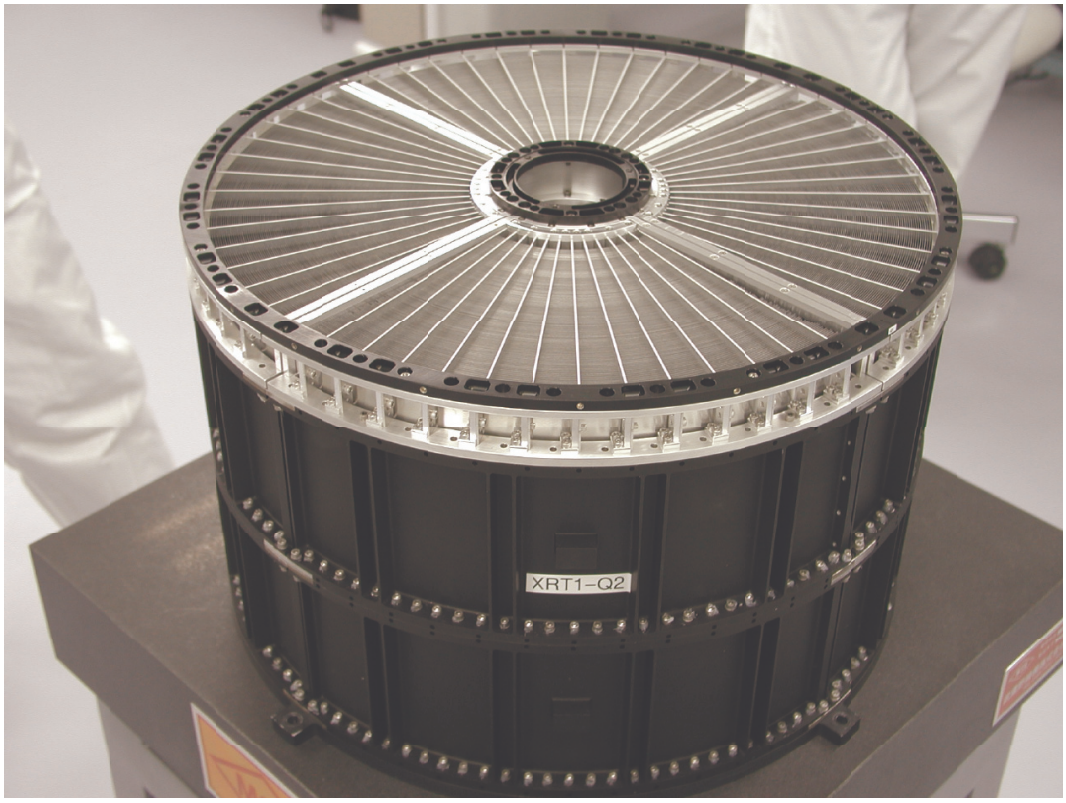

Fig. 5.3.—: Picture of the XRT-I1 module (Serlemitsos et al. 2007).

so multiple layers are combined to increase the total effective area.

In Wolter type-I reflective optics, X-rays are reflected twice by a parabolic surface and a hyperbolic surface sequentially (figure 5.4). The precise Wolter design yields a spatial resolution of $\sim 1''$, such as the X-ray telescope adopted for the Chandra X-ray Observatory. However, this sacrifices the effective area, as the small surface roughness requires a heavy substrate and limits the number of nesting layers.

Suzaku takes different approach. It increases the effective area with 175 thin foil layers in each XRT-I module at the sacrifice of good angular resolution. It is difficult to construct a precise Wolter geometry with thin foils with a thickness of ~ 180 μm adopted for XRT, so both the primary and secondary reflectors of XRT are approximated by simple cones, which limits the angular resolution to about $\sim 18''$. Since the electron density strongly depends on the atomic number, the reflector surface is coated with Au with a thickness of ≥ 1000 Å.

Both the primary and secondary reflectors are made of four sections, which are called "quadrants". Since the spaces between two quadrants are dead areas, point source images appear to be a cross or a butterfly as shown in figure 5.6.

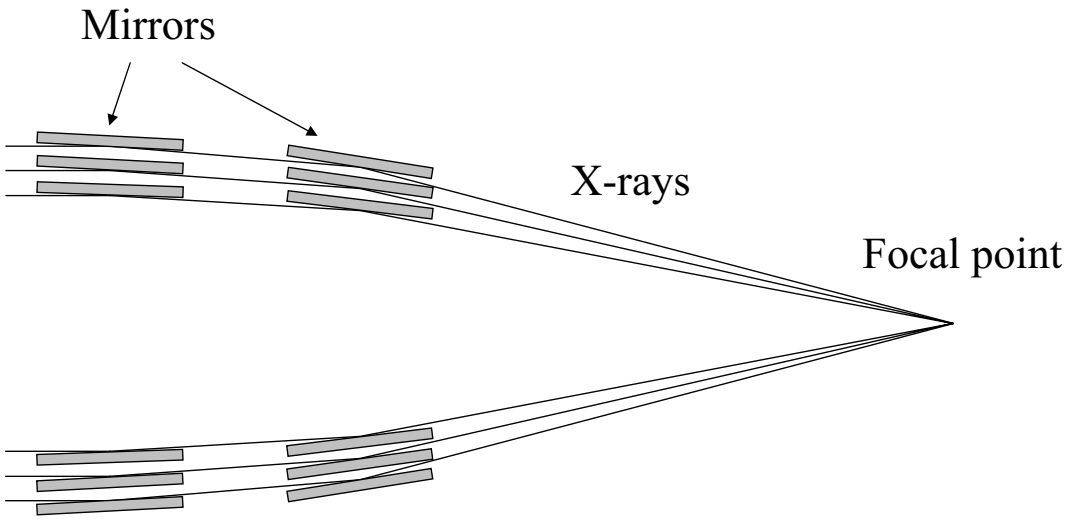

Fig. 5.4.—: Schematic cross-section of Wolter-I type X-ray mirror. Incident X-rays are reflected twice at very shallow angles and concentrated at the focal point.

5.2.2 Onborad Performance

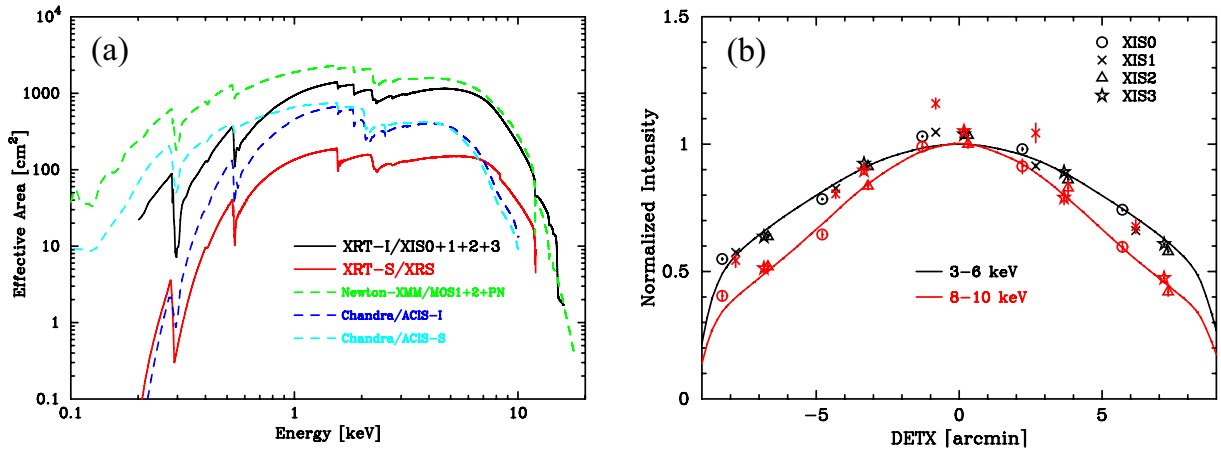

Fig. 5.5.—: (a) Total effective area of the XRT combined with the XIS (Serlemitsos et al. 2007). Those of other X-ray missions are also shown for comparison. (b) Off-axis angle dependence of the effective area normalized at the optical axes in the soft and hard bands shown with black and red points, respectively (Serlemitsos et al. 2007). Data are obtained with the observations of Crab nebula. The solid lines show the simulated model.

The left panel of figure 5.5 shows the energy-dependent on-axis effective area including the detector efficiency. At larger off-axis angles, incident X-rays are partially obscured by neighbor-

ing reflectors. This effect is called "vignetting" and is more prominent at higher energy. This is because high energy photons have smaller critical angles and are efficiently reflected at innermost mirrors, where the cone angles is small and the reflectors are tightly packed, thus highly subject to shadowing. Figure 5.5b shows the vignetting curve in the soft (3–6 keV) and hard (8–10 keV) bands. Since the effective area is defined by the number of source photons within the CCD field of view (FOV) of a $17'.8 \times 17'.8$ square, the model curves show sharp drops at $\sim 8'$.

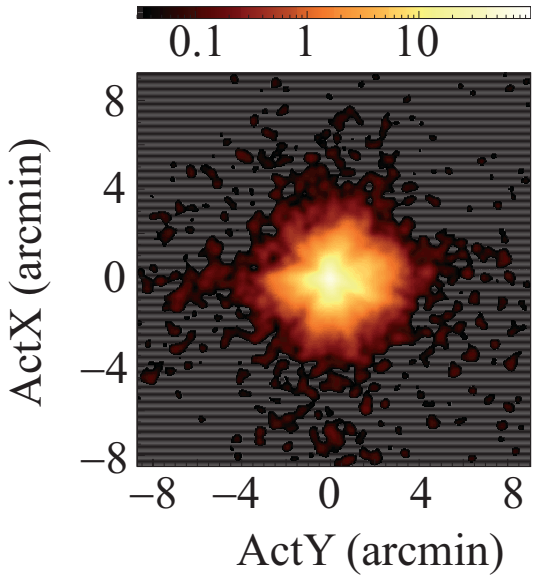

Fig. 5.6.—: Image of SS Cygni at the optical axis taken with XRT-I2 (Serlemitsos et al. 2007). The color scale shows the X-ray counts pixel^{-1}

The angular resolution was verified with the SS Cygni data in quiescence (figure 5.6).

Figure 5.7 shows the point spread function (PSF) and the encircled energy fraction (EEF). The half-power diameter (HPD), the typical indicator of spatial resolution, is obtained to be $1'.8$, $2'.3$, $2'.0$, and $2'.0$ for XRT-I0, 1, 2, and 3, respectively. Since the primary factor of the XRT spatial resolution is the misalignment of the nested reflectors, the HPD is nearly independent on photon energy or off-axis angle within $\sim$10%.

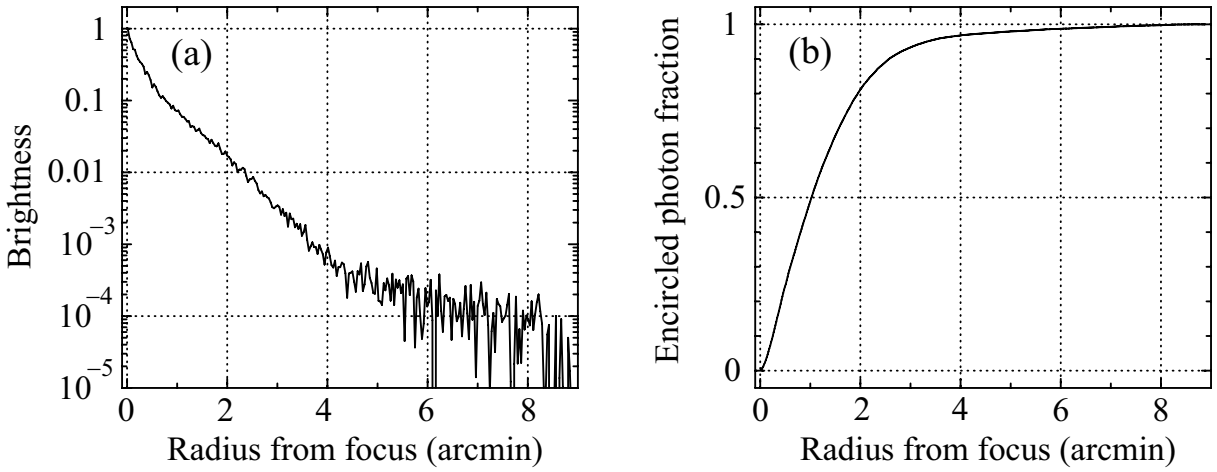

Fig. 5.7.—: Point spread function (PSF, left panel) and the encircle energy fraction (EEF, right panel) of the XRT (for XIS2) at the focal plane (Serlemitsos et al. 2007).

5.3 XIS

5.3.1 Overview of the XIS

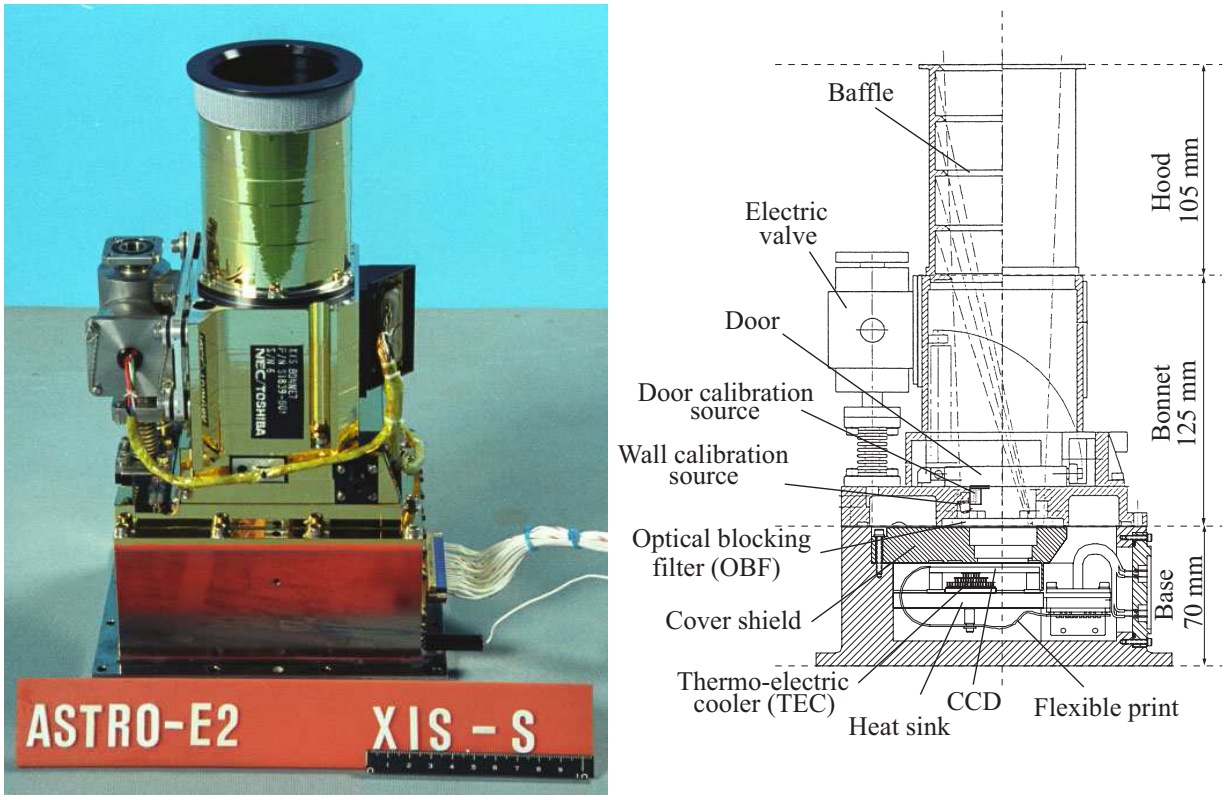

Fig. 5.8.—: Left panel: Picture of one of the XIS sensors. Right panel: Cross section of the XIS sensor (Koyama et al. 2007a).

The XIS is comprised of four X-ray CCD camera systems (figure 5.8). X-ray CCD converts an incident X-ray photon to a cloud of electrons, the amount of which is proportional to the energy of the absorbed X-ray photon. The cloud made in the depletion layer in each pixel is transferred to the gate of the output transistor by three-phase electric potential clocking. In MOS-type CCDs (figure 5.9), the gate, insulator, and depletion layer are made of poli-Si (Metal), SiO_2 (Oxide), and Si (Semiconductor), respectively. In the frame transfer mode, the charges are transferred from the imaging area (IA) to the frame store (FS) region after an exposure. Then, the charges in the FS region is transferred vertically along the ActY direction and horizontally along the ActX direction sequentially.

One side of a CCD is coated with the gate structure mainly made of Si and SiO_2 (front side). Front-illuminated (FI) CCDs detect X-rays that penetrate the gate structure with a thick-

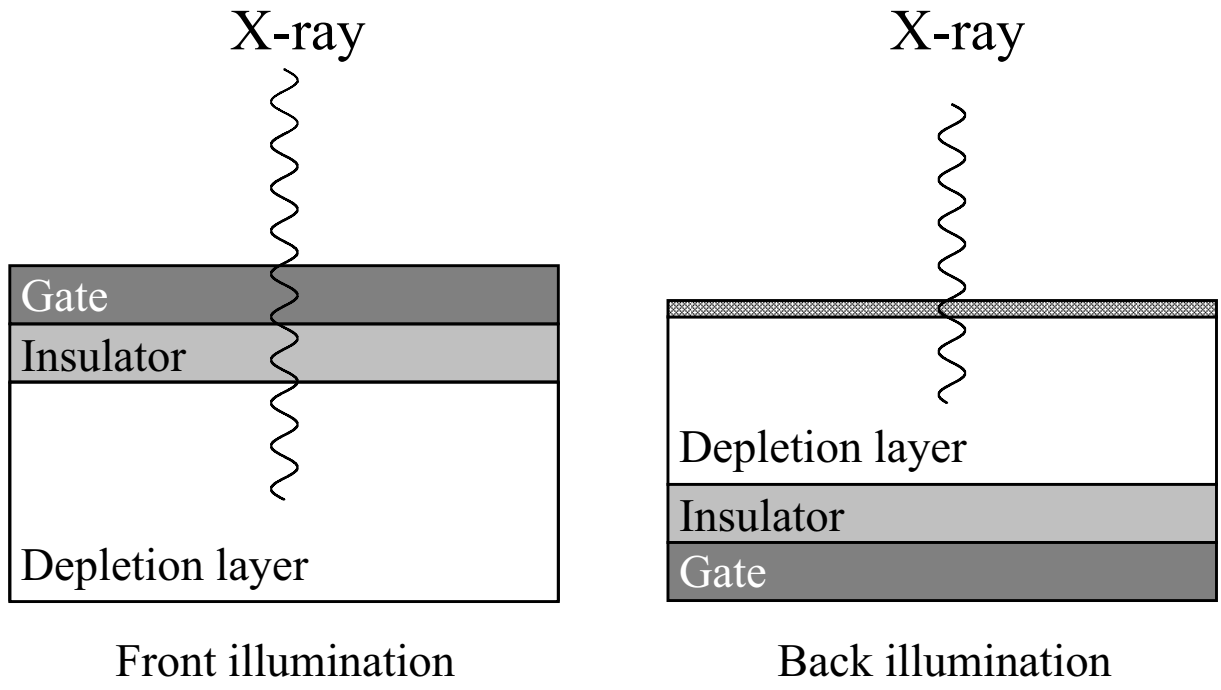

Fig. 5.9.—: Difference of front illumination and back illumination in MOS-type CCD.

ness of ~ 0.7 μm, whereas the surface dead layer of back-illuminated (BI) CCDs have a thickness of ~ 10 nm (figure 5.9). Due to the absence of the gate structure, BI CCDs reach a high quantum efficiency (QE) even below ~ 1 keV. On the other hand, FI CCDs employ thicker depletion layer than BI CCDs (~ 76 μm for FI CCDs and ~ 42 μm for BI CCD), and have higher QE for high energy photons. Three of the XIS cameras (XIS 0, XIS 2, and XIS 3) use FI CCDs, and the remaining one (XIS 1) uses a BI CCD. The QE of each FI CCD is better than that of the BI CCD above ~ 4 keV, while BI becomes superior QE in lower energy (figure 5.10).

In both the IA and FS regions, the CCD chips have a format of 1024×1024 pixels and four read-out nodes. Thus, a CCD chip is composed of four segments of 256×1024 pixels (figure 5.11). The pixel size of the IA is 24 μm$\times$24 μm. Combined with XRT, each pixel corresponds to $1.04'' \times 1.04''$ of the sky, and the field of view is $17\farcm8 \times 17\farcm8$. The detector is operated at a temperature of $\sim -90^{\circ}$C controlled by Pertier coolers.

Each XIS has an optical blocking filter (OBF) to block optical and UV photons. The OBF is made of ~ 1400 Å polyimide ($C_{22}H_{10}N_2O_4$) coated with Al of a ~ 1200Å thickness.

For on-orbit calibration of the energy scale and resolution, each sensor is equipped with two radioactive sources (^{55}Fe). ^{55}Fe decays to leave ^{55}Mn via electron capture mainly (88.5%)

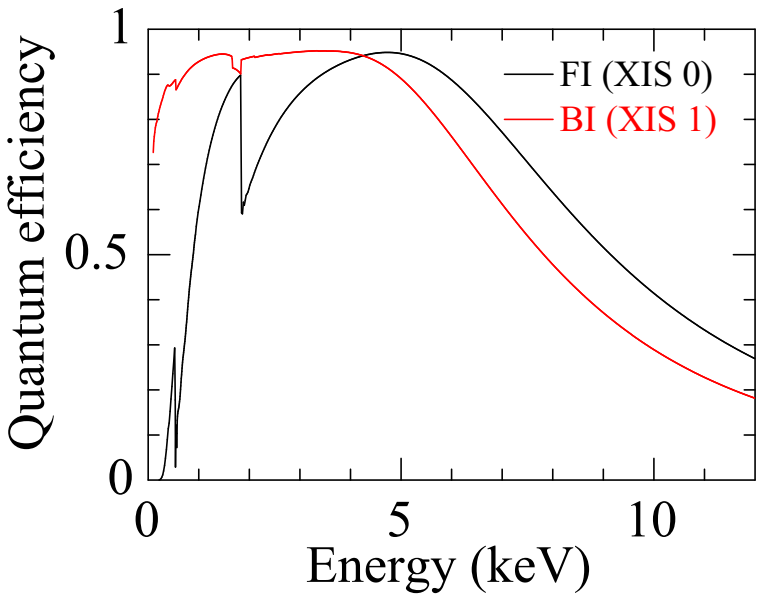

Fig. 5.10.—: Quantum efficiencies of the XIS as a function of incident photon energy. The black and red curves are for XIS 0 (FI) and XIS 1 (BI) respectively (Koyama et al. 2007a). The effect of contaminant on the OBF is not included.

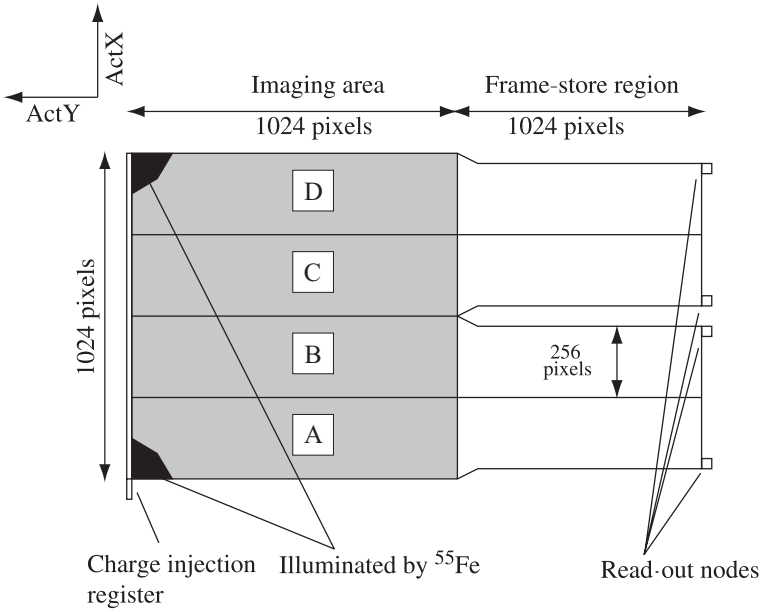

Fig. 5.11.—: Schematic view of the XIS CCD (Koyama et al. 2007a).

from the K-shell. Subsequently, fluorescent X-ray is emitted, accompanied by an L→K electron transition (Kα: 5.895 keV) or an M→K electron transition (Kβ: 6.513 keV). These sources illuminate two far corners from the read-out nodes.

5.3.2 Onboard Performance

The charge transfer inefficiency (CTI) has been increasing since the launch due to charge traps caused by radiation damage (Nakajima et al. 2008; Ozawa et al. 2009a). Consequently, the energy resolution has been degrading, which was initially of ∼130 eV at 5.9 keV in full width at half maximum (FWHM). To mitigate the degradation, spaced-row charge injection (SCI) technique is applied for almost all observations since 2006 October. In the SCI technique, electrons are injected from the furthest side from the read-out nodes to fill the traps as "sacrificial charges". This prevents charges generated by X-rays from being captured by the traps and actively reduces the CTI.

We here briefly summarize the behavior and the calibration method of CTI. The CTI consists of two components. One is CTI 1 due to slow transfer and the other is CTI2 due to fast transfer. Both the components increase with time almost linearly. The energy (original pulse height) dependence of the CTI is described with a power-law function with a time-constant index of β (Ozawa et al. 2009a). With the SCI, the CTI 1 has saw-tooth like positional dependence because CTI is discontinuously changes after each charge injection row (figure 5.12). The basic correction method of the CTI is established by Uchiyama et al. (2009).

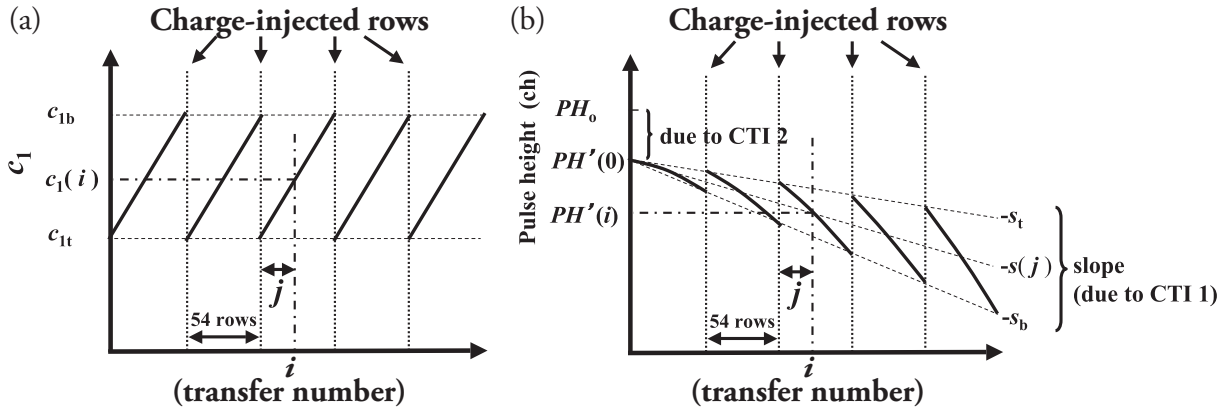

Fig. 5.12.—: The saw-tooth model of CTI 1 with SCI (Uchiyama et al. 2009). The positional dependence of CTI 1 (c_1) is modeled as shown in (a). As a result, the observed pulse height has positional dependence as shown in (b). c_{1t} and c_{1b} in (a) are the c_1 values at the peak and valley of the saw-tooth model.

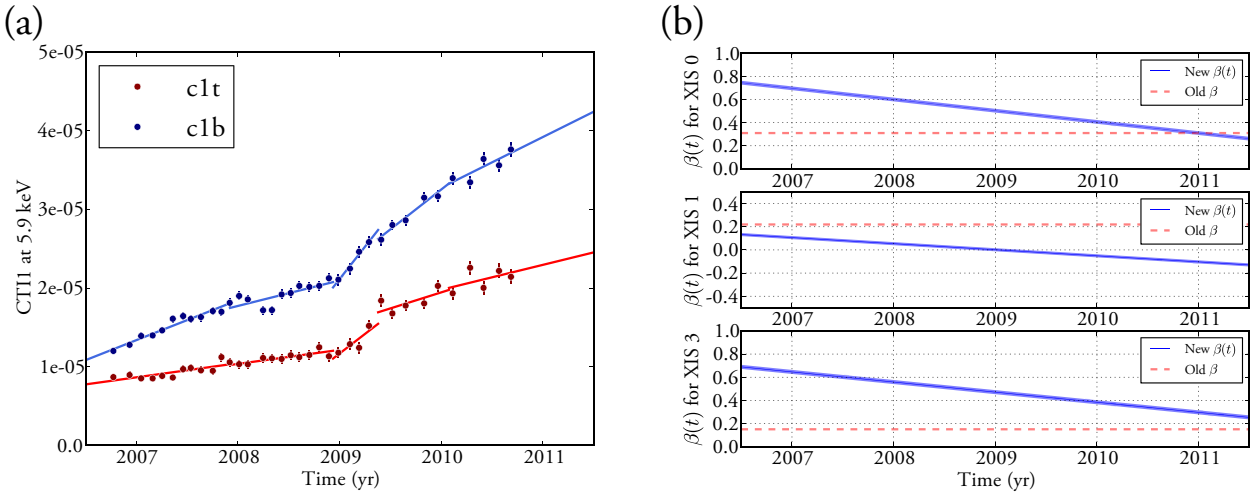

Fig. 5.13.—: The unexpected time evolution of CTI. (a) Non-linear increase of CTI 1. The case for XIS 1 segment D is shown for example. The observed values (dots) and the best-fit models (lines) considering discontinuous jumps for c_{1t} and c_{1b} are shown in blue and red, respectively. (b) Linear decrease of β derived by the calibration data (solid blue lines). The constant β values assumed in the original calibration method (Ozawa et al. 2009a; Uchiyama et al. 2009) are also shown in dashed red lines for reference.

Recent data since 2009, however, show the degradation of the accuracy in the energy scale. As shown in figure 5.13, we found (1) non-linear time increase of CTI 1 and (2) linear decrease of β from the systematic analysis of the calibration data. By taking account these unexpected behaviors of the CTI into the calibration, we successfully achieved the high accuracy of the XIS energy scale, which satisfies the calibration goal (figure 5.14). After the energy-scale calibration, we also revised the energy-resolution calibration based on indirect modeling assuming an implicit boundary condition of $\Delta E = 0$ at $E = 0$. Our new model with direct parameterizing method successfully improved the reproducibility of the energy resolution (figure 5.15). The comparison of old and new calibration accuracy in the energy scale and resolution is summarized in table 5.1.

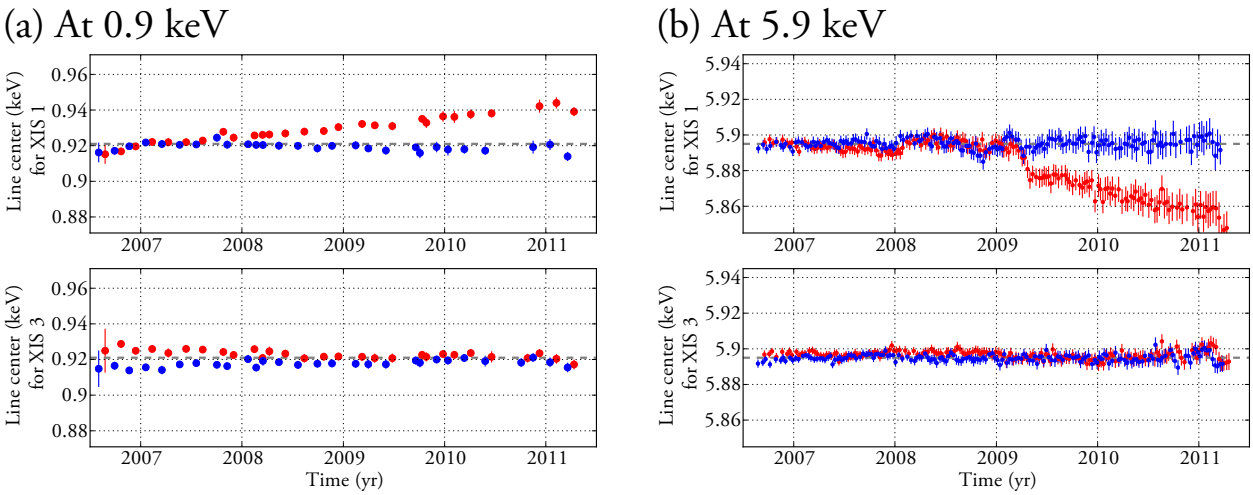

Fig. 5.14.—: Long-term trend of energy scale at (a) 0.9 keV and (b) 5.9 keV after the CTI correction. Upper and lower panels show the line center energies for XIS 1 and XIS 3, respectively. The data with different correction methods are shown: the results of the original method (Uchiyama et al. 2009) in red error bars and those of the upgraded CTI correction in blue error bars. The reference energy is also shown with dashed gray lines.

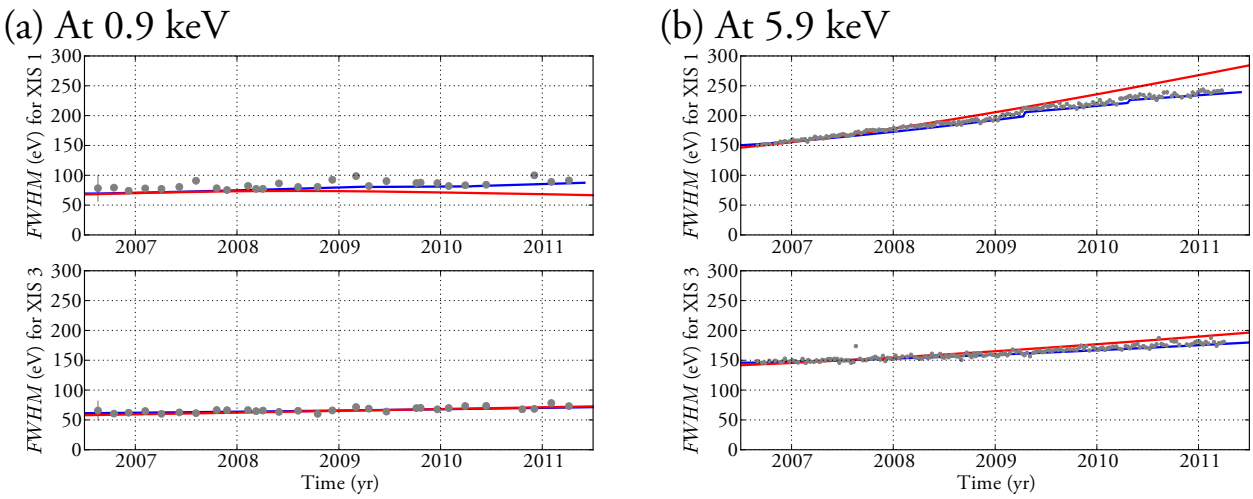

Fig. 5.15.—: Long-term trend of energy resolution at (a) 0.9 keV and (b) 5.9 keV. Upper and lower panels show $FWHM$ for XIS 1 and XIS 3, respectively. The observed data are shown with gray dots while the best-fit models with the original calibration by Uchiyama et al. (2009) and with the improved calibration method are shown with red and blue curves, respectively.

Table 5.1—: A summary of improvements on the energy scale and resolution calibration of the XIS.

Calibration item	Energy	Accuracy	
		Original∗	Upgraded
Energy scale	5.9 keV	0.5%	0.1%
	0.9 keV	2.0%	0.7%
Energy resolution	5.9 keV	16%	7.0%
	0.9 keV	21%	12%

∗ The results with the original SCI calibration by Uchiyama et al. (2009).

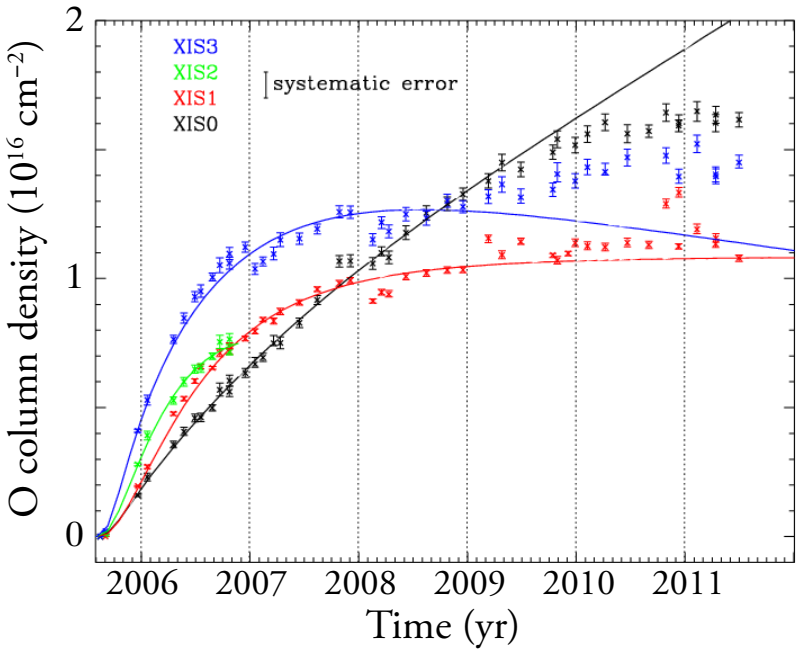

Fig. 5.16.—: Long-term trend of on-axis contaminant represented by O column density (The Suzaku technical description). An empirical model is shown in solid lines.

The low energy QE has degraded by unexpected contamination (due to out-gassing from the satellite) accumulating on the OBF (Koyama et al. 2007a). The contaminant is mainly composed of C and O. The time evolution of the contamination has been measured using calibration observations of 1E 0102–072 (figure 5.16). Although the chemical composition of the contaminant is still uncertain, it is assumed to be C/O=6 in number. The effect of contamination is included in ancillary response files made by `xissimarfgen` (Ishisaki et al. 2007).

Figure 5.17 shows the non–X-ray background (NXB) accumulated during night-earth observations. The data obtained during the South Atlantic anomaly passages and in the calibration source areas are excluded. The flux of NXB depends on the geo-magnetic cut-off rigidity (COR, figure 5.17) and the position of CCDs. The COR distribution was recently updated and is called COR2. We hereafter use COR2. Tawa et al. (2008) modeled the NXB spectra as a function of COR2. The NXB can be constructed for any observations with an accuracy of $\sim 5\%$.

On 2006 November 9, XIS 2 suddenly showed an anomaly. About 2/3 of the image was unusable due to a large amount of charge leakage. Since this anomaly, XIS 2 has been dysfunctional. Similar anomaly also occurred for XIS 0 on 2009 June 25. Fortunately, the unusable region due to the latter anomaly was located at the edge and occupies only 1/8 of the entire image. These events were possibly caused by micro-meteoroid impacts, as seen in XMM-Newton and Swift. Figure 5.18 shows the time of the anomalies of XIS 0 and 2, and the start of SCI observations. The observations presented in this thesis are also shown sequentially.

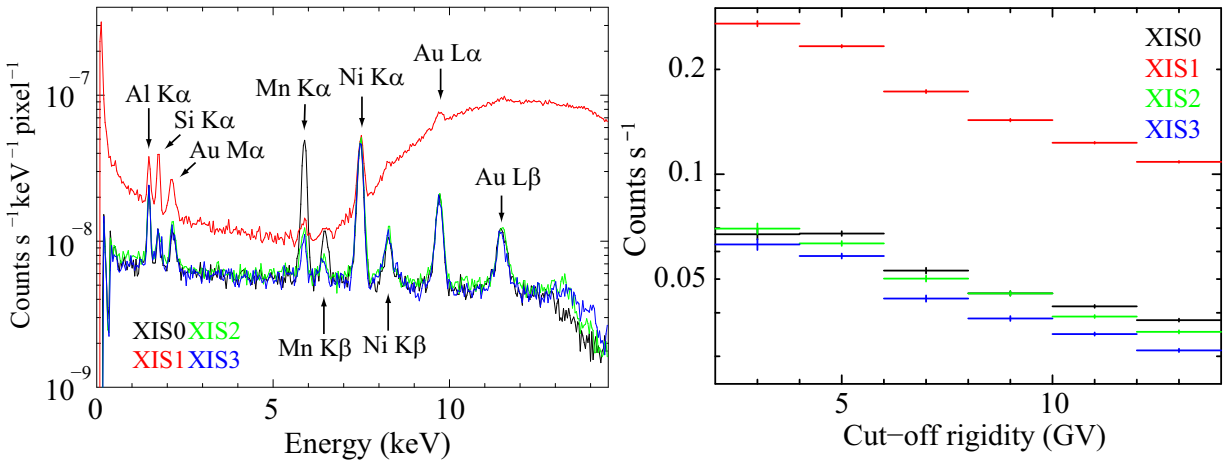

Fig. 5.17.—: XIS spectra obtained during night earth observations.

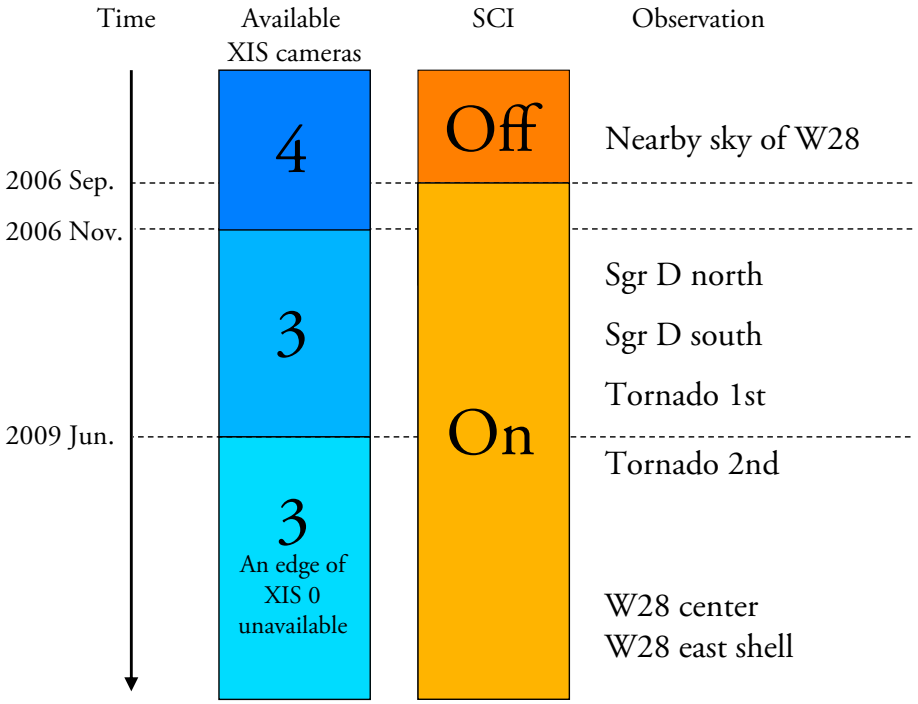

Fig. 5.18.—: History of the observing condition of the XIS.

Chapter 6

G 1.2–0.0

Contents

6.1 Objective

Sgr D is one of the most intense radio sources in the GC region known from the earliest days of GC radio observations (Downes & Maxwell 1966). It is composed of an H II region (Sgr D H II region or G1.13−0.10) and a SNR (Sgr D SNR or G1.05−0.15) adjoining each other (figure 6.1a). Low-resolution radio continuum observations (Little 1974; Swarup et al. 1974; Downes et al. 1979) identified thermal emission from the H II region and non-thermal emission from the SNR.

The Sgr D H II region is associated with its natal giant molecular cloud (GMC), which has a velocity different from those typical of GMCs in the Galactic nuclear disk such as Sgr B2 (Lis 1991; Liszt 1992). In higher resolution radio continuum images (Mehringer et al. 1998; LaRosa et al. 2000; Yusef-Zadeh et al. 2004), the Sgr D H II region is comprised of several components of different spatial scales. Throughout this chapter, we call the entire region "the Sgr D H II complex" and treat three components separately (figure 6.1a): (1) "core", the brightest knot, which is referred to as "G1.12−0.10" (Liszt 1992; Mehringer et al. 1998) or the "compact H II region" (Blum & Damineli 1999), (2) "extended", a $\sim 7'$ shell surrounding the "core" (Blum & Damineli 1999), and (3) "tail", the structure extending eastward from the "extended" component, which is labeled "G1.2+0.0" (Law et al. 2008). The "core" is an H II region with a Lyman continuum photon intensity equivalent of an O5.5 star based on its infrared properties (Odenwald & Fazio 1984; Blum & Damineli 1999). The latter two structures may be at the edge of the H II region; the "extended" component is created by ionizing photons from the "core" and the "tail" by gas escaping away from the "extended" component (Mehringer et al. 1998).

Recent observational results, however, are diverging away from this view of the Sgr D H II complex. There are two contradictory estimates of its distance. Narrow molecular line emission and broad H_2CO absorption features indicate that the complex is on the far side of the GC region (Mehringer et al. 1998), whereas the near-infrared star counts around the "core" suggest

Table 6.1—: Log of Suzaku and XMM-Newton observations of the Sgr D.

Telescope/	Sequence	Field	Aim point		Observation	Exposure
Instrument	number	name	α (J2000.0)	δ (J2000.0)	start date	time (ks)∗
Suzaku/XIS	501059010	north	$17^h48^m22^s$	$-27°56'08''$	2007/03/15	62.2/62.2
Suzaku/XIS	502020010	south	$17^h48^m46^s$	$-28°08'00''$	2007/09/06	139/139
XMM/EPIC	0112970101	obs00	$17^h48^m44^s$	$-28°05'06''$	2000/09/23	14.5/12.9
XMM/EPIC	0205240101	obs05	$17^h48^m17^s$	$-28°07'50''$	2005/02/26	28.7/16.6

∗ The exposure time after screening of XIS FI/BI for the Suzaku and EPIC MOS/pn for the XMM-Newton observations.

the system lies on the near side of the GC (Blum & Damineli 1999), possibly in the ∼160 pc expanding molecular ring (Lis 1991). The latest radio continuum study on arcminute spatial scales indicates a mixture of thermal and non-thermal emission in this complex (Law et al. 2008), which historically had been considered solely a thermal radio source.

These new lines of evidence do not support the long-standing interpretation that the Sgr D H II complex is a single H II region and its environment. Rather, it is more likely that the system is made up of multiple components at various distances projected along the same line of sight. Previous results should be carefully reviewed and new observations should be conducted to better understand the system.

X-ray observations are indispensable in this pursuit. Both SNRs and GMCs can be identified through X-ray imaging as emission extended by ∼10 pc. The two types of emission can be distinguished by their X-ray spectra; SNRs show thermal plasma with emission lines from highly ionized atoms (e.g., Becker et al. 1979), while GMCs show emission produced by external X-ray irradiation (Murakami et al. 2000). H II regions are also an emerging class of diffuse X-ray sources with a similar spatial scale. They show a variety of spectral shapes, including soft thermal (Townsley et al. 2003; Hyodo et al. 2008), hard thermal (Moffat et al. 2002; Ezoe et al. 2006), and non-thermal (Wolk et al. 2002; Law & Yusef-Zadeh 2004; Wang et al. 2006; Tsujimoto et al. 2007; Ezoe et al. 2006) emission. In addition to the X-ray emission, the measurement of the X-ray absorption gives a constraint on the distance and hence the physical scale of extended objects.

Several X-ray observations were reported in the Sgr D region. In a BeppoSAX study (Sidoli et al. 2001), diffuse X-ray emission was significantly detected from the Sgr D SNR and marginally detected from the Sgr D H II complex. In an ASCA study (Sakano et al. 2002), the image was plagued by stray lights from a nearby bright source and was unsuitable to search for diffuse X-ray sources. In an XMM-Newton study (Sidoli et al. 2006), dozens of point sources were identified, but no diffuse emission was detected presumably due to high background. The possible diffuse X-ray detection by BeppoSAX in the Sgr D H II complex has not been confirmed and no spectral information exists for this source.

We conducted X-ray observations of the Sgr D H II complex using the XIS onboard Suzaku. The low background of XIS makes it particularly well-suited for finding diffuse sources of low surface brightness and yielding their high signal-to-noise ratio spectra. Indeed, a series of XIS studies in the GC region identified several new SNRs and irradiated GMCs (Koyama et al. 2007b; Mori et al. 2008; Nobukawa et al. 2008) and reported detailed spectroscopy of an H II region (Tsujimoto et al. 2007). Upon the confirmation of the previously claimed marginal diffuse detection in the Sgr D H II complex, we further aim to construct the X-ray spectrum which gives important insights into the origin of the emission and the entire complex.

Here, we present a significant detection of diffuse X-ray emission from the Sgr D H II complex with the Suzaku XIS. High signal-to-noise ratio spectra were obtained from two different diffuse sources. We discuss their X-ray characteristics and their association with sources observed in our study using the 100 m Green Bank Telescope (GBT) and in other archived multi-wavelength data sets. Based on these data, we propose a new view of the Sgr D H II complex. In this chapter, we supplement the Suzaku data with those taken by XMM-Newton in order to evaluate the contribution of point sources to the diffuse emission.

6.2 Observations and Data Reduction

6.2.1 Suzaku

We used two XIS fields covering the Sgr D H II complex in the Suzaku GC mapping project (table 6.1). We hereafter call the two fields as north and south field (figure 6.1a). The north field covers the entire complex. The overlapping area of the north and south fields also cover a part of the complex, for which we additionally use the south field data.

In the two observations presented here, the XIS was operated in the normal clocking mode with the SCI technique. Starting from the pipeline products in the processing version 2.0, we recalculated the energy scales by taking into account of the time dependence of the CTI and the positional dependence of the SCI efficiency.[1] The resultant systematic uncertainty in the energy gain is $\lesssim$10 eV at 5.9 keV. We removed events during the South Atlantic Anomaly passages, Earth elevation angles below 5°, and Earth day-time elevation angles below 20°. We also removed hot and flickering pixels. The net exposures are 62.2 and 139 ks for the north and south fields, respectively.

6.2.2 XMM-Newton

We retrieved the archived XMM-Newton (Jansen et al. 2001) data to supplement the Suzaku data, and found that two observations taken in 2000 and 2005 cover Sgr D. We hereafter refer to them as obs00 and obs05, respectively (table 6.1). The obs05 data were presented by Sidoli et al. (2006), upon which we added the obs00 data to make deeper images. Both data sets were obtained with the European Photon Imaging Camera (EPIC), which is comprised of two MOS CCDs (Turner et al. 2001) and a pn CCD (Strüder et al. 2001).

The EPIC is sensitive in an energy range of 0.1–10 keV with an energy resolution of

[1] See (http://heasarc.gsfc.nasa.gov/docs/suzaku/analysis/sci_gain_update.html) for details.

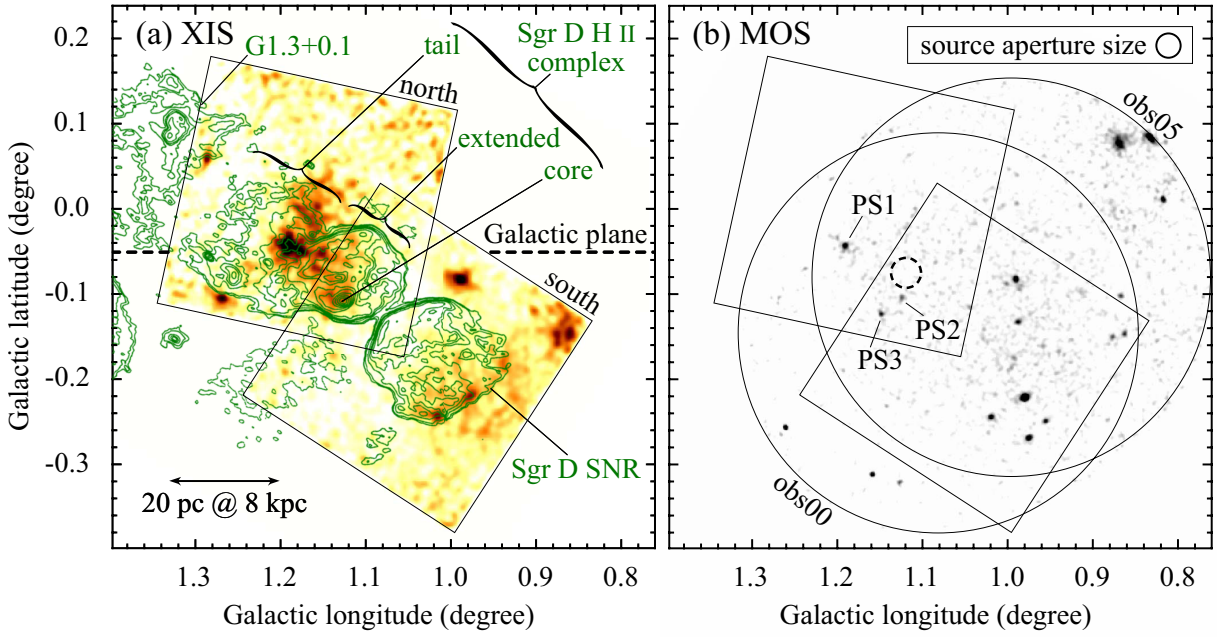

Fig. 6.1.—: Wide-band (0.7–5.5 keV) smoothed images by the (a) XIS and (b) MOS shown with the logarithmic intensity scale. Overlaid green contours in (a) are an 18 cm radio continuum map from the Very Large Array (VLA; Mehringer et al. 1998). The point source extraction aperture and background accumulation region are respectively shown with solid and dashed circles in the panel (b). For the XIS image, we merged events with the three CCDs, subtracted the NXB (Tawa et al. 2008), corrected for the vignetting, and mosaicked the two fields with different exposure times normalized. The FOVs are shown with two solid squares with 18′ in length. For the MOS image, we merged two CCDs and mosaicked the two fields with normalized exposures. The fields are shown with two circles with 30′ in diameter.

$\sim$140 eV (MOS) and $\sim$170 eV (pn) in the FWHM at 5.9 keV for the retrieved data. The MOS and pn cover a $\sim$30′-diameter circle with a pixel scale of 1″ pixel^{-1} and 4″ pixel^{-1}, respectively. The HPD and the total effective area at 8 keV are 4″.2–6″.6 at the optical axis and $\sim$900 cm^2, respectively. The combination of XMM-Newton's large effective area and imaging capability makes EPIC observations highly sensitive to point sources.

In the two observations, both the MOS and the pn were operated in the full frame mode with the medium filter. We removed events taken during periods with background rates higher than 0.5 counts s^{-1} (MOS) and 0.3 counts s^{-1} (pn) in the 10–15 keV energy band. We also removed hot and flickering pixels. The resultant effective exposures are shown in table 6.1. The XMM-Newton Science Analysis System[2] version 7.1.0 was used for reducing the EPIC data.

6.3 Analysis and Results

We reduced the data using HEASoft[3] version 6.4. In the spectral analysis, we used XSpec (Arnaud 1996) version 11.3.2 and SPEX (Kaastra et al. 1996) version 2.02.02. The redistribution matrix function released on 2006-02-13 and the auxiliary response function generated by a ray-tracing simulator (`xissimarfgen`: Ishisaki et al. 2007) were used.

6.3.1 Images

Wide-Band Images

Figure 6.1 shows the wide-band (0.7–5.5 keV) X-ray images obtained with the XIS and the EPIC MOS. Here, we restricted the energy range to be below 5.5 keV to eliminate the signals from the calibration sources in the XIS image. We find that the Sgr D H II complex is accompanied by both diffuse and point-like X-ray emission. The former is more noticeable in the XIS image while the latter is in the MOS image, reflecting the complementary capability of the two imagers.

In the MOS image (figure 6.1b), we found three bright point-like sources in and around the complex listed in the Second XMM-Newton Serendipitous Source Catalogue (Watson 2007): PS1 (2XMM J174835.9−275619), PS2 (2XMM J174841.1−280136), and PS3 (2XMM J174848.7−280100). We matched the astrometric positions between the XIS and the MOS images using bright and isolated point-like sources. The absolute astrometry of XMM-

[2]See (http://xmm.vilspa.esa.es/sas/).
[3]See (http://heasarc.nasa.gov/lheasoft/).

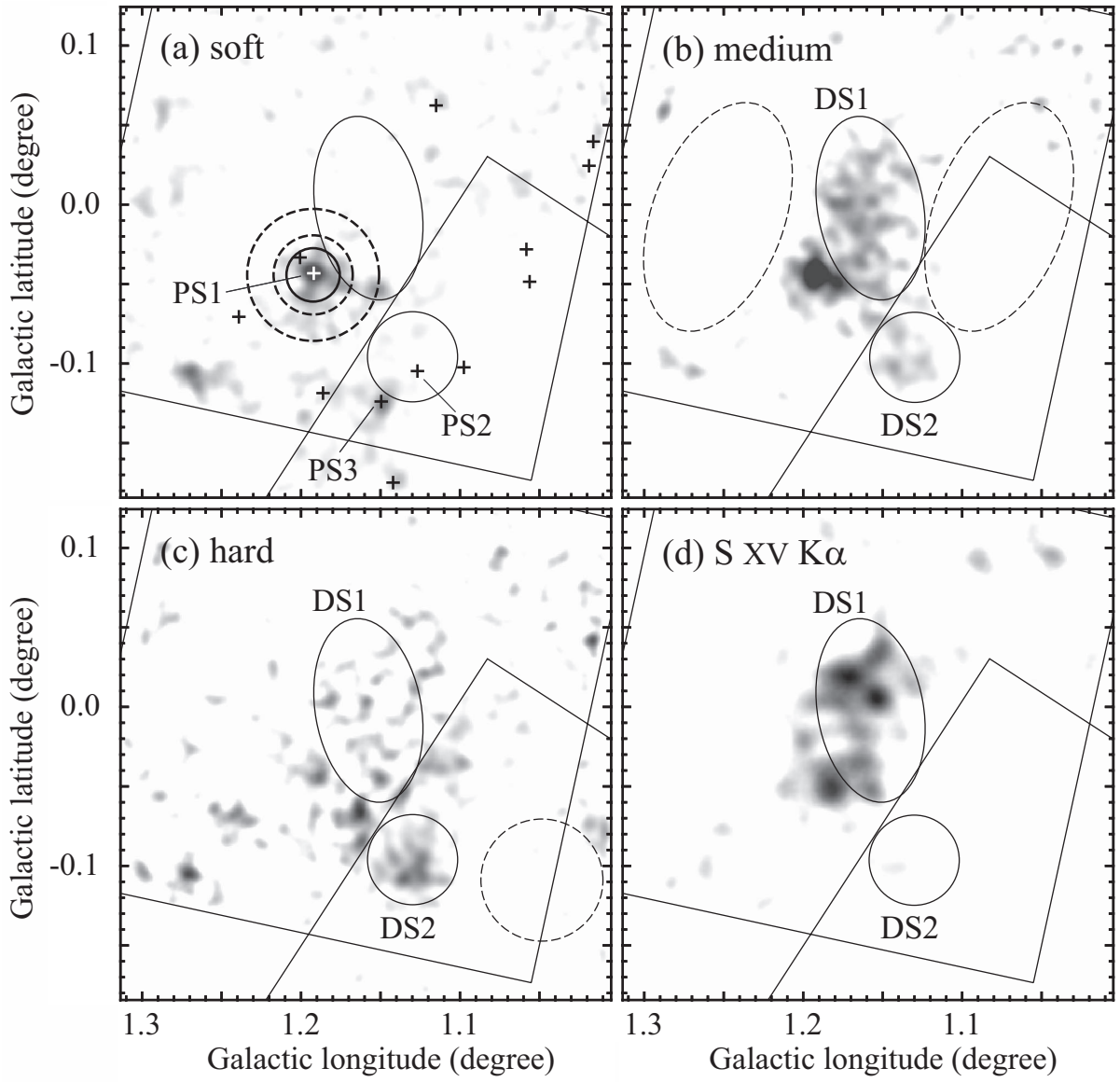

Fig. 6.2.—: Close-up XIS images of the Sgr D H II complex in various energy bands: (a) soft (0.7–2.0 keV), (b) medium (2.0–4.0 keV), (c) hard (4.0–5.5 keV), and (d) S XV Kα (2.4–2.5 keV). Crosses in (a) represent positions of point sources by XMM-Newton (Watson 2007). The source and background extraction regions are shown with solid and broken symbols, respectively; thick circles for PS1 and thin ellipses for DS1 and DS2. See § 6.3.2 for details. The images were processed in the same way as the wide-band XIS image (figure 6.1a).

Newton is accurate to $\sim 2''$[4], while that of Suzaku can be uncertain up to $\sim 20''$ (Uchiyama et al. 2008). The XIS south field was shifted to match the MOS image by (ΔR. A., ΔDec.) = ($0''$, $22''$), while the north field was unchanged as it is consistent with the MOS astrometric positions.

Band-Limited Images

XIS images were exposed for much longer times than MOS images (table 6.1). Sufficient photon counts enable us to construct both broad-band and narrow-band images with XIS. Figure 6.2 shows the close-up view of the Sgr D H II complex in four limited energy bands: (a) soft (0.7–2.0 keV), (b) medium (2.0–4.0 keV), (c) hard (4.0–5.5 keV), and (d) S XV Kα (2.4–2.5 keV).

In the three broad-band images (figure 6.2a–6.2c), PS1 appears only in the soft and medium bands, indicating that it is soft, lightly attenuated, and thus a foreground source. The soft band image lacks diffuse features. However, in the medium and hard bands, diffuse emission emerges with different colors at the north field center and at the Sgr D H II core. We consider that the two diffuse sources are different and call them DS1 and DS2 (figure 6.2).

In the narrow-band image tracing the S XV Kα line emission (figure 6.2d), PS1 and DS1 are conspicuous. These sources are likely to be thermal emission of a few keV plasma temperatures. DS2, on the contrary, is faint in this band. This reinforces the claim that DS1 and DS2 have different origins.

6.3.2 Spectra

We here present the spectra of the diffuse source using XIS. The results for the point-like sources are given in Sawada et al. (2009).

Figure 6.3 shows their background-subtracted spectra. For DS1, source photons were extracted from a region defined by the emission morphology in the S XV narrow-band image (the thin solid ellipse in figure 6.2). Spectra of faint diffuse sources are prone to uncertainties stemming from the background subtraction. We considered the following to minimize possible systematic effects. First, the data in the same observation (the north field) were used both for the source and background signals. Second, the background spectrum was constructed from two regions at the same Galactic latitude (the thin dashed ellipses in figure 6.2b) as the background is dominated by the Galactic diffuse X-ray emission (GDXE) distributed symmetrically with respect to the Galactic plane (Koyama et al. 1989; Yamauchi et al. 1990). Third, the difference

[4]See (http://xmm.esac.esa.int/docs/documents/CAL-TN-0018.pdf) for details.

in the effective area due to the different off-axis angles between the source and background regions was taken into account (Hyodo et al. 2008).

For DS2, we used both the north and south field data. The source spectrum was integrated from a $\sim$1.′7 radius to encompass the Sgr D H II core (the thin solid circle in figure 6.2). The background subtraction was performed separately in each field and then merged. In the north field, we utilized the background region for DS1, which happens to be at the symmetric position to the Galactic plane with DS2. In the south field, the background was constructed from the thin dashed circle in figure 6.2c. Other procedures follow DS1.

The spectra of DS1 and DS2 are both characterized by emission lines from highly ionized atoms (figure 6.3). Hence, we fitted the data with an optically thin thermal plasma model in CIE (Apec in the XSpec fitting package: Smith et al. 2001) attenuated by interstellar extinction (Wabs: Morrison & McCammon 1983). Because of stronger signal, we are able to derive the chemical abundances relative to solar (Anders & Grevesse 1989) for elements with conspicuous emission lines ($Z_{\rm Si}$, $Z_{\rm S}$, $Z_{\rm Ar}$, $Z_{\rm Ca}$, and $Z_{\rm Fe}$). The best-fit values are summarized in table 6.2. For DS1, we also tried a recombining plasma model by using the SPEX software version 2.02.02 (Kaastra et al. 1996). The spectra of DS1 can also be reproduced by a recombining plasma (figure 6.3b) but we found no significant improvement from the CIE model (table 6.2).

For DS2, we found that an additional Gaussian model at $\sim$6.4 keV improves the fit (F-test significance of $\sim$98%) with an equivalent width of $\sim$270 eV. More counts are necessary to confirm this.

Because the DS2 emission may largely originate from unresolved point sources, we examined time variation. Light curves in several energy bands are tested against the null hypothesis that the flux is constant using the χ^2 statistics. We found a marginal variability (significant at a $\sim$97% level) in DS2 in the north field data. For comparison, we conducted the same procedure for DS1 and the background regions. Their signals were found to be constant at high confidence levels. We thus believe that the procedure to test the time variability is reliable, and that DS2 varies.

6.4 Nature of X-ray Sources

6.4.1 Diffuse Source DS1

We first argue that the level of contamination to DS1 by point sources is negligible. The largest contaminant is PS1 among all point sources listed in the XMM-Newton catalog (pluses in figure 6.2a), but its contribution accounts only for $\sim$3% of the total XIS counts of DS1. Other point sources make even smaller contributions.

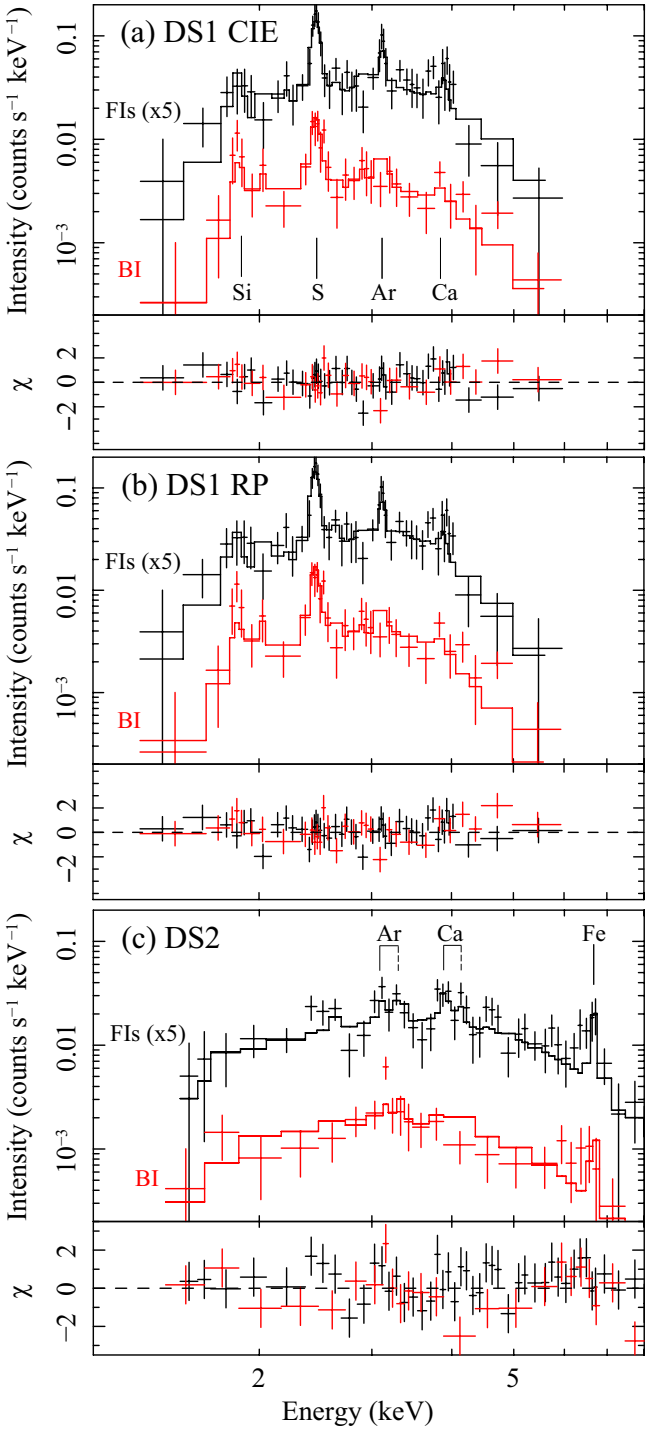

Fig. 6.3.—: Background-subtracted XIS spectra (pluses) and the best-fit models (histograms) of (a) DS1 with the CIE plasma model, (b) DS1 with the recombining plasma model, and (b) DS2 with the CIE plasma model. XIS merged FI and BI spectra are shown in black and red, respectively. Black spectra are scaled upward by a factor of 5 for clarity.

Table 6.2—: Best-fit parameters of the diffuse sources by the XIS.

Parameter	DS1		DS2
Model	CIE	Recombining plasma	CIE
$N_{\rm H}$ (10^{22} cm^{-2})$*$	$9.0^{+1.5}_{-1.5}$	$8.0^{+2.68}_{-1.47}$	$5.6^{+2.3}_{-1.0}$
kT (keV)$*$	$0.86^{+0.14}_{-0.10}$	...	$3.4^{+1.1}_{-1.2}$
$kT_{\rm e}$ (keV)$*$	...	$0.64^{+0.65}_{-0.09}$	...
$kT_{\rm z}$ (keV)$*$	...	1.06 ($<$1.37)	...
$Z_{\rm Si}$ (solar)$*$	$1.7^{+2.6}_{-1.0}$	$1.8^{+4.6}_{-0.8}$	1 (fixed)
$Z_{\rm S}$ (solar)$*$	$2.1^{+1.1}_{-0.5}$	$3.7^{+1.8}_{-1.9}$	1 (fixed)
$Z_{\rm Ar}$ (solar)$*$†	$2.1^{+0.9}_{-0.7}$	$4.5^{+3.5}_{-3.2}$	$4.8^{+4.0}_{-3.0}$
$Z_{\rm Fe}$ (solar)$*$	1 (fixed)	1 (fixed)	$0.52^{+0.41}_{-0.28}$
$f_{\rm X}$‡ (s^{-1} cm^{-2})	6.9×10^{-5}	6.9×10^{-5}	4.1×10^{-5}
$L_{\rm X}$‡§ (erg s^{-1})	1.4×10^{35}	8.8×10^{34}	6.0×10^{33}
χ^2/d.o.f.	65/73	65/72	70/65

$*$ Statistical uncertainty is represented by the 90% confidence intervals for the CIE models. For the recombining plasma model, it is represented by the 1-σ intervals.
† The values of $Z_{\rm Ar}$ and $Z_{\rm Ca}$ are fixed to one another.
‡ Values in the 0.7–8.0 keV band.
§ The absorption is corrected and the distances are assumed to be 8.0 kpc. See § 6.4.1 and § 6.4.2 for details.

We next argue that DS1 is an extended source. We retrieved optical images using the Digitized Sky Survey from the Space Telescope Science Institute[5] and near-infrared (NIR) and mid-infrared (MIR) images respectively using the Two Micron All Sky Survey (Skrutskie et al. 1997) and the Spitzer Space Telescope (Werner et al. 2004) from the Infrared Science Archive[6]. We compared these images with our X-ray image and found no stellar distribution with a morphology similar to DS1. The point source distribution in the EPIC image (figure 6.1b) differs significantly from the surface brightness distribution of DS1 in the XIS image (figure 6.1a). We thus conclude that DS1 is extended in nature, and not an ensemble of unresolved point sources.

The extinction ($\sim 9 \times 10^{22}$ cm^{-2}) derived from the X-ray spectral fit (table 6.2) indicates that DS1 is in the GC region (Baganoff et al. 2003). The apparent extent converts to $\sim 9 \times 16$ pc at an 8 kpc distance (Reid 1993). A source like DS1 has not been previously reported in the literature. It is therefore a new celestial object.

Classes of diffuse X-ray emission with an extent of $\sim$10 pc include SNRs, irradiated GMCs, PWNe (Muno et al. 2008), and H II regions (Yusef-Zadeh et al. 2002; Law & Yusef-Zadeh 2004; Wang et al. 2006; Tsujimoto et al. 2007) in the GC region. Since DS1 shows unambiguous thermal features of a $\sim$0.9 keV temperature with enhanced abundances of metals, the GMC and PWN origins are unlikely. At the position of DS1, H II regions are not known nor found in our inspection of Spitzer MIR images, which makes an H II region origin also unlikely. The XIS spectrum is akin to those found in SNRs in the GC region (Koyama et al. 2007b; Mori et al. 2008; Nobukawa et al. 2008). Thus, we propose that DS1 is X-ray emission from a new SNR. The lack of X-ray variation is consistent with the SNR interpretation.

SNRs are expected to show non-thermal synchrotron emission in centimeter bands. The Sgr D H II complex has long been considered to have thermal emission, not non-thermal emission, from the flat radio spectral indices (Downes & Maxwell 1966; Swarup et al. 1974; Little 1974; Downes et al. 1979). However, all these results were based on low resolution data, and the spectral indices were dominated by two H II regions with strong thermal emission in and around this complex; the Sgr D H II core and the other H II region to the east (G1.3+0.1 in figure 6.1a; Mehringer et al. 1998).

The latest work by Law et al. (2008) presented radio continuum maps on spatial scales comparable to the X-ray images. The spectral indices were derived from the 3.5 cm and 6.0 cm continuum maps obtained with GBT along several slices across the Sgr D H II complex. Some indices indicate that there is a mixture of thermal and non-thermal emission.

Using this GBT data set, we constructed the intensity and the spectral index profiles along

[5]See (http://archive.stsci.edu/cgi-bin/dss_form) for details.
[6]See (http://irsa.ipac.caltech.edu/) for details.

a slice including DS1 but not the Sgr D H II core (figure 6.4). The slice was taken from two images (3.5 cm and 6.0 cm) convolved to the same beam size of $\sim$2.′5. Details of the data and other reduction procedures are described in Law et al. (2008). The background-subtracted index is consistently about -0.5, indicating that non-thermal synchrotron emission dominates the spectrum (Green 2009). The radio continuum peak corresponds to the position of DS1. This result constitutes independent evidence for classifying DS1 as an SNR.

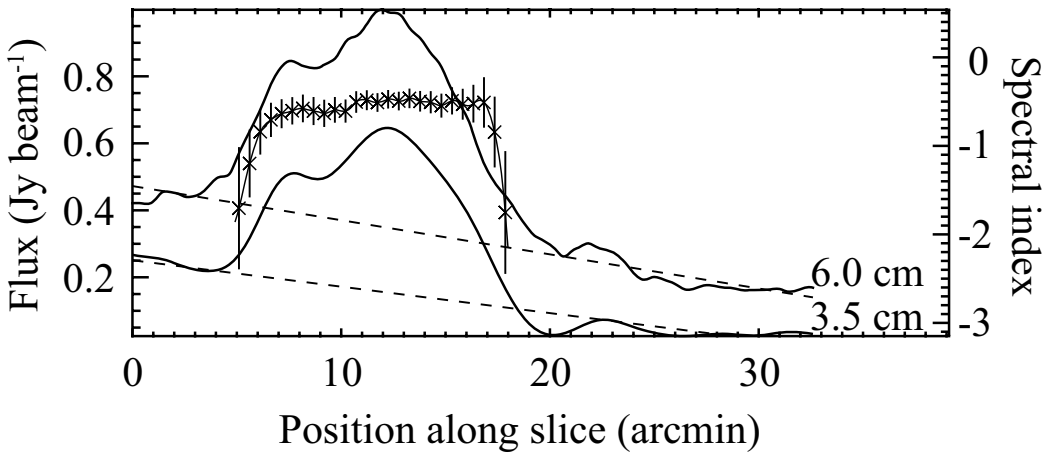

Fig. 6.4.—: Profiles of 3.5 cm and 6.0 cm intensity (solid curves) and the spectral index (crosses) between the two bands along the slice shown in figure 6.6a. Background (dashed lines) is derived by linearly fitting the slope at the two sides of the source region, where the indices are computed. The error bars indicate 1σ uncertainty.

6.4.2 Diffuse Source DS2

Similarly to DS1, we first evaluate the level of contamination by point sources. Two bright point sources (PS2 and PS3) are found in and around DS2. PS3 has a different X-ray hardness than DS2, and its contribution is minor above 2 keV (see figures 3c in Sawada et al. 2009 and 6.3b). However, the contamination by PS2 is significant. By comparing the time-averaged flux of PS2 by the EPIC and DS2 by the XIS, $\sim$ 40% of 0.7–8.0 keV counts of DS2 is attributable to PS2. Similar spectral shapes between PS2 and DS2 (see figures 3b in Sawada et al. 2009 and 6.3b) and the XIS detection of a marginal flux variation during the north field observation indicate that a significant fraction of the DS2 emission stems from PS2.

Nevertheless, PS2 alone cannot account for all properties of DS2. DS2 has an extent inconsistent with a single point source. Figure 6.5 shows the background-subtracted radial profile of DS2 around PS2 in comparison to a simulated radial profile of a point-like source. The excess emission is noticeable in the profile as well as in the X-ray image (figure 6.2c), where the diffuse emission is localized to the northeast of PS2.

The origin of the excess emission is uncertain. It can be either an ensemble of numerous unresolved point sources or the truly extended emission associated with the H II region. Considering a large concentration of stars in the Sgr D H II core (Blum & Damineli 1999; Dutra et al. 2003), the former possibility is likely. If it is of an extended nature, DS2 has quite a hard thermal spectrum for diffuse emission in H II regions, which is comparable to only a few cases (Moffat et al. 2002; Ezoe et al. 2006). The metallicity (table 6.2) above one solar is larger than diffuse X-ray emission in other H II regions (e.g. Hyodo et al. 2008), which may be due to the enhanced metallicity in the GC region (Cunha et al. 2007). The current data do not give a conclusive interpretation for this emission. Further observations are expected.

6.4.3 Structure of the Sgr D H II Complex

We now have sufficient information to decompose and deproject the Sgr D H II complex. The data are displayed in figure 6.6 with the same scale as figure 6.1. Figure 6.6a is composed of the Suzaku X-ray (0.7–5.5 keV; blue), Spitzer MIR (24 μm; green), and GBT radio continuum (6.0 cm; red) images. In this color code, SNRs appear in magenta with X-ray and non-thermal radio emission such as DS1 and the southwestern part of the Sgr D SNR. H II regions appear in yellow with MIR and thermal radio emission, which include G1.3+0.1 and another H II region inferred by Downes et al. (1979) in the northeast of the Sgr D SNR (we name this component G1.05$-$0.14). The Sgr D H II core, which has emission in all three bands, does not appear white because the Spitzer image is saturated. Figure 6.6b is a superposition of the X-ray image with millimeter emission line maps in two different velocities at the local

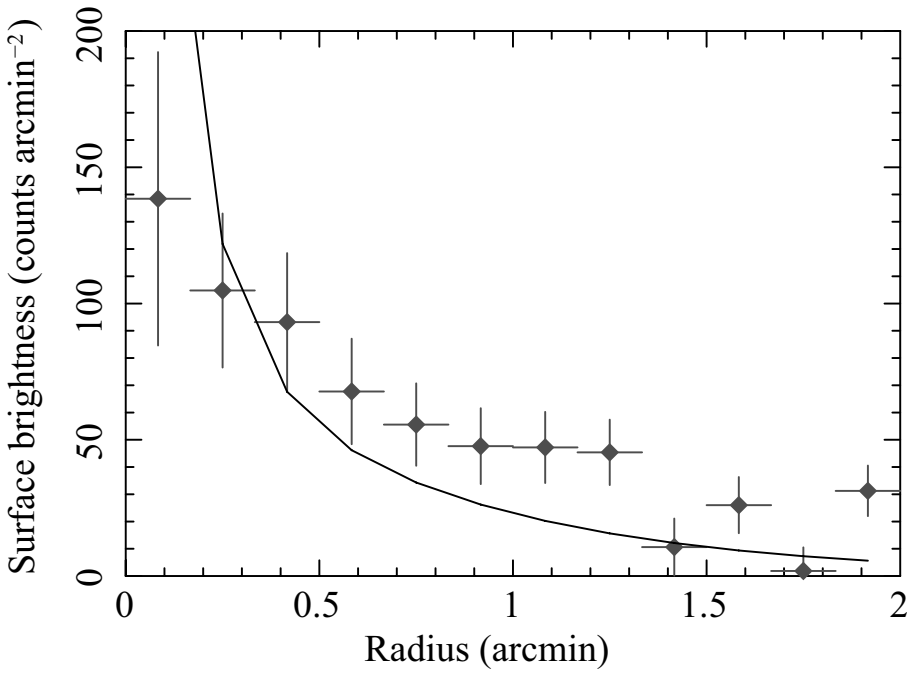

Fig. 6.5.—: Radial profile of the background-subtracted intensity around PS2 (solid pluses with dots), which is fitted with a simulated radial profile of a point-like source at the same detector position (solid curve). The energy range of 2.0–5.5 keV is used to suppress the emission by PS3. The observed profile is constructed from the north field data.

standard of rest; 100 km s^{-1} by CO (J = 3–2) in red contours (Oka et al. 2007) taken by the Atacama Submillimeter Telescope Experiment and -15 km s^{-1} by CS (J = 1–0) in blue contours (Tsuboi et al. 1999) taken by the Nobeyama 45 m telescope.

We argue that "tail" is the new SNR (we name G1.2$-$0.0) and the northwestern part of it is bright in X-ray as DS1. The X-ray morphology of DS1 is not well-correlated with the well-defined shell labeled "extended" in figure 6.1a. It is therefore unlikely that the two objects are physically related. It is more reasonable to consider that DS1 is associated with "tail". The index across "tail" is almost constant (figure 6.4), suggesting that this is a uniform structure. Both X-ray and radio properties indicate that this is an SNR. The X-ray is bright only in the western part of the imperfect shell-like morphology of the "tail". The lack of X-ray emission in other parts is attributable to an intervening GMC seen in figure 6.6b. The CO emission with a 100 km s^{-1} velocity (red contours) is anti-correlated with the X-ray emission; DS1 is just outside of the sharp boundary of the CO cloud. The extinction along this GMC is $N_{\rm H} \sim 10^{24}$ cm^{-2} from the CO data (private communication with T. Oka), which is sufficient to block the $kT \sim$0.9 keV X-ray emission behind it.

The Sgr D H II core is associated with a GMC in a different velocity (blue contours), which was suggested by Lis (1991) and Liszt (1992). Blum & Damineli (1999) proposed that "core" is a blister H II region on the GMC. We speculate that the H II region G1.05$-$0.14 is another blister on the other side of the GMC. H 109α emission was detected at this position and its velocity is the same with the GMC (Pauls & Mezger 1975).

It is now clear that Sgr D H II complex is not a single H II region and its environment as was considered in the past. We propose that an SNR and two H II regions on both sides of a GMC are projected along the same line of sight. The SNR lies behind the H II regions, which is justified by a larger $N_{\rm H}$ value in DS1 (a part of the SNR) than in DS2 ("core"). The SNR position behind the 100 km s^{-1} cloud puts this object in or behind the GC region, whereas the H II regions associated with a GMC at -15 km s^{-1} is on the near side of the GC in agreement with the NIR star count study (Blum & Damineli 1999).

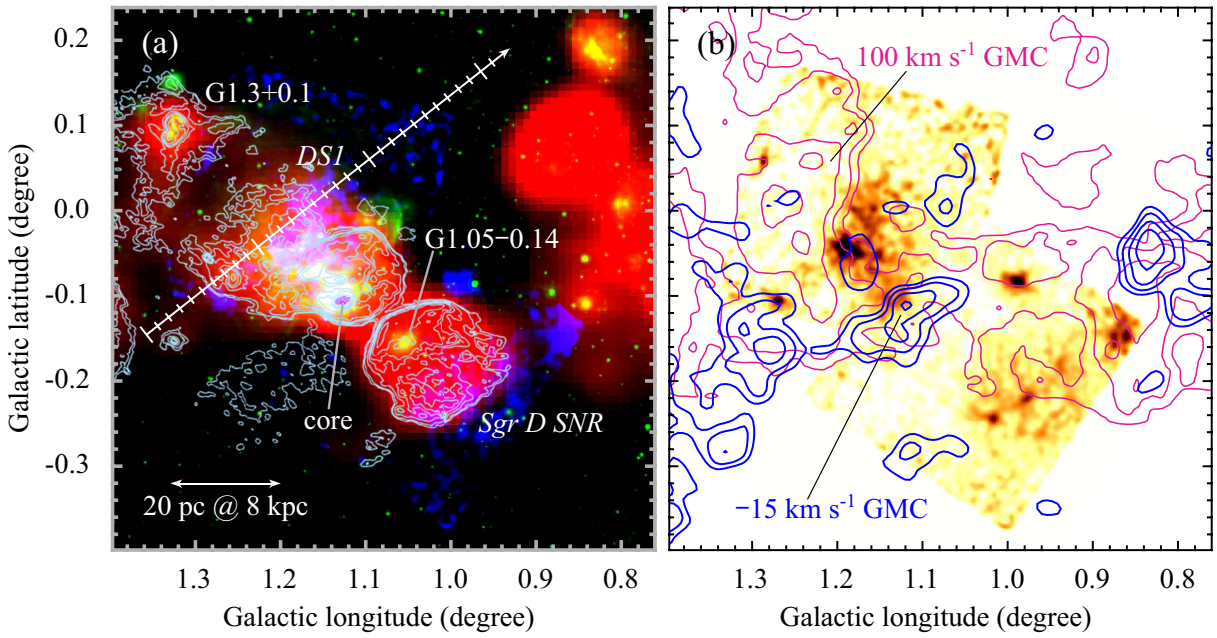

Fig. 6.6.—: (a) Composite color image with Suzaku X-ray (0.7–5.5 keV) in blue, Spitzer MIR (24 μm) in green, and GBT radio (6.0 cm) in red. The slice for the radio continuum index (figure 6.4) is shown with a ticked vector. Objects are labeled in Italic for SNRs and in Roman for H II regions. (b) X-ray image with CO ($J = 3$–2) emission at 100±5 km s^{-1} (Oka et al. 2007) in red contours and CS (J =1–0) emission at −15±5 km s^{-1} (Tsuboi et al. 1999) in blue contours.

Chapter 7

G 357.7–0.1

Contents

7.1 Objective

G 357.7−0.1 is a bright radio object near the GC direction and was first catalogued by Mills et al. (1960) as MSH 17-39. The extended, non-thermal emission with the spectral index of ~ -0.6 (Dickel et al. 1973, Slee & Dulk 1974) and the linear polarization of $\lesssim$10% (e.g. Kundu et al. 1974) placed this source as one of the Galactic SNRs.

It has an elongated shape with $\sim 10'$ length and has the brightest peak offset to one side, which is called the "head", while fainter emissions are elongated to the other side, called the "tail". Unusual structure was found with the higher resolution observations. The remarkable feature is the several co-axial filamentary arcs swirling around its major axis, and hence nicknamed as the "Tornado nebula" (figure 7.1a: Shaver et al. 1985, Becker & Helfand 1985, Helfand & Becker 1985). Stewart et al. (1994) corrected the large-scale brightness gradient of the radio map, and found a bipolar radio structure along the major axis.

The distance to the Tornado is constrained to be > 6 kpc from H I absorption measurements (Radhakrishnan et al. 1972). Recently, OH maser at 1720 MHz, supporting evidence for the shocked molecular clouds, is detected at the head (Frail et al. 1996, Yusef-Zadeh et al. 1999, Lazendic et al. 2004). From the velocity of the OH maser (-12.4 km s^{-1}), the distance is estimated to be 11.8 kpc (Frail et al. 1996). The H_2 emission lines are also detected toward the head of the Tornado (Lazendic et al. 2004).

The origin of the Tornado nebula has been controversial due to its peculiar appearance. Some scenarios are based on the head-tail structure; the center of activity is located at the brightest head and the tail is the periphery structure. The source may be either a radio galaxy with one-sided jet (Weiler & Panagia 1980, Miley 1980), a Galactic nebula powered by a pulsar, or a Galactic binary source located at the head (Shaver et al. 1985, Becker & Helfand 1985, Shull et al. 1989).

The other scenarios are along the lines of bipolar-like structure: an extragalactic double-lobed source (Caswell et al. 1989), an exotic remnant by an equatorial SN explosion of a rotating massive star (Shaver et al. 1985), or precessing jets of binary accretion system (Shaver et al. 1985, Manchester 1987, Caswell et al. 1989). The problem of these scenarios is that no compact source has been found near at the center of the Tornado.

In the X-ray band, ASCA found a hint of weak X-rays from the Tornado (Yusef-Zadeh et al. 2003a). Then Gaensler et al. (2003) discovered a diffuse X-ray source in the head with Chandra. From the centrally filled X-rays, the authors proposed that the Tornado is a Galactic MM SNR (Rho & Petre 1998). However the nature of the X-rays, whether thermal or non-thermal, was not clear due to the limited photon statistics.

In order to give further constraint on the origin from the high energy phenomena, we

Table 7.1—: Log of Suzaku observations of the Tornado

Sequence no.	Aim point		Start date	Effective exposure	Field name
	α (J2000.0)	δ (J2000.0)			
503015010	$17^h40^m07^s$	$-30°57'45''$	2008/9/19	56.8 ks	obs08 (1st)
504036010	$17^h40^m31^s$	$-30°56'56''$	2009/8/29	125 ks	obs09 (2nd)

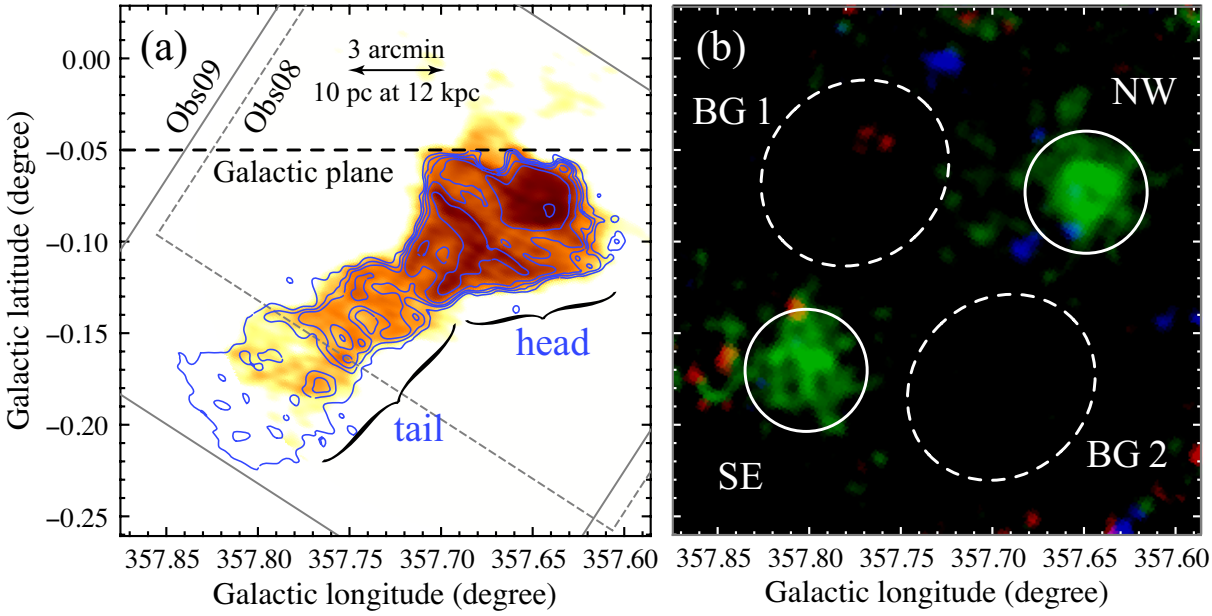

Fig. 7.1.—: (a) The 1.4 GHz radio continuum map from the Very Large Array data archives. Overlaid contours represent the radio map with the Australia Telescope Compact Array (ATCA) made by combining 4.79 and 5.84 GHz images (the fainter emission along the tail is enhanced: Stewart et al. 1994). The XIS FOVs are indicated with the solid and dashed rectangles. (b) Smoothed broad-band XIS images of the Tornado nebula: soft (0.5–1.5 keV in red), medium (1.5–3.0 keV in green), and hard (3.0–7.0 keV in blue) bands are displayed. The data from the three CCDs are merged, NXB are subtracted, and vignetting are corrected. The two fields are combined with normalization of the exposure times. Source and background extraction regions are shown with the solid and dashed ellipses, respectively.

conducted deep X-ray observations on the Tornado nebula with the XIS onboard Suzaku. We present the discovery of twin thermal plasmas associated with the head and tail of the Tornado. We investigate possible interaction of the Tornado with molecular clouds by referring the data from the Nobeyama Radio Observatory (NRO) 45-m telescope. Based on these new results, we discuss the nature of the X-ray source.

7.2 Observations and Data Reduction

The Tornado nebula was observed twice. The first observation was centered at the head region, while the second covered the whole structure of the Tornado. The observation log is given in table 7.1.

In the present observations, the XIS was operated in the normal clocking mode with the SCI technique. The data reduction was made from the pipeline processing version 2.4. We updated the gain correction method to be optimized for the SCI (Uchiyama et al. 2009) by using the makepi files version 20090915 provided by the XIS team. The systematic uncertainty in the energy scale is $\lesssim 10$ eV at 5.9 keV. We removed events during the South Atlantic Anomaly passages and Earth night-time and day-time elevation angles below 5° and 10°, respectively. We also removed hot and flickering pixels. We reduced the data using the software packages HEADAS version 6.9.

7.3 Analysis and Results

In the spectral analysis, we used Xspec (Arnaud 1996) version 12.5.1 and SPEX (Kaastra et al. 1996) version 2.02.02. The NXB data were generated by `xisnxbgen` (Tawa et al. 2008). The redistribution matrix function was generated by `xisrmfgen` and the auxiliary response function was made by a ray-tracing simulator `xissimarfgen` (Ishisaki et al. 2007).

7.3.1 X-ray Images

The NXB subtracted data were used to make the three-band X-ray images in the soft (0.5–1.5 keV), medium (1.5–3.0 keV), and hard (3.0–7.0 keV) bands. Figure 7.1b shows the results after the vignetting correction. We see two diffuse emissions only in the medium band (1.5–3.0 keV). We hereafter call these sources as "NW" and "SE". The apparent sizes of NW and SE are $\sim 4'$, which are larger than the HPD of the Suzaku XRT ($\sim 2'$). Thus these X-ray sources are not single point sources, but diffuse or ensemble of multiple point sources. We

then searched for X-ray point sources in the source areas from the Chandra Catalog (Evans et al. 2010), and found only one Chandra point source in the SE area. The flux is only 0.7% of the total flux (after the background subtraction; see § 7.3.2 and § 7.3.3) in the SE area in the 1.2–7.0 keV band. We further made the X-ray light-curve from the NW and SE areas, and found no time variability of these sources. Thus NW and SE must be extended sources.

7.3.2 Background Selection

The background X-rays in the source (NW and SE) areas are mainly due to the Galactic diffuse X-ray emission (GDXE), because the two sources are near the GC and the Galactic plane. The flux (surface brightness) of the GDXE smoothly decreases with increasing distances from the GC and the plane, while the spectrum shape has no significant position-to-position variation (e.g., Uchiyama et al. 2011). In order to investigate the flux and spectrum variation near the source fields, we selected two background regions from the nearby blank sky (BG 1 and BG 2: broken ellipses in figure 7.1). Figure 7.2 shows the NXB-subtracted spectra of BG 1 and BG 2. We see that the over-all spectral structures and fluxes are very similar to each other.

For the quantitative study, we conducted spectral fittings with the following process. The GDXE is known to exhibit strong K-shell lines from highly ionized Si, S, and Fe (Yamauchi & Koyama 1993). In fact, the XIS spectra of BG 1 and BG 2 clearly exhibit the highly ionized Si, S, and Fe K-shell lines. The co-existence of these lines indicates that the spectra require at least two temperature plasmas.

The previous studies on the GDXE near the GC direction (e.g., Muno et al. 2004, Ryu et al. 2009) showed that the GDXE spectra can be fitted with two plasmas in collisional ionization equilibrium (CIE): a low-temperature ($kT \sim 1$ keV) CIE for the Si and S lines, and a high-temperature ($kT \sim 6$ keV) CIE for the Fe line. We therefore applied a two-temperature CIE plasma model by using the Apec code (Smith et al. 2001). We also included a Gaussian in the GDXE as a Kα emission line at 6.40 keV from neutral irons (Fe I), which is also found in the GDXE (e.g., Koyama et al. 2007c). These three components are attenuated by interstellar extinction (Wabs: Morrison & McCammon 1983) toward the GC distance. Then, the GDXE is written as:

$$\mathrm{Wabs}\,1 \quad \times \quad (\mathrm{Apec}\,1 + \mathrm{Apec}\,2 + \mathrm{Gaussian}). \tag{7.1}$$

The temperatures (kT), chemical abundance of metals (Z) relative to the solar values (Anders & Grevesse 1989), the volume emission measures of the plasmas, the surface brightness of Fe I Kα line ($S_{6.4}$), and the hydrogen-equivalent column density of the absorbing materials (N_{H}) were free parameters.

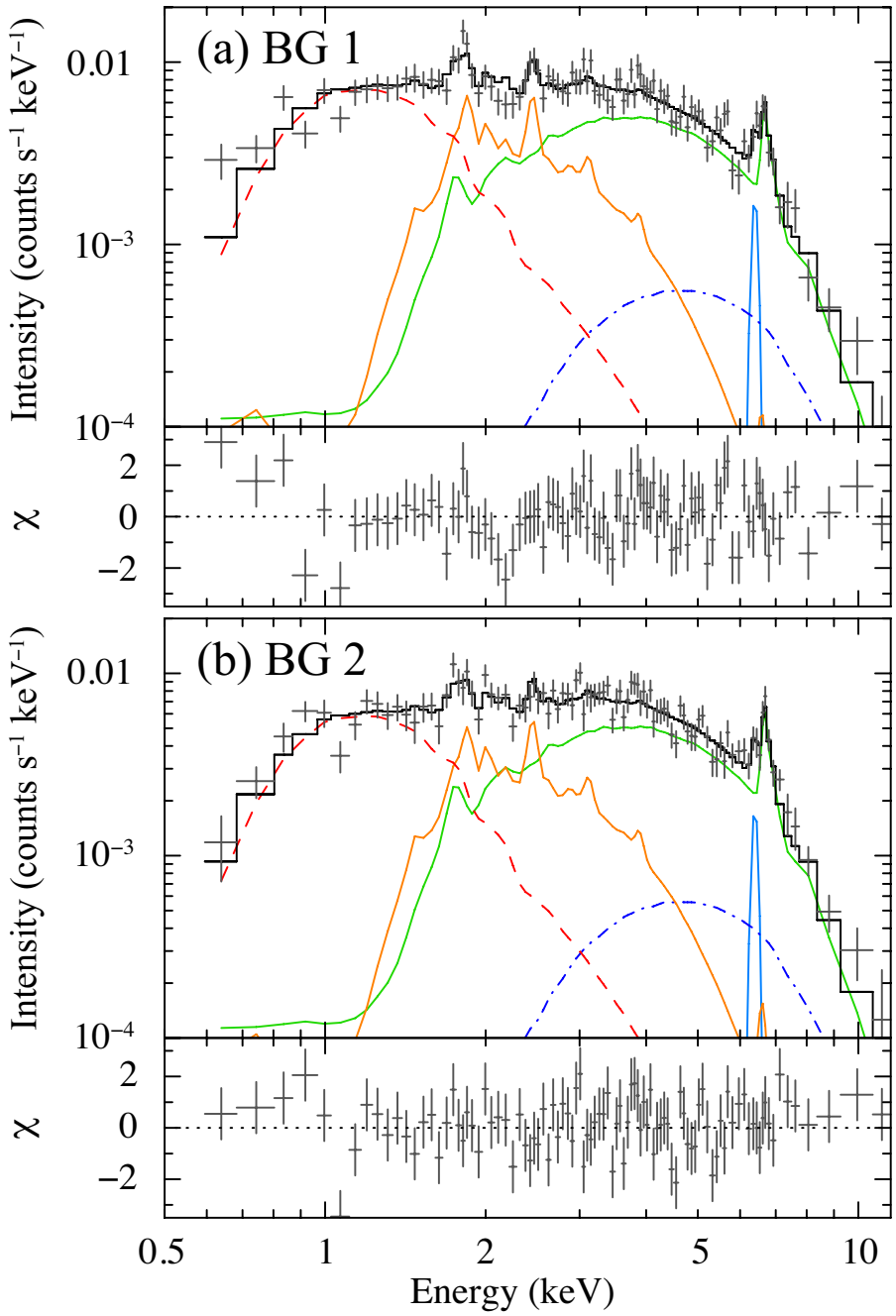

Fig. 7.2.—: (a) The NXB-subtracted spectra (gray crosses) and the best-fit models (black histograms) of BG 1. The difference of effective area between the two is corrected and only the results of FIs are shown for simplicity. The solid, dashed, and dash-dotted curves represent contributions from the GDXE, the foreground emission, and the CXB, respectively. (b) Same as panel (a), but for BG 2.

As is seen in figure 7.1, the spectra of BG 1 and BG 2 exhibit significant emission in the soft band (0.5–1.5 keV). If these soft X-rays come from the GDXE, the X-rays should be heavily attenuated by interstellar extinction toward the GC distance. Therefore the soft X-rays are mainly foreground emission. The soft X-rays are also observed near the GC region ($|l| < 1^\circ$) by Ryu et al. (2009). They found that the soft X-ray emission is almost uniform within the central one degree on the plane. They applied the model below:

$$\mathrm{Wabs}\,2 \times \mathrm{Apec}\,3. \tag{7.2}$$

Since the absolute Galactic latitude of the Tornado fields are close to that of the region of Ryu et al. (2009), we can reasonably assume that the typical parameters for the soft X-ray spectrum are same as those of Ryu et al. (2009): the plasma temperature of 0.9 keV, the chemical abundance[1] of $5 \times 10^{-3}\ Z_\odot$, and the hydrogen-equivalent absorption column of 2.0×10^{21} cm^{-2}. Thus for the foreground soft X-ray spectrum, only the normalization was a free parameter.

The other background component, the Cosmic X-ray background (CXB), is isotropic and

[1]Since the true origin of the foreground emission is unknown at present, we applied a phenomenological model, which gives a reasonable fit to the data. Therefore apparent low abundances in this model should not be taken seriously.

Table 7.2—: Best-fit parameters of the background emission.

Parameter	BG 1	BG 2
— Low temperature plasma —		
kT (keV)	$0.90^{+0.17}_{-0.19}$	$0.96^{+0.22}_{-0.17}$
Norm$*$	$8.7^{+9.6}_{-3.4}$	$6.4^{+3.6}_{-2.6}$
— High temperature plasma —		
kT (keV)	$6.5^{+1.3}_{-1.3}$	$6.5^{+1.2}_{-0.7}$
Norm$*$	$2.3^{+0.6}_{-0.4}$	$2.4^{+0.4}_{-0.3}$
— Common Parameters —		
$S_{6.4}$†	$3.8^{+1.8}_{-1.7}$	$3.8^{+1.6}_{-1.7}$
Z (solar)	$0.53^{+0.16}_{-0.14}$	$0.58^{+0.15}_{-0.13}$
$N_{\rm H}$ (10^{22} cm^{-2})	$5.2^{+0.8}_{-0.6}$	$5.3^{+0.6}_{-0.5}$
Foreground Norm$*$	$1.1^{+0.1}_{-0.1}$	$0.91^{+0.06}_{-0.06}$
χ^2/d.o.f.	201/171	190/171

$*$ The normalized volume emission measure (VEM) represented as $10^{-7} \times \frac{VEM}{4\pi d^2 \cdot A}$ cm^{-5} arcmin^{-2}, where d and A are the distance and the solid angle of plasma, respectively.

† The average surface brightness in the unit of 10^{-8} photons s^{-1} cm^{-2} arcmin^{-2}.

we adopted the empirical form, an absorbed power-law:

$$\mathrm{Wabs3} \times C \times (E/\mathrm{keV})^{-\Gamma}, \tag{7.3}$$

where C is the normalization constant at 1 keV and Γ is the photon index of the power-law. These were fixed to be $C = 7.4 \times 10^{-7}$ photons s^{-1} cm^{-2} arcmin^{-2} and $\Gamma = 1.486$ according to Kushino et al. (2002). Since the CXB should be absorbed by the ISM throughout the whole Galaxy, we assumed the hydrogen-equivalent absorption column toward the CXB to be twice of that for the GDXE ($N_{\rm H}$).

In the model fitting, all the free parameters were allowed to be independent between the two regions, BG 1 and BG 2. The model fit was acceptable for both the spectra. The results are shown in figure 7.2 and the best-fit parameters are listed in table 7.2.

We found that the best-fit parameters for the GDXE components are all consistent between BG 1 and BG 2 within the statistical errors, and hence can assume that the background spectrum and flux are essentially constant near at the source areas. We therefore merged BG 1 and BG 2 to increase statistics. The best-fit $N_{\rm H}$ for the merged spectrum is $(5.3 \pm 0.4) \times 10^{22}$ cm^{-2}.

Table 7.3—: Best-fit parameters of the diffuse sources.

Parameter	NW	SE
$N_{\rm H}$ (10^{22} cm^{-2})	$6.6^{+1.1}_{-0.8}$	$7.4^{+1.7}_{-1.4}$
kT (keV)	$0.73^{+0.15}_{-0.15}$	$0.59^{+0.18}_{-0.15}$
Z (solar)$*$	$0.89^{+0.37}_{-0.28}$	$1.7^{+1.3}_{-0.7}$
$S_{\rm X}$†	$2.8^{+0.2}_{-0.2}$	$2.4^{+0.2}_{-0.2}$
$L_{\rm X}$‡	$2.4^{+0.1}_{-0.1}$	$3.6^{+0.3}_{-0.3}$
χ^2/d.o.f.	85/82	49/41

$*$ The chemical abundance of Si, S, and Ar relative to the solar values. The abundances of the other elements are fixed at the solar values.
† The average surface brightness in the unit of 10^{-6} photons s^{-1} cm^{-2} arcmin^{-2} in the 0.5–7.0 keV band.
‡ The luminosity in the unit of 10^{35} erg s^{-1} in the 0.5–7.0 keV band. The absorption is corrected and the distances are assumed to be 12.0 kpc (see § 7.4.1).

7.3.3 Spectra of NW and SE

We extracted the spectra from the NW and SE regions (solid circles in figure 7.1b), then subtracted the NXB and merged-background spectra. Figure 7.3 shows the background-subtracted spectra of NW and SE. We clearly see several emission lines from highly ionized

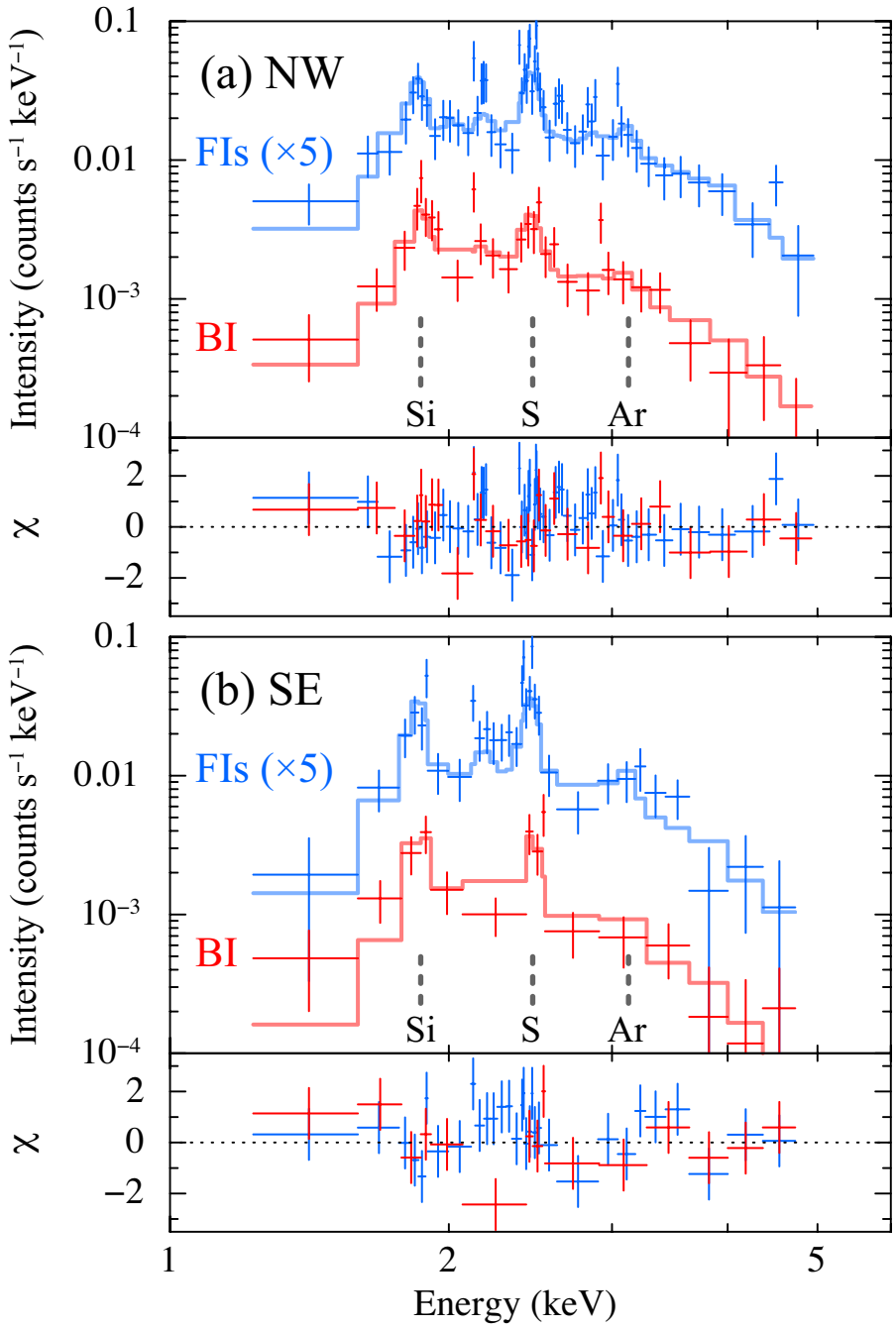

Fig. 7.3.—: (a) The background-subtracted spectra for NW. The FI and BI spectra are separately given by blue and red crosses, respectively. For visibility, the FI spectrum is multiplied by 5. The blue and red histograms are the best-fit model of FI and BI spectra, respectively. (b) Same as panel (a) but for SE.

atoms, Si, S and Ar. We therefore fitted the spectra with an optically thin thermal plasma

model in CIE (Apec) absorbed by the ISM (Wabs). Free parameters were the chemical abundances of Si, S, and Ar, the temperatures and normalization of the CIE plasma, and absorption ($N_{\rm H}$). The abundances of the elements other than Si, S, and Ar were fixed to the solar values. All the abundances in the absorbing materials were also fixed to be solar. With this model, we obtained satisfactory fits both for NW and SE (figure 7.3). The best-fit parameters are given in table 7.3.

7.4 Nature of the X-ray Sources

7.4.1 Association to the Tornado

We find that the absorption column densities ($N_{\rm H}$) for the NW and SE sources are very similar to each other (table 7.3). Since the $N_{\rm H}$ values for the GDXE near the source region are almost constant at $(5.3 \pm 0.4) \times 10^{22}$ cm^{-2}, the same $N_{\rm H}$ values for NW and SE supports that the two sources are located at nearly the same distances.

Assuming that the distance of the GDXE is 8 kpc and that the ISM density along the line-of-sight is constant, the distances of NW and SE can be estimated by the $N_{\rm H}$ ratio relative to the background emission of $(5.3 \pm 0.4) \times 10^{22}$ cm^{-2} as $10.0^{+1.8}_{-1.4}$ and $11.2^{+2.7}_{-2.3}$ kpc, respectively. These distances are almost consistent with the radio distance of the Tornado ($\sim$12 kpc; Frail et al. 1996). In the projected image, the radio emission of the Tornado appears to be associated with the two X-ray structures at the both ends (see figure 7.4). Thus we argue that the two X-ray sources are physically connected to the Tornado nebula.

The two diffuse sources are found to exhibit optically thin thermal nature. In fact, the X-ray emissions from the sources are described with CIE plasmas of nearly the same temperatures (0.6–0.7 keV). The abundances are consistent with the solar values. This indicates that the X-ray emitting materials mainly consist of ISM. If the distance of the Tornado is 12 kpc, the X-ray source size of $4'$ corresponds to 14 pc. Assuming a spherical shape with uniform density, we derive the physical parameters of the NW and SE plasmas, electron density ($n_{\rm e}$), mass (M) and total thermal energy ($E_{\rm th}$), as are listed in table 7.4.

We found no hint of non-thermal emission from the NW and SE sources. Assuming the photon index of 2, we obtained the 3-σ upper limits of the luminosities of non-thermal X-rays to be 1.1% and 2.0% of those of the thermal plasmas in the 0.5–7.0 keV band for NW and SE, respectively.

We also examined whether the sources are in a NEI state such as ionizing plasma and recombining plasma. In this analysis, we merged the two spectra of NW and SE to increase statistics. The merged spectra are shown in figure 7.5. We found that the merged spectra can

Table 7.4—: Physical parameters of the X-ray emitting plasma.

Parameter	NW	SE
VEM (10^{58} cm^{-3})$*$	1.0	1.5
$n_{\rm e}$ (cm^{-3})	0.49	0.59
M ($M_\odot$)	23	29
$E_{\rm th}$ (10^{49} erg)	8.3	8.2

$*$ These values are taken from the best-fit model in table 7.3 at the distance of 12 kpc.

be described as ionizing plasma rather than recombining plasma. The best-fit values of the electron and ionization temperatures are $0.92^{+0.12}_{-0.06}$ keV and $0.32^{+0.09}_{-0.07}$ keV, respectively. The ionizing plasma model slightly improves the fit (χ^2/d.o.f $= 120/83$) compared to the CIE plasma model (χ^2/d.o.f. $= 134/84$). We note that the physical parameters such as thermal energy do not change drastically even if we prefer the ionizing plasma model.

7.4.2 Bipolar Structure of the Tornado Nebula

The two X-ray plasmas are located at the both ends (head and tail) of the symmetric (bipolar-like) radio structure found by Stewart et al. (1994). Since the properties of the X-ray plasmas are almost identical, these would be the twins formed by a common process. A plausible scenario is that the X-ray plasmas have been generated by the termination shocks at the intersecting molecular clouds. In fact the shocked molecular cloud associated with the Tornado has been found near NW (Frail et al. 1996). To confirm the cloud interactions, we further search for the molecular structure near at the NW and SE regions using the data of CO $J=$1–0 taken with the NRO 45-m telescope (private communication with T. Oka). The results in the velocity range of 11 ± 1 km s^{-1}, close to the velocity of the OH maser near at NW, are shown in figure 7.4. We clearly see CO counterparts near NW (MC 1) and SE (MC 2).

As we described in § 7.1 (Objective), many ideas for the origin of the Tornado have been proposed. The present result that the Tornado has bipolar X-rays at the head and tail excludes most of these scenarios. In the following sections (§ 7.4.3 and § 7.4.4), we discuss two plausible origins.

7.4.3 Bipolar Jet from a Binary Accretion System

One possibility is that the Tornado is made by bipolar jets from a binary accretion system. The filamentary radio arcs swirling around the major axis would be due to the precession of jets

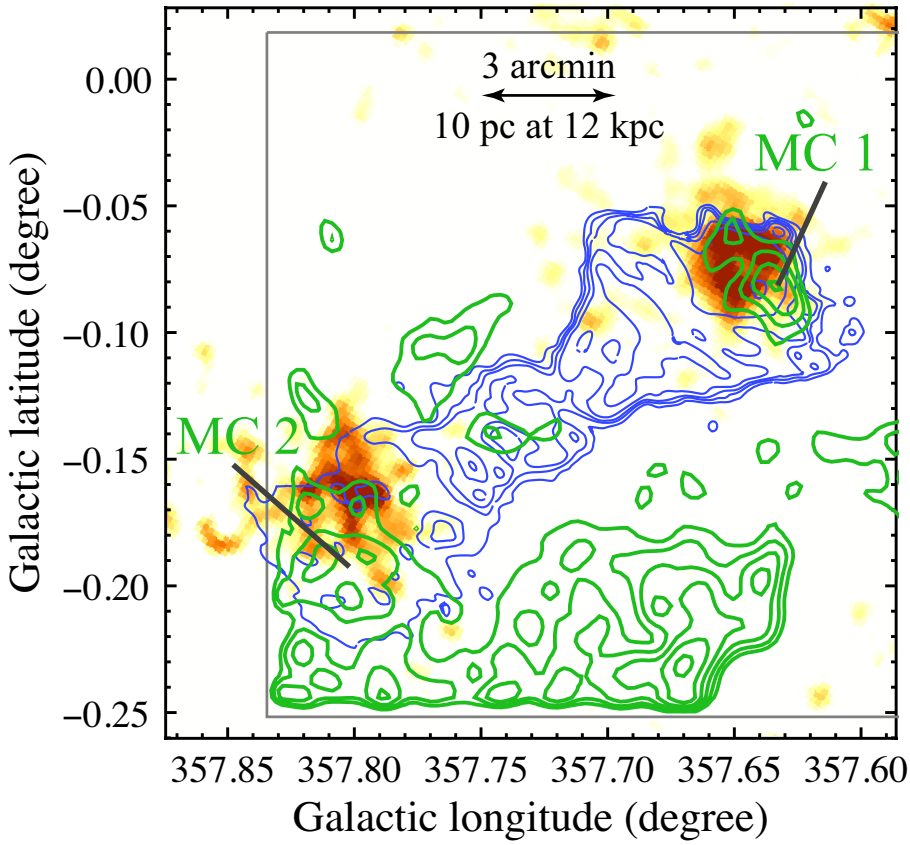

Fig. 7.4.—: Multi-wavelength image of the Tornado nebula: the medium band (1.5–3.0 keV) image overlaid with contours of the radio continuum emission with the ATCA (blue) and CO J=1–0 ($V_{\rm LSR} = -11 \pm 1$ km s^{-1}) with the NRO 45 m telescope (green). The FOV of the NRO observation is shown with the solid rectangle.

as is found in SS 433. The twin X-ray emitting plasmas are made by the shock with molecular clouds. Bipolar jets have usually a bright central power source, but no X-ray source is found from the center of the Tornado nebula. We set the 3-σ upper limit on the luminosity to be 1.9×10^{33} erg s^{-1} in the 0.5–10.0 keV band, assuming the absorption column of $N_{\rm H} = 7 \times 10^{22}$ cm^{-2}, the power-law spectrum with the photon index of 2, and the distance of 12 kpc. Chandra has gave more severe constraint of $\sim 1 \times 10^{33}$ erg s^{-1} (Gaensler et al. 2003). These upper limits are only less than 1% of NW and SE luminosities of 2.4×10^{35} erg s^{-1} and 3.6×10^{35} erg s^{-1}, respectively. A plausible explanation for the non-detection of the bright central source is that putative binary went into a quiescent state after forming jet-structures in a past active phase.

The synchrotron cooling timescale (Reynolds 1996) for electrons which emit $\epsilon_{\rm syn}$ keV photons in a magnetic field B G is estimated to be,

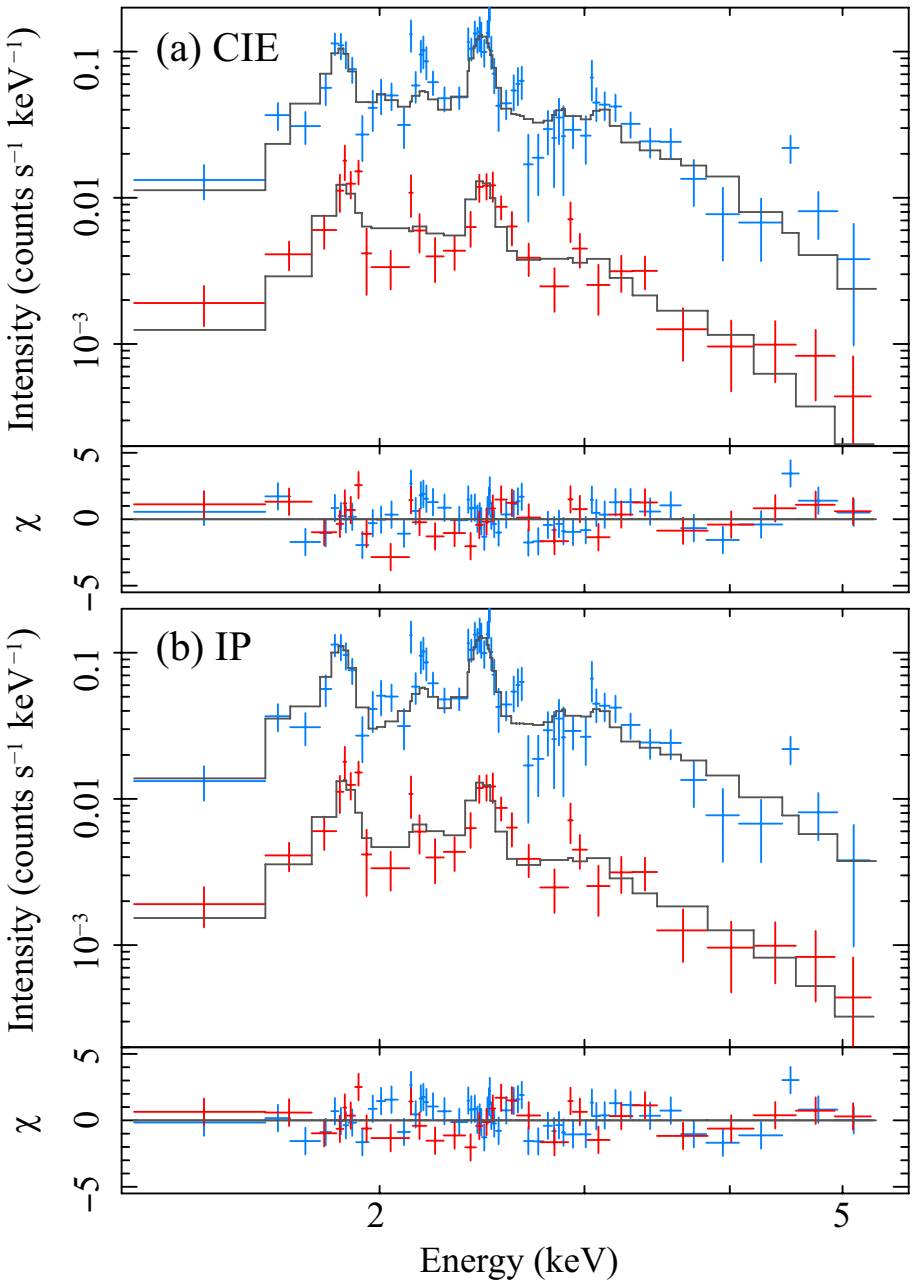

Fig. 7.5.—: (a) The merged spectra of NW and SE with the CIE model. (b) Same as panel (a) but with the ionizing plasma model. Symbols follow figure 7.3.

$$\tau \approx 2000 \left(\frac{B}{10\ \mu\mathrm{G}}\right)^{-\frac{3}{2}} \left(\frac{\epsilon_{\mathrm{syn}}}{1\ \mathrm{keV}}\right)^{-\frac{1}{2}} \text{ years.} \tag{7.4}$$

Assuming the magnetic field of 100 μG (Law et al. 2008), the cooling timescale for ≥ 1 keV

photons is estimated to be less than ∼40–50 years. The lower energy electrons responsible for the radio synchrotron radiation can survive much longer time. The cooling time of the X-ray emitting plasma, which are made by the interaction between the jets and the molecular clouds, is also much longer. Thus the radio Tornado and the twin X-rays at the both ends would be fossil radiations of a past activity some ∼40–50 years ago. Although such object is very rare, we see a hint in the jets of 4U 1755−33. The central source is in low luminosity of 3.6×10^{31} erg s^{-1} at present, but was bright two decades ago (Angelini & White 2003, Roberts et al. 1996).

7.4.4 Remnant of an Equatorial Explosion

An alternative possibility for the bipolar structure of the Tornado is a remnant of an equatorial explosion of a rotating high mass star (Shaver et al. 1985). For example, a hypernova explosion associated with a γ-ray burst may produce a bipolar blast wave (Ioka et al. 2004). If this blast wave hits molecular clouds, then the double X-ray spots will be produced. This scenario does not necessarily require a central source.

A hypernova is very energetic ($\sim 10^{52}$ erg). In our case, however, the thermal energy in the plasma is less than 10^{51} erg (table 7.4). Hence, if this scenario is true, a large fraction of the explosion energy would have gone into the acceleration of cosmic rays and/or the bulk motion of the molecular clouds.

Chapter 8

W28

Contents

8.1 Objective

W 28 (G 6.4−0.1), a bright MM SNR, exhibits the two conditions, which is commonly shared by all of the recombining SNRs. A shock interaction with the ambient gas indicated by the expanding H I shell (Velázquez et al. 2002), broad CO, CS, and H_2 emission lines (Arikawa et al. 1999; Reach et al. 2005), and OH (1720 MHz) masers (Yusef-Zadeh et al. 2003b). Also the GeV and TeV γ-rays were detected (Abdo et al. 2010b; Aharonian et al. 2008).

From the estimated distance of 1.9±0.3 kpc (Velázquez et al. 2002), the angular size of $\sim$50′ is $\sim$30 pc. The large size, possible association to the nearby pulsar (Kaspi et al. 1993), and dynamical evolution of the H I shell (Velázquez et al. 2002) constrain the age of W 28 to be 33,000–150,000 yr.

ROSAT and ASCA mapped the entire remnant in the X-ray band (Rho & Borkowski 2002) and found center-filled structure with partial shells at the northeast and southwest. The X-ray spectrum in the central region had hard X-ray emissions up to $\sim$ 7 keV with the Fe Kα line, and was fit with a two temperature plasma of 0.67 keV and 1.8 keV in CIE or ionizing. Thus no hint of recombining plasma has been reported from W 28, although this SNR shares the common features with the three SNRs of recombining plasmas. The aim of this chapter is to search for and quantitatively study recombining plasmas with superior energy resolution and large effective area of the XIS onboard Suzaku. We adopt 2 kpc for the distance of W 28.

Table 8.1—: Log of Suzaku observations of W 28.

Sequence no.	Aim point		Start date	Effective	Field name
	α (J2000.0)	δ (J2000.0)		exposure	
505005010	$18^h00^m17^s$	$-23^\circ21'59''$	2010/04/03	73.0 ks	Center
505006010	$18^h01^m29^s$	$-23^\circ17'08''$	2011/02/25	100 ks	East shell
500008010	$18^h03^m49^s$	$-22^\circ01'03''$	2006/04/07	40.7 ks	Nearby sky

8.2 Observations and Data Reduction

We made two-pointing observations of W 28 with the XIS as a part of the recombining plasma survey project; one covers the central bright region while the other covers the eastern shell. The local background was obtained from the Suzaku archive near W 28. The locations of the two fields and the observation log are respectively shown in figure 8.1 and in table 8.1.

The XIS observation was made with the normal clocking mode. The software package

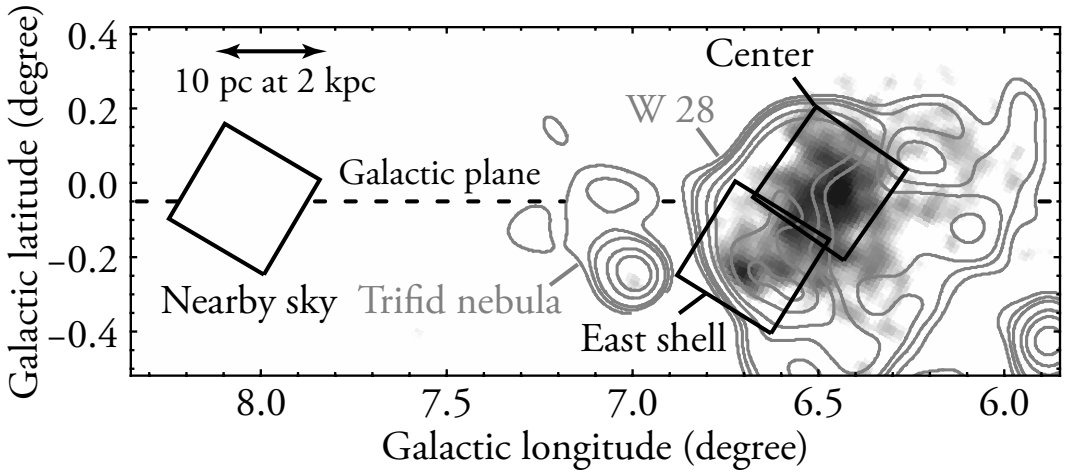

Fig. 8.1.—: Wide-field X-ray image retrieved from the ROSAT All Sky Survey in grayscale (Snowden et al. 1995). Overlaid contours are the radio continuum map at 1.4 GHz by the Very Large Array (Dubner et al. 2000). The XIS FOVs are shown with the solid squares.

HEASoft version 6.11, and the pipeline processing version 2.4 were used for the data reduction. To restore radiation-induced degradation of the energy gain and resolution, the SCI technique (Bautz et al. 2004) was applied with the makepi files version 20110621 provided by the XIS team (Uchiyama et al. 2009). Then the systematic uncertainty in the energy scale is $\lesssim 10$ eV at 5.9 keV. We removed hot and flickering pixels, and events during the South Atlantic Anomaly passages and Earth night-time and day-time elevation angles below 5° and 20°, respectively.

8.3 Analysis and Results

8.3.1 Background Estimation

Figure 8.2 shows the X-ray images of the W 28 center and the nearby-sky fields. The NXB generated by `xisnxbgen` (Tawa et al. 2008) was subtracted, and then the vignetting and exposure corrections were made.

We can see excess emission from W 28 in the soft X-ray band, but no excess in the hard band (figure 8.2). We extracted the source and background spectra from the solid and dashed circles in figure 8.2, respectively. The results are shown in figure 8.3, where the effective area of the background is normalized to that of the source region.

Compared with the background, the source spectrum shows obvious excess below ~ 5 keV

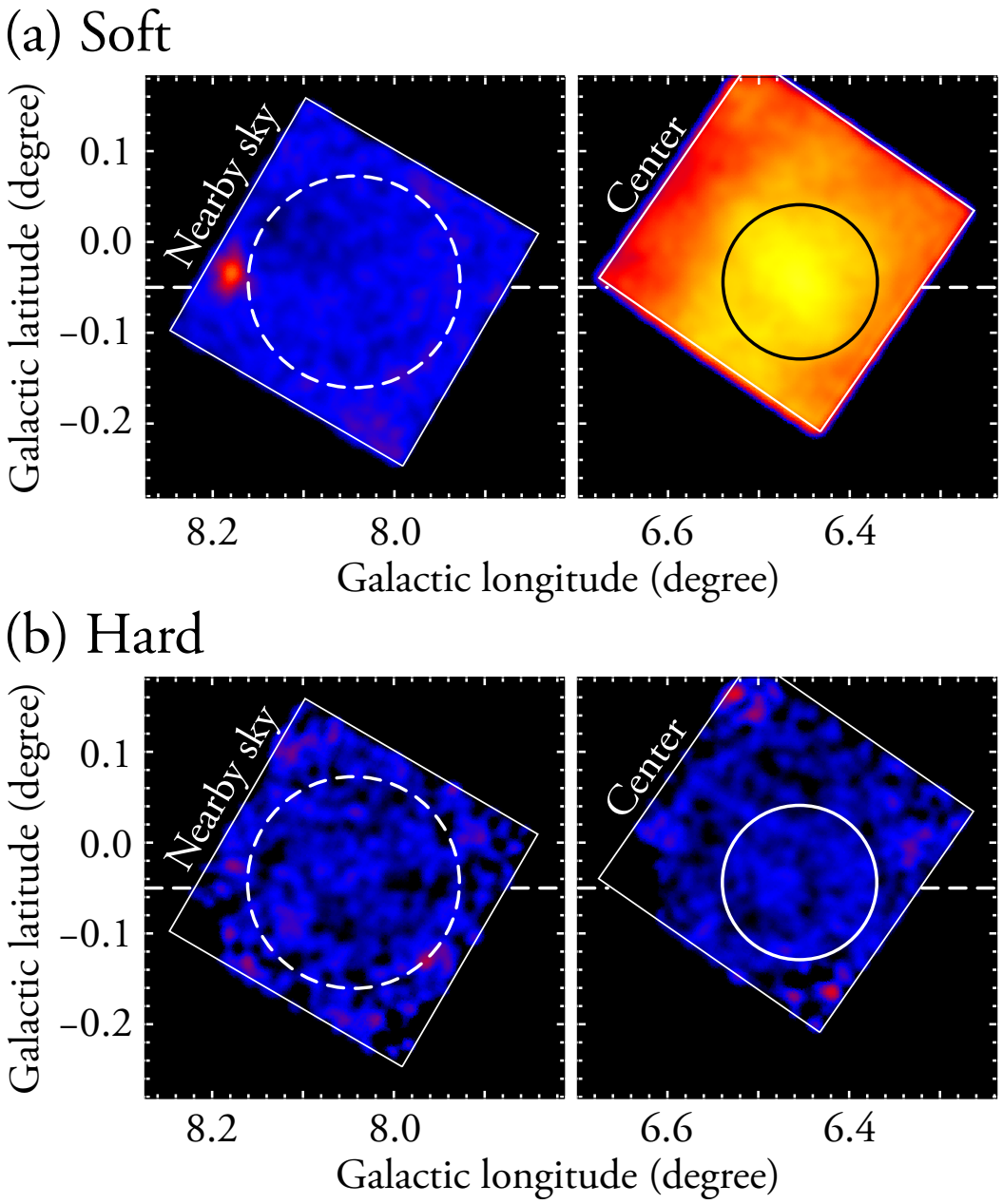

Fig. 8.2.—: Band-limited images with the XIS: (a) soft X-rays in 0.5–5.0 keV and (b) hard X-rays in 5.0–8.0 keV. The data with the three CCDs were merged. The NXB was subtracted and then the exposure and the vignetting were corrected. The source and background extraction regions are shown in the solid and dashed circles, respectively.

but no excess in the hard X-ray band $\gtrsim 5$ keV (figure 8.3), consistent with the images. This result is, however, inconsistent with the previous ASCA observations, which claimed the detection of

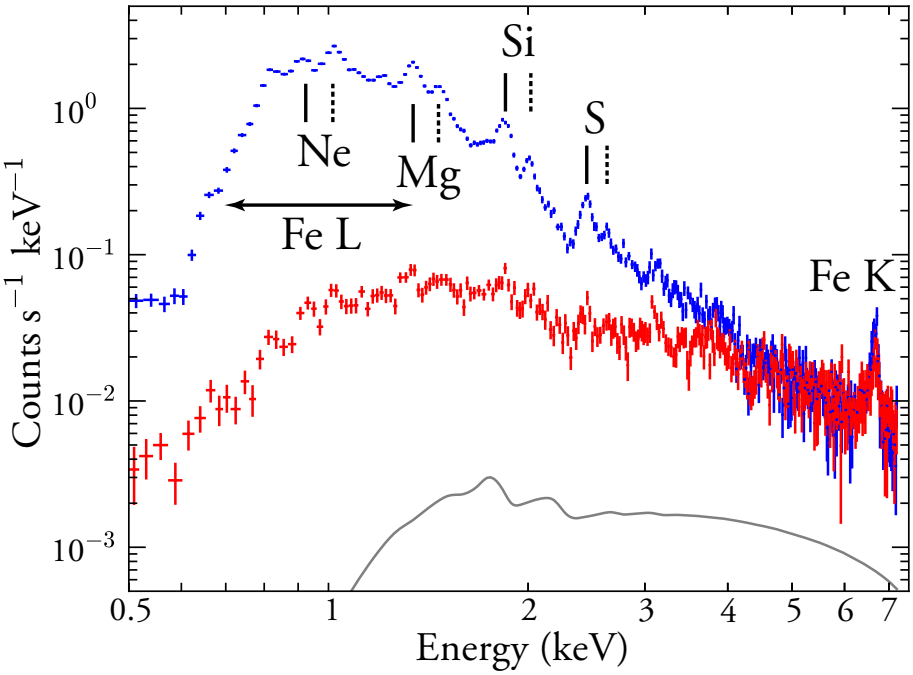

Fig. 8.3.—: Comparison of the source (blue) and the normalized background (red) spectra. For visibility, only merged spectra of FI (XIS 0 and XIS 3) are displayed. The solid and dashed black lines show the center energies of Kα lines from He-like and H-like ions, respectively. The gray line indicates the CXB spectrum.

hard X-ray emission up to ~ 7 keV with the Fe Kα line (Rho & Borkowski 2002).

One problem is position-to-position fluctuations of the CXB. We therefore estimated the CXB flux assuming the photon index, the average surface brightness, and the Galactic absorption to be 1.412, 6.38×10^{-8} erg cm^{-2} s^{-1} sr^{-1} (Kushino et al. 2002), and 1.4×10^{22} H cm^{-2} (Dickey & Lockman 1990), respectively. Then the expected CXB level (the grey curve in figure 8.3) is only about 5% of the total background flux. Thus the error due to the CXB fluctuation can be neglected.

The major source of the background is the GDXE because W 28 is located near the Galactic plane and the GC. In fact, the Fe Kα line at 6.7 keV seen in figure 8.3 is due to the GDXE. Since the surface brightness of the GDXE quickly decreases with increasing distance from the Galactic plane with the scale height of $\lesssim 1^\circ$ (Uchiyama 2010[1]), we selected the background region from the same Galactic latitude (figure 8.2 left) of W 28 (figure 8.2 right). The GDXE uncertainty is, therefore, due to the longitude distribution along the plane. The flux of the GDXE decreases as the distance from the GC increases with the scale length of $\sim 30^\circ$ (Uchiyama 2010). Then

[1]Available at http://repository.tksc.jaxa.jp/pl/dr/IS8000028000/en

the GDXE on the background region is estimated to be about 5% smaller than that on W 28. Still we found no excess from W 28 above the background in the hard X-ray band, and hence no hard X-ray emission above 5 keV for W 28 is very conservative conclusion.

8.3.2 Spectrum of Center

We subtracted the background spectrum (the red data in figure 8.3) from the source spectrum (the blue data in figure 8.3). The result is shown in figure 8.4. We can see many K-shell emission lines from highly ionized Ne, Mg, Si, and S as well as L-shell emission lines from Fe. We therefore examined several optically thin thermal plasma models. In the spectral analysis, we used the SPEX (Kaastra et al. 1996) software version 2.02.02. The redistribution matrix and the auxiliary response functions were generated by `xisrmfgen` and `xissimarfgen` (Ishisaki et al. 2007), respectively, with the latest rmfparam files version 20110708. The abundances for the absorption of ISM (Morrison & McCammon 1983) were assumed to be one solar (Anders & Grevesse 1989), using the Absm model in SPEX. The abundances for Ne, Mg, Si, S, and Fe in the thermal plasma were free parameters, while those of O, Ar and Ca, and Ni were assumed to be the same as those of Ne, S, and Fe, respectively. The other elements, including C and N were fixed to one solar.

CIE Plasmas

We tried a single-temperature optically thin thermal plasma model in CIE (the Cie model in SPEX). The result is shown in figure 8.4a. Although we fit simultaneously for the FI and BI spectra, we show only the best-fit FI spectrum for simplicity. As is seen in figure 8.4a, this model obviously failed to reproduce the spectrum with χ^2/d.o.f. of 2160/641. We therefore examined a two-temperature CIE model (figure 8.4b), with coupled abundances for each element between the two CIE components. This model also failed to reproduce the spectrum with χ^2/d.o.f. of 1753/639. The best-fit parameters for these CIE models are given in table 8.2. In addition to the 0.77-keV plasma, W 28 requires 0.24-keV plasma instead of 1.8-keV plasma of the ASCA results (Rho & Borkowski 2002). The authors proposed that W 28 is a peculiar MM SNR because of the presence of the high-temperature plasma of 1.8 keV. Our results of the 0.24+0.77-keV temperature plasma revised the interpretation of W 28 to be a typical MM SNR (0.4–0.9-keV temperature; Rho & Petre 1998). This revised picture comes from the absence of the high-energy photons above $\sim$5 keV in the Suzaku spectrum, which would be due to proper background subtraction (§ 8.3.1). To improve the value of χ^2/d.o.f., we added further CIE components, but found no significant improvement. The most remarkable residuals in any CIE model are line-like excess at the Si Lymanα energy (2.0 keV) and bump-like structures at 2.4–5.0 keV.

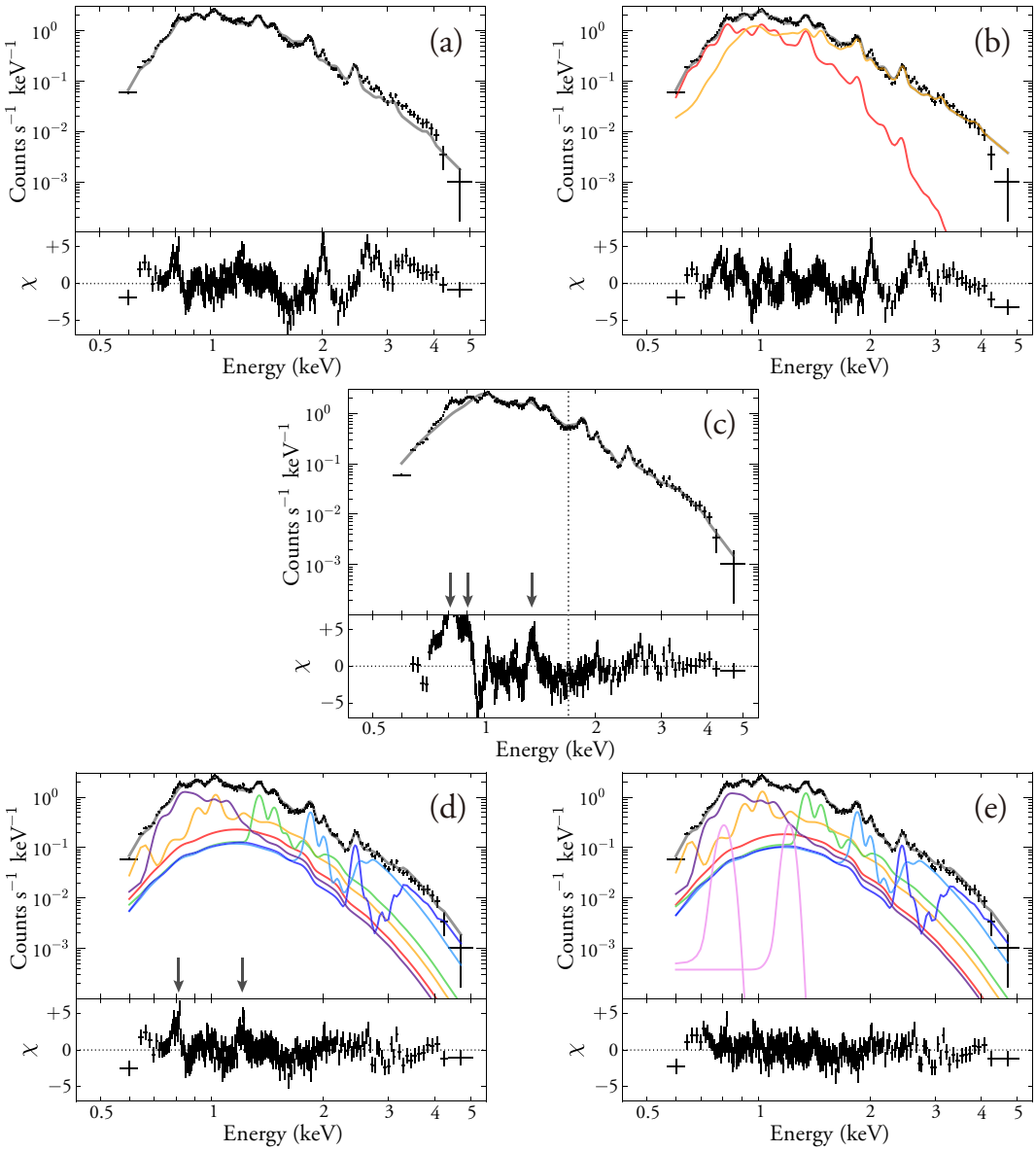

Fig. 8.4.—: The background-subtracted spectrum (the black crosses) with the best-fit models. Thick gray curves are the total emission, while thin colored curves are each component (C and N in red; O and Ne in orange; Mg in green; Si in light blue; S, Ar, and Ca in dark blue; Fe and Ni in purple). For visibility, only data and models for merged FI are displayed. Each panel shows result for different model: (a) single-temperature CIE, (b) two-temperature CIE, (c) single-T_z recombining plasma model, (d) multi-T_z recombining plasma model, (e) the same as (d) but artificial Gaussians at 0.8 and 1.2 keV are added (pink). Solid arrows in (c) indicate the Kα line centers of He-like Mg and Ne, and L-shell complex of Fe. Solid arrows in (d) are L-shell transitions of Fe.

Table 8.2—: Best-fit parameters with CIE and single-T_z recombining plasma models.

Parameter	Single-temperature CIE	Two-temperature CIE	Single-T_z recombining plasma
N_H (10^{21} cm^{-2})	$3.90^{+0.06}_{-0.07}$	$6.28^{+0.11}_{-0.12}$	$2.99^{+0.02}_{-0.02}$
VEM_1 (10^{56} cm^{-3})$*$	$21.1^{+0.7}_{-0.5}$	103^{+11}_{-10}	$64.6^{+0.6}_{-0.6}$
VEM_2 (10^{56} cm^{-3})$*$	...	$13.6^{+0.4}_{-0.4}$	...
kT_1 (keV)	$0.62^{+0.01}_{-0.01}$	$0.24^{+0.01}_{-0.01}$	...
kT_2 (keV)	...	$0.77^{+0.01}_{-0.01}$	...
kT_e (keV)	...	...	0.43 (fixed)
kT_z (keV)	...	...	0.95 (fixed)
Abundance (solar)			
... Ne	$0.39^{+0.02}_{-0.02}$	$0.13^{+0.01}_{-0.01}$	≤ 0.01
... Mg	$0.36^{+0.02}_{-0.02}$	$0.41^{+0.02}_{-0.02}$	$0.18^{+0.01}_{-0.01}$
... Si	$0.25^{+0.01}_{-0.01}$	$0.32^{+0.01}_{-0.02}$	$0.20^{+0.01}_{-0.01}$
... S	$0.50^{+0.04}_{-0.03}$	$0.43^{+0.03}_{-0.02}$	$0.26^{+0.01}_{-0.01}$
... Fe	$0.14^{+0.01}_{-0.01}$	$0.23^{+0.01}_{-0.01}$	$0.06^{+0.01}_{-0.01}$
χ^2/d.o.f.	2160/641	1753/639	6914/642

$*$ Volume emission measure, $VEM = \int n_e n_H dV$, where n_e, n_H, and V are the electron and Hydrogen densities, and the emitting volume, respectively. Values at the distance of 2 kpc.

Recombining Plasma Model with Single T_z

The bumps at 2.4–5.0 keV have two rising edges at 2.4 and 3.2 keV, which are most probably due to RRCs of He-like Si and S, respectively (Ohnishi et al. 2011). Together with the strong Si Lymanα residual, the spectrum is due to a recombining plasma, at least for Si and S. We thus tried a recombining plasma model in the RRC band of Si and S (1.7–5.0 keV). Then the residuals found in the 1.7–5 keV band disappear with the best-fit T_z of $0.95^{+0.01}_{-0.08}$ keV and T_e of $0.43^{+0.03}_{-0.01}$ keV. Fixing these best-fit temperatures, we made full energy band fit. The free parameters were abundances of Ne, Mg, Si, S, and Fe, and N_H. The result is, however, unacceptable with χ^2/d.o.f. of 6914/642 (figure 8.4c). As shown by the solid arrows in figure 8.4c, remarkable excess are found at the Kα lines of He-like Mg (1.35 keV) and Ne (0.92 keV) and the Fe L-shell complex at $\sim$0.8 keV.

Multi-T_z Recombining Plasma

The data excess near the Kα lines of He-like Mg and Ne indicates underestimation of the He-like line fluxes compared to the H-like line (see the solid arrows in figure 8.4c). This supports that T_z for Mg is significantly lower than those of Si and S. We therefore introduced a recombining plasma model with different T_z for each element (figure 8.4d). Since no spectral code to directly describe such a plasma is available, we approximated the model with the combination of several single-T_z plasmas whose T_e are coupled among the all plasmas. We grouped the elements into six sub-groups assuming the same abundances in each sub-group (see the caption of figure 8.4). For C and N, we fixed T_z to T_e.

Table 8.3—: Best-fit parameters with a multi-T_z recombining plasma model.

Parameter	A	B
N_H (10^{21} cm^{-2})	$4.65^{+0.07}_{-0.10}$	$4.7^{+0.09}_{-0.07}$
VEM (10^{56} cm^{-3})$*$	$60.7^{+8.2}_{-6.1}$	$47.1^{+4.2}_{-3.6}$
kT_e (keV)	$0.39^{+0.02}_{-0.02}$	$0.40^{+0.01}_{-0.02}$
kT_z (keV)		
... Ne	$0.48^{+0.04}_{-0.03}$	$0.46^{+0.03}_{-0.03}$
... Mg	$0.66^{+0.05}_{-0.04}$	$0.66^{+0.04}_{-0.04}$
... Si	$1.01^{+0.06}_{-0.05}$	$1.01^{+0.05}_{-0.05}$
... S	$0.95^{+0.10}_{-0.08}$	$0.96^{+0.08}_{-0.06}$
... Fe	$0.58^{+0.04}_{-0.03}$	$0.58^{+0.03}_{-0.03}$
Abundance (solar)		
... Ne	$0.16^{+0.01}_{-0.01}$	$0.23^{+0.01}_{-0.01}$
... Mg	$0.32^{+0.02}_{-0.02}$	$0.44^{+0.02}_{-0.02}$
... Si	$0.26^{+0.02}_{-0.02}$	$0.34^{+0.02}_{-0.02}$
... S	$0.33^{+0.07}_{-0.07}$	$0.40^{+0.05}_{-0.05}$
... Fe	$0.10^{+0.01}_{-0.01}$	$0.11^{+0.01}_{-0.01}$
χ^2/d.o.f.	1268/636	893/634

$*$ Values at the distance of 2 kpc.

As shown in figure 8.4d, this model (model A) well reproduced the overall structure of the observed spectrum. Still some residuals remain at ~ 0.8 and ~ 1.2 keV (see the solid arrows in figure 8.4d). These features are known to originate from incomplete atomic data in the current spectral code. The former comes from the uncertain intensity ratio of the Fe L-shell transitions of 3s$\rightarrow$2p and 3d$\rightarrow$2p (Gu et al. 2007 and reference therein). The present code may underestimate the 0.8 keV line flux. The latter is due to the lack of a number of the Fe L-

shell lines by the transitions from highly excited states of $n \geq 5$ (Brickhouse et al. 2000). Thus, we artificially added two Gaussians at 0.8 keV and 1.2 keV (figure 8.4e). Then the fit largely improved (model B; χ^2/d.o.f. = 893/634). The best-fit parameters for Model A and B are listed in table 8.3. We see that the best-fit T_z are essentially the same between model A and B. The best-fit T_z values are different among elements with higher temperature than T_e (table 8.3).

8.3.3 Spatially Resolved Spectra

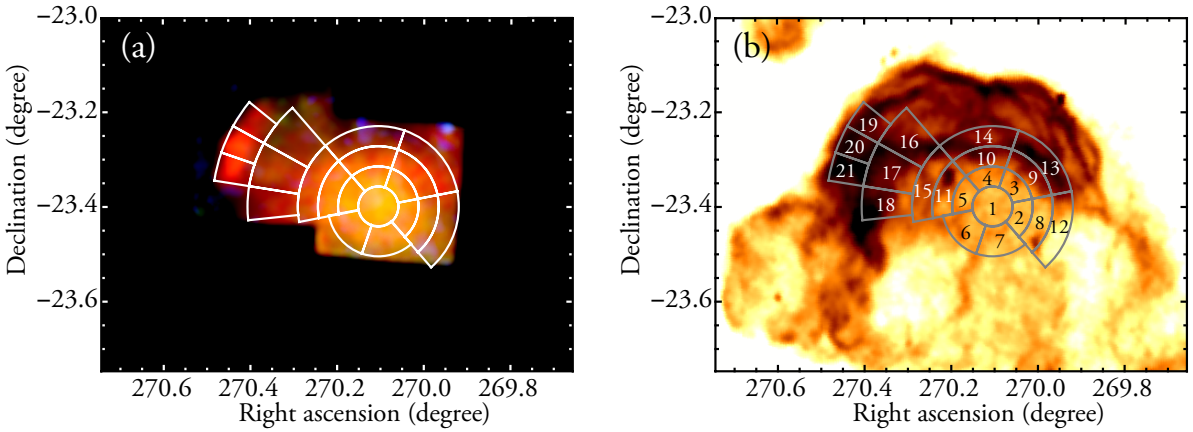

Fig. 8.5.—: The divided sectors for the spatially resolved spectral analysis (white regions) overlaid on (a) the X-ray images and (b) the radio 90-cm continuum image (Brogan et al. 2006) of W 28. The red, green, and blue colors in (a) show the soft (0.5–2.0 keV), medium (2.0–5.0 keV), and hard (5.0–8.0 keV) X-rays, respectively. The labels in the panel (b) indicate the sector numbers.

In order to investigate the spatial structure of the recombining plasma, we performed spatially resolved spectral analysis. For this purpose, we coaxially divided the two FOVs into 21 sectors as shown by white regions in figure 8.5. We utilized the same background spectrum as used for center (§ 8.3.1) but with different normalization of effective area for each sector. The systematic uncertainty of the background emission mainly comes from the spatial variation of surface brightness of the GDXE (§ 8.3.1). The uncertainty is estimated to be within $\sim \pm 5\%$. The background-subtracted spectra are given in appendix (figure B.1).

In this analysis, we focused on the ionization temperatures of Si and S since the RRCs from these elements are most clearly detected in the spectra of the central region. Hence, we

restricted the fitting energy bands to be 1.7–5.0 keV and used the single-T_z recombining plasma model. The free parameters were volume emission measures (VEM), electron and ionization temperatures (respectively T_e and T_z), and the abundances of Si and S (respectively Z_{Si} and Z_S). The abundances of Ar and Ca were coupled with that of S and those for remaining elements were fixed to the solar values. The hydrogen column densities of interstellar absorption were fixed to the best-fit value for the center region (N_H =4.7×10^{21} cm^{-2}). The best-fit parameters of T_e and T_z, and the X-ray surface brightnesses SB are shown in table 8.4.

Table 8.4—: The best-fit parameters with recombining plasma models for the divided sectors.

Sector	kT_e (keV)	kT_z (keV)	$SB*$	χ^2/d.o.f
1	$0.50^{+0.06}_{-0.05}$	$1.02^{+0.09}_{-0.09}$	$1.22^{+0.11}_{-0.10}$	251/184
2	$0.40^{+0.09}_{-0.06}$	$0.93^{+0.15}_{-0.14}$	$0.94^{+0.13}_{-0.15}$	109/79
3	$0.33^{+0.04}_{-0.04}$	$0.83^{+0.10}_{-0.09}$	$1.00^{+0.09}_{-0.08}$	99/91
4	$0.35^{+0.04}_{-0.05}$	$0.84^{+0.13}_{-0.07}$	$1.00^{+0.11}_{-0.08}$	130/90
5	$0.51^{+0.10}_{-0.07}$	$0.98^{+0.15}_{-0.16}$	$1.02^{+0.15}_{-0.15}$	107/137
6	$0.31^{+0.05}_{-0.04}$	$0.90^{+0.16}_{-0.12}$	$0.83^{+0.06}_{-0.06}$	174/158
7	$0.54^{+0.12}_{-0.16}$	$1.04^{+0.37}_{-0.18}$	$0.86^{+0.23}_{-0.14}$	119/98
8	$0.63^{+0.13}_{-0.17}$	$0.95^{+0.33}_{-0.20}$	$0.72^{+0.19}_{-0.12}$	97/78
9	$0.26^{+0.04}_{-0.11}$	$0.66^{+0.78}_{-0.11}$	$0.58^{+0.08}_{-0.12}$	150/131
10	$0.28^{+0.05}_{-0.04}$	$0.81^{+0.19}_{-0.13}$	$0.58^{+0.06}_{-0.05}$	125/124
11	$0.41^{+0.10}_{-0.08}$	$0.90^{+0.20}_{-0.15}$	$0.87^{+0.16}_{-0.15}$	108/88
12	$0.31^{+0.06}_{-0.06}$	$0.82^{+0.23}_{-0.14}$	$0.52^{+0.06}_{-0.06}$	63/65
13	$0.28^{+0.05}_{-0.04}$	$0.54^{+0.08}_{-0.08}$	$0.34^{+0.09}_{-0.08}$	83/110
14	$0.26^{+0.06}_{-0.05}$	$0.74^{+0.47}_{-0.14}$	$0.28^{+0.13}_{-0.05}$	100/91
15	$0.29^{+0.04}_{-0.05}$	$0.72^{+0.17}_{-0.09}$	$0.49^{+0.06}_{-0.06}$	224/191
16	$0.26^{+0.03}_{-0.11}$	$0.64^{+0.21}_{-0.07}$	$0.32^{+0.04}_{-0.05}$	210/194
17	$0.28^{+0.03}_{-0.02}$	$0.61^{+0.14}_{-0.05}$	$0.37^{+0.06}_{-0.05}$	196/165
18	$0.29^{+0.04}_{-0.03}$	$0.49^{+0.05}_{-0.06}$	$0.26^{+0.09}_{-0.06}$	96/112
19	$0.26^{+0.03}_{-0.03}$	$0.48^{+0.06}_{-0.05}$	$0.27^{+0.09}_{-0.06}$	112/118
20	$0.27^{+0.02}_{-0.02}$	$0.46^{+0.04}_{-0.04}$	$0.44^{+0.08}_{-0.08}$	150/153
21	$0.27^{+0.03}_{-0.02}$	$0.41^{+0.07}_{-0.03}$	$0.33^{+0.02}_{-0.07}$	98/121

$*$ The average surface brightness in the 1.7–5.0 keV band in units of 10^{-5} photons s^{-1} cm^{-2} arcmin^{-2}.

8.4 Nature of W 28

We have found centrally peaked thermal X-ray emission filling inside the radio non-thermal shell. The X-ray surface brightness (SB) distribution is given in figure 8.6, together with the radio emission. The radial distributions are also given in figure 8.7. The X-ray profile shows clear central peak. Assuming spherical distribution with uniform density, the SB profile is given by a cosine curve as is shown with the green solid curve in figure 8.7. The observed SB (blue crosses) is more concentrated toward the center compared to the spherical plasma distribution. The centrally peaked X-rays are often observed around the central neutron star as a PWN. The X-rays from PWN is non-thermal origin. We have found that all the spatially resolved spectra are free from non-thermal components, no particular excess of non-thermal hard X-rays is found near the center region also. Thus, we confirmed that W 28 is one of the typical MM SNRs.

We have found that the X-ray spectrum is described by a recombining plasma. This is the fourth discovery of recombining plasma in MM SNRs, after IC 443, W 49B, and G 359.1–0.5 (Yamaguchi et al. 2009; Ozawa et al. 2009b; Ohnishi et al. 2011). Like these MM SNRs, W 28 is associated with OH (1720 MHz) maser sources indicating shock-excited molecular clouds and GeV/TeV γ-ray sources.

Since the previous studies on the three MM SNRs were limited in the narrow band spectroscopy, only one or two elements can be available in measurements of T_z; Si and S were available for IC 443 and G 359.1–0.5 and Fe was available for W 49B. We have performed broad-band spectral analysis of W 28 and found that the spectrum composes of multi-T_z recombining plasma. Thus, W 28 is the first established MM SNR having a multi-ionization temperature recombining plasma.

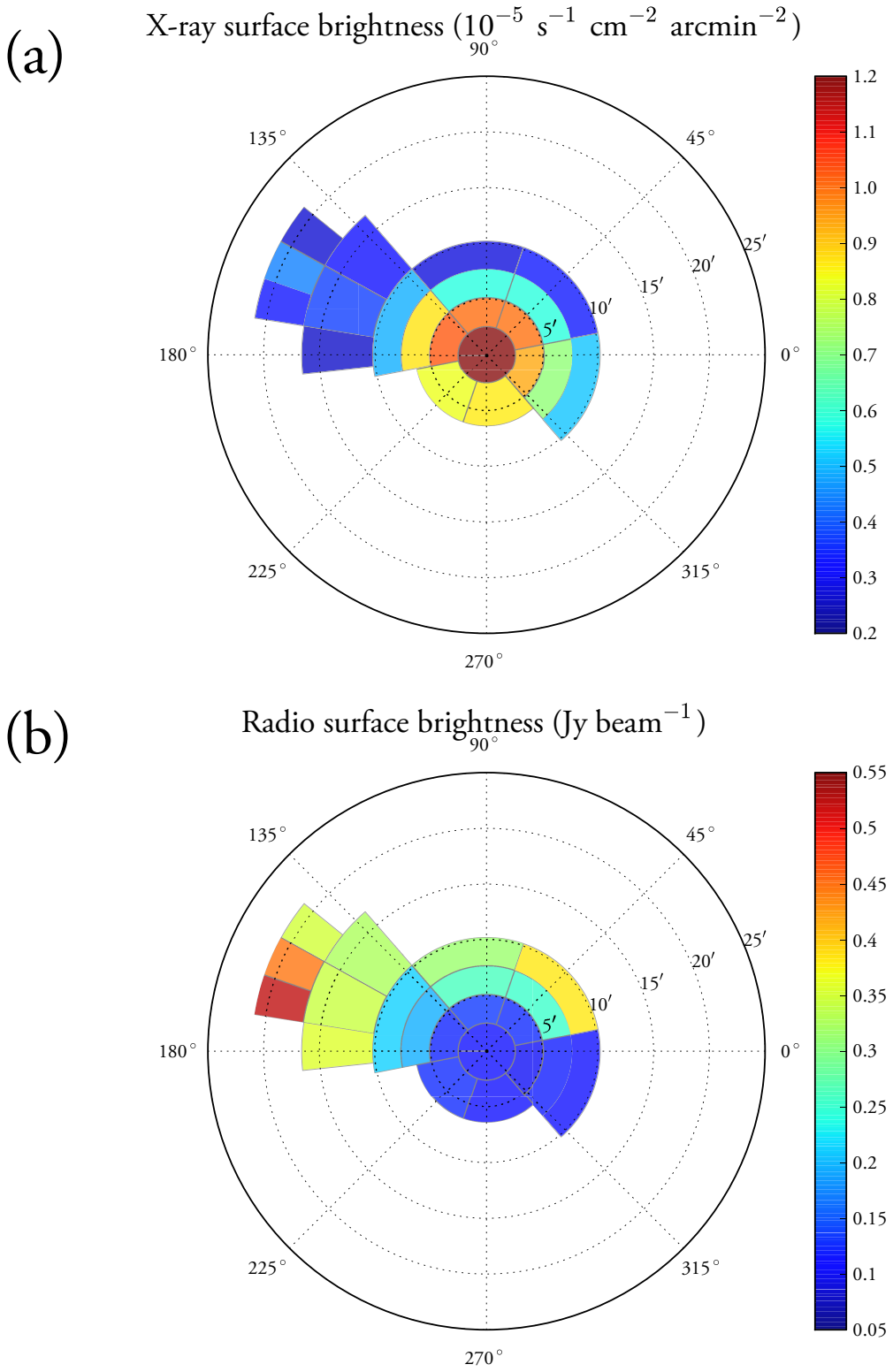

Fig. 8.6.—: The Surface brightness maps of W 28: (a) the Suzaku X-ray in 1.7–5.0 keV and (b) the VLA radio continuum at 90 cm.

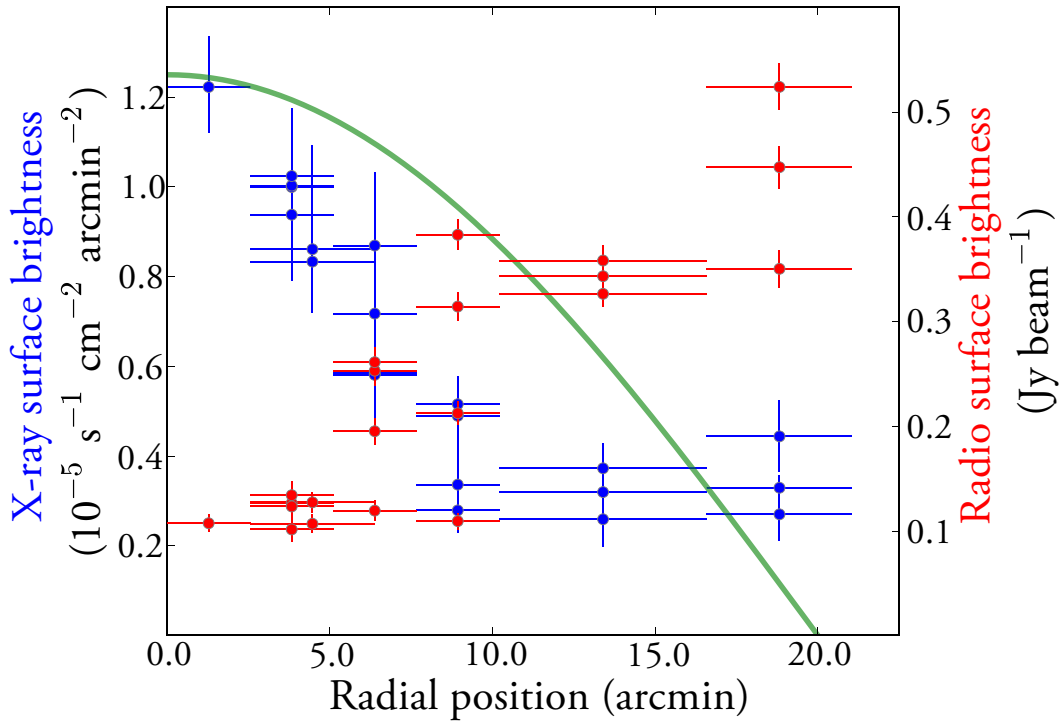

Fig. 8.7.—: The radial profiles of the X-ray (blue) and radio (red) surface brightnesses. Green solid curve shows the expected X-ray profile for the spherical plasma distribution with uniform density.

Chapter 9

Discussion

Contents

We have studied the three non-standard SNRs in the GC region. All of them have different and distinct structures, which can not be produced in the standard evolution. The variety in the observed structures and environments may indicate that the three non-standard SNRs were produced by different "missing branches" in the SNR evolution.

One of them, G 1.2–0.0, has peculiar structure like a blow-out from the Sgr D H II region. The SN explosion and following evolution would be occurred in or around the H II region and its natal molecular cloud. Such a highly non-uniform environment may produce the blow-out structure. Another SNR, G 357.7–0.1, is produced by the bipolar outflows. A possible explanation for the structure is that the SNR has the rapidly rotating very massive progenitor, and it has exploded as a hypernova (possibly type Ib/Ic explosion). The two SNRs, however, have the thermal plasmas in nearly CIE, and hence we can not quantitatively discuss the origins any further based on the thermal structures.

The other one, the MM SNR W 28, exhibits a recombining plasma (RP). This result confirms that RPs are only found in MM SNRs. Furthermore, we provide the most precise and detailed spatial and spectral structures of the RP. This leads us to a quantitative discussion on a possible origin of RPs in the MM SNRs for the first time. Since the RPs are neither predicted nor observed in the standard SNRs, the origin of RP would become a missing branch, which should be involved in a new scenario of the SNR evolution. The missing branch may also be physically related to the formation of MM SNRs.

9.1 Possible Scenarios

The standard scenario of SNRs predicts either ionizing plasma (IP) or CIE plasma. If some additional process such that the electron temperature is preferentially decrease (case 1), or ionization is selectively enhanced (case 2), then RP would be realized.

As the first case (case 1), we propose two scenarios. One is thermal conduction scenario. If the normal IP or CIE plasma encounters to cold molecular clouds (MC), the electron energy will be transferred to the MC by thermal conduction, and hence the electron temperature drops rapidly. Since the recombination timescale of ionized atoms is longer than the conduction time scale, the ionization temperature cannot follow the decrease of the electron temperature, and hence RP would be realized. This process, therefore, makes the electron temperature lower in the region of the shock-cloud interaction than the other regions. In fact, this scenario is stimulated by the observed correlation of MM SNRs and OH (1720 MHz) masers (e.g. Yusef-Zadeh et al. 2003a).

The other is rarefaction scenario proposed by Itoh & Masai (1989). If the SN explodes in a dense CSM around the massive progenitor, the ejecta and CSM are shock-heated quickly to

IP or CIE, because the ionization timescale is short even in a dense medium. Soon after the shock wave breaks the CSM region out to lower density ISM. Then the electron temperature cools down by the adiabatic expansion.

The second case (case 2) is the extra-ionization scenarios. One is photo-ionization scenario proposed by Kawasaki et al. (2002). If high-energy radiation fields are realized in addition to normal shock-heating process, effective photo-ionization rises the ionization temperature, while the electron temperature is less affected because the heating by Compton scattering is less efficient. As the results the plasma becomes RP.

The other is the extra-ionization by supra-thermal electrons with the energy range of 10–100 keV. These electrons have large ionization cross sections than the thermal electrons, and hence the apparent ionization temperature becomes significantly higher than the case of pure thermal electrons. Since the efficient ionization is possible by a small fraction of supra-thermal electrons in the large population of thermal electrons (about 5% in the number density; Masai et al. 2002), these supra-thermal electrons do not appear in the continuum X-ray spectra, and hence apparent RP would appear.

9.2 Spatial Structure of RP

We give the maps of $T_{\rm e}$ and $T_{\rm z}$ in figure 9.1 based on the best-fit parameters obtained in § 8.3.3. As shown in the figure, both $T_{\rm e}$ and $T_{\rm z}$ have higher values near the center of the SNR and decrease with increasing distance from the center. The ratio $T_{\rm z}/T_{\rm e}$, which is the indicator of over-ionization degree, also shows a peak near the center. These spatial structures indicate that the extra-ionizing source to make RP should be located near the center.

In the thermal conduction model, $T_{\rm e}$ must be lower near the interacting cloud and become higher with the increasing distance from the cloud. To examine this, we use the ^{12}CO J =1–0 (0–10 km s^{-1}) image by NANTEN (Aharonian et al. 2008). The MCs are concentrated to the eastern part of the remnant as shown in figure 9.2a. Thus the prediction from the thermal conduction model gives spatial trend inconsistent with the observed trend of $T_{\rm e}$ (see figures 9.1a and 9.2a). For more quantitative comparison, we plot the electron temperature as a function of the CO J =1–0 line brightness in figure 9.2b. We find that the center region (sector 1) has higher electron temperature of $\sim$0.5 keV compared to the regions of intense molecular emission (sectors 10, 18, and 21) with $T_{\rm e}$ of $\sim$0.3 keV. Furthermore, the other regions have all the same $T_{\rm e}$ of $\sim$0.3 keV. Thus, we conclude that no clear spatial correlation exists between the electron temperatures and the shocked MCs (figure 9.2b). This fact rules out the possibility of the thermal conduction scenario for the origin of RP.

For the supra-thermal electron scenario, we can judge from the spatial correlation of $T_{\rm z}$

and TeV γ-ray flux. These high-energy radiations indicate the existence of cosmic ray particles, where supra-thermal electrons would be injectors of this particle accelerator. Accordingly, $T_{\rm z}$ would be higher near the γ-ray sources. In order to check whether the centrally peaked $T_{\rm z}$ distribution correlates with the γ-ray flux, we use the TeV γ-ray emission map by H.E.S.S. (Aharonian et al. 2008; shown in figure 9.2c). The position of GeV γ-ray emission subsequently detected by Fermi (Abdo et al. 2010b) is also given by the red circle. As shown in figure 9.2c, the GeV/TeV γ-ray emissions are enhanced at the eastern edge of the radio shell and that of the X-ray emission. On the other hand, $T_{\rm z}$ monotonically decreases from the center to the east-end (figure 9.1b). Thus the supra-thermal electron scenario is unlikely. The $T_{\rm z}$ distribution as a function of the distance from the peak of TeV γ-rays is given in figure 9.2d. We see rather negative correlation. From all together, we can safely reject the supra-thermal electron origin for the RP.

The photo-ionization model can be consistent with the observed spatial distribution of RP, if the photo-ionizing source is located at the SNR center. The properties of photo-ionized plasmas are determined by one parameter, $\xi = L/(nR^2)$, where L is the luminosity in units of 10^{37} erg s^{-1}, n (cm^{-3}) and R (cm) are the density, and the radius of the photo-ionized plasma, respectively (Tarter et al. 1969). Kallman & McCray (1982) simulated the physical properties of photo-ionized plasmas with various densities. Using the results of the low density (optically thin) model, we estimate the required condition for the ionizing source. For example, the required radiation field to ionize S atoms to He-like state or higher can be given as $\xi > 10^{2.5}$ (see figure 1 in Kallman & McCray 1982). For the radius of R =10 pc and n =1 cm^{-3}, typical values for SNRs, the required luminosity is $>3\times10^{41}$ erg s^{-1}. Such a luminous hard X-ray source was not found in the Suzaku data (see figure 8.5a). It might be very luminous transient. One good candidate is the X-ray afterglows of the γ-ray bursts at the SN explosion. In this case, the spatial structure of $T_{\rm z}$ would be consistent with the observation; the highest temperature at the center and gradual decrease as increasing distance (figure 9.1b).

The rarefaction scenario is also consistent with the spatial distribution of $T_{\rm e}$ and $T_{\rm z}$. Furthermore this scenario may give consistent picture of $T_{\rm e}$ and the X-ray surface brightness (SB) distributions. The SB is proportional to the integration of the density square along the line of sight, and hence it can be an indicator of the density distribution. The $T_{\rm e}$ would be nearly uniform in the CSM due to high density. After the shock break-out to the ISM, the $T_{\rm e}$ drops by the rarefaction. Since the process is adiabatic, the electron temperature is determined by the change of the density. We plot the SB distribution in figure 8.7. The green solid line is the estimated curve for the uniform and spherical plasma. The observed SB (blue crosses) indicates that the density distribution is more concentrated toward the center than the spherical case. This result may indicate that the outer region have experienced larger rarefaction and hence the electron temperature is lower than those of the center. Thus the observed correlation between SB and $T_{\rm e}$ is in good agreement with the rarefaction scenario.

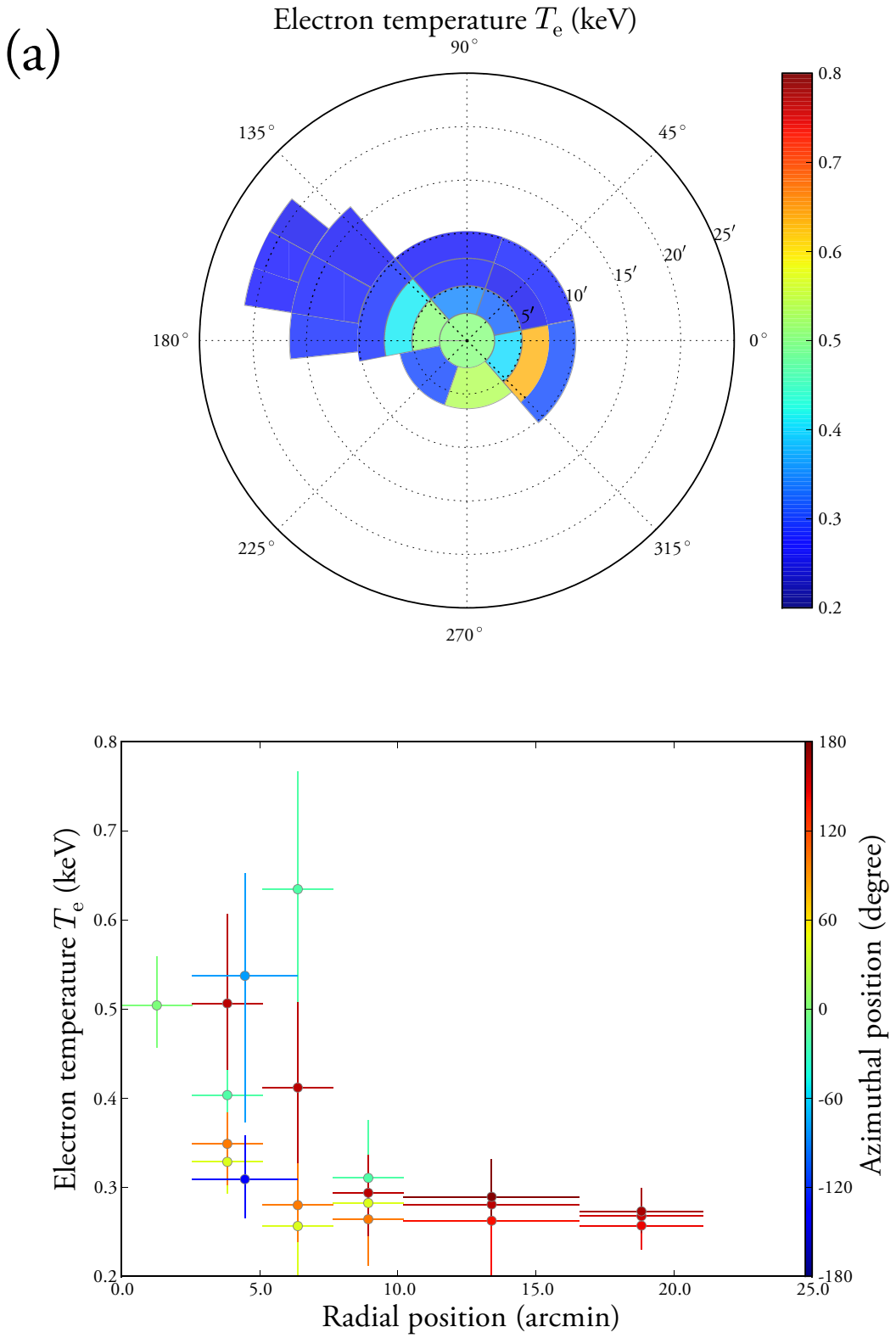

Fig. 9.1.—: The spatial variation of (a) the electron temperature and (b) the ionization temperature in W 28. Colormap in upper panels show the best-fit values while crosses in lower panels show the best-fit values and the statistical uncertainties with respect to the radial positions. The color of the crosses indicate the azimuthal positions.

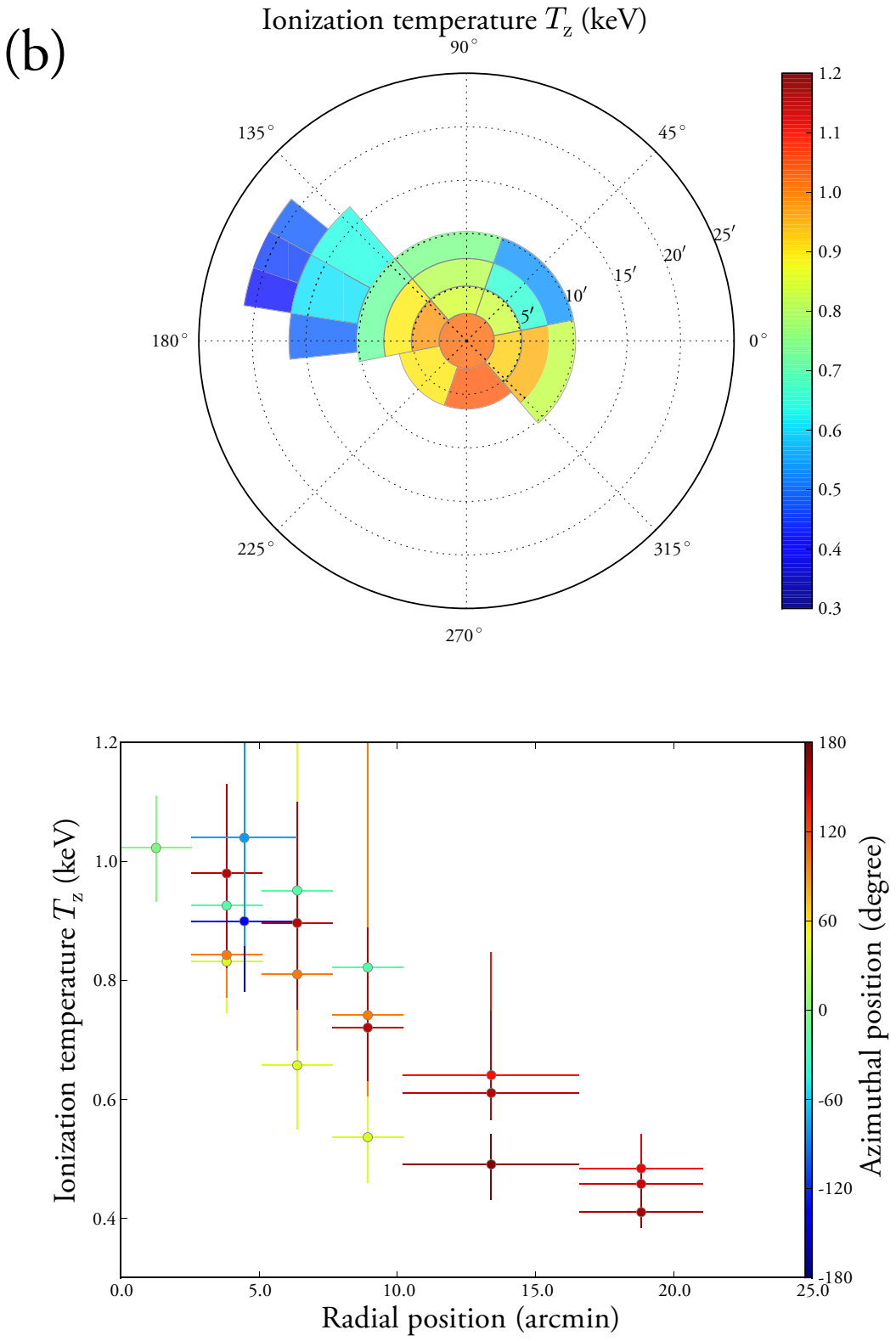

Fig. 9.1.—: *Continued.*

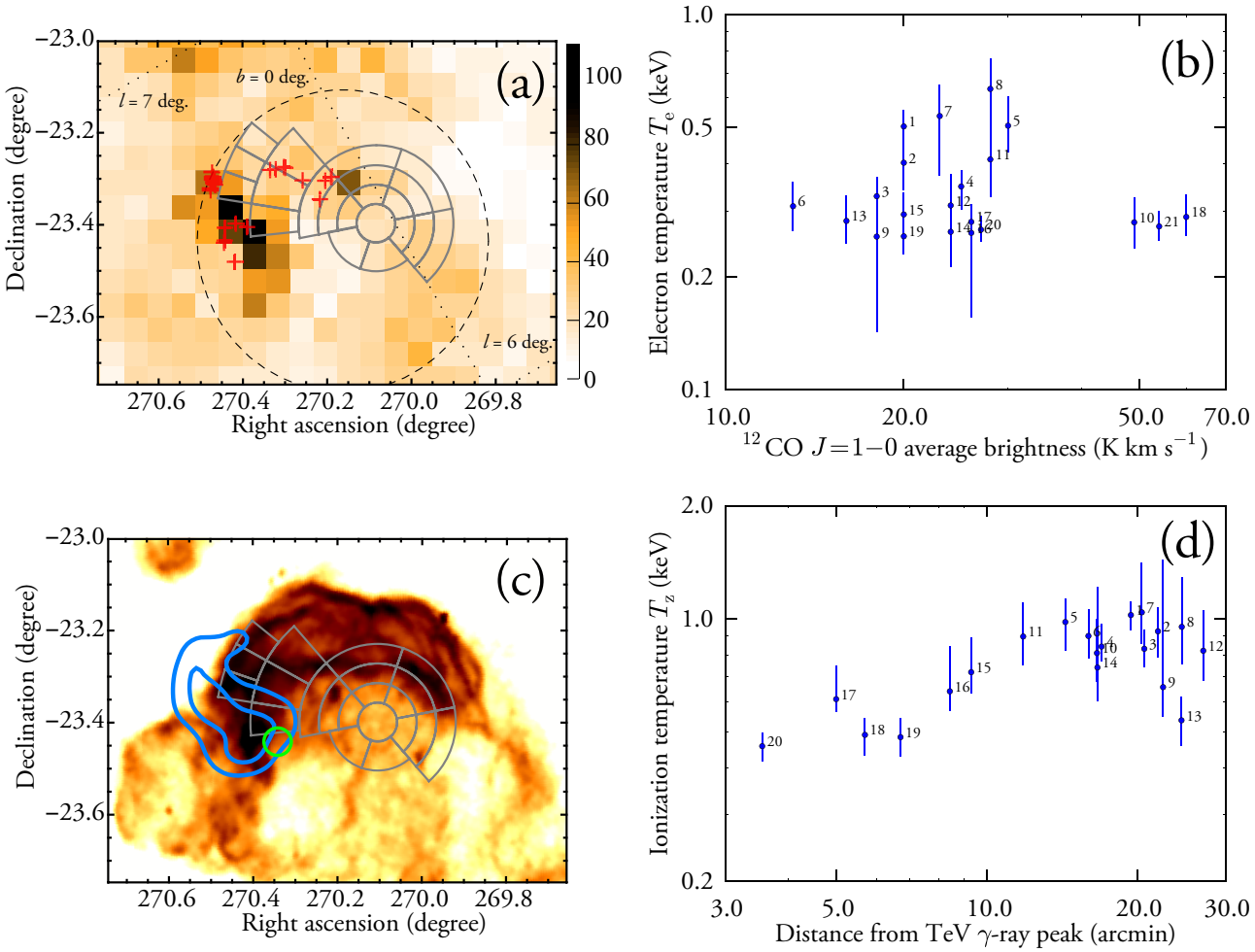

Fig. 9.2.—: The spatial correlations between RP and other structures. (a) The distribution of the interacting molecular clouds. The colormap shows the CO J =1–0 molecular line intensity by NANTEN with linear scale in units of K km s^{-1}, integrated over 0–10 km s^{-1}. The CO map is taken from figure 2 of Aharonian et al. (2008). The red crosses are the positions of the OH (1720 MHz) masers (Claussen et al. 1999). The black dashed circle indicate the rough boundary of the radio shell. (b) A comparison between CO J =1–0 average brightness and T_e. (c) The distribution of the GeV and TeV γ-ray emission overlaid on the radio 90-cm continuum image in the same scale with figure 8.5b. The blue contours are the TeV γ-ray significance map by H.E.S.S. at 4- and 5-σ levels (Aharonian et al. 2008), while the green circle is the 1-σ error region of the GeV γ-ray peak by Fermi (Abdo et al. 2010b). (d) A comparison between the projected distances from TeV γ-ray peak at the northeast of the remnant and T_z. The labels in (b) and (d) indicate the sector numbers (see figure 8.5b).

9.3 Elemental Distribution of T_z

In the previous section, we interpret that both the photo-ionization after a γ-ray burst and the rarefaction scenarios are consistent with the observed spatial distribution of RP. In order to distinguish these two possible scenarios, we discuss the elemental distribution of T_z. The real process of these two scenarios may be composed of two stages; (1) the initial event to make RP and (2) gradual relaxation of the RP toward CIE. Difference of T_z among elements can appear in a relaxation of RP to CIE because the relaxation timescale is different from element to element.

Numerical studies have demonstrated that the relaxation timescale basically shows monotonic increase with atomic number, except for Fe and Ni (e.g., see figure 1 of Smith & Hughes 2010). These two heavy elements have shorter timescales than the other lighter elements at T_z from sub to a few keV, because the L-shell processes are dominant for Fe and Ni, while the K-shell processes are dominant for the others in this temperature range. The observed T_z values appear to satisfy this trend (table 8.3). For more quantitative discussion, we simulate the evolution of T_z in the recombining phase in the next subsection.

9.3.1 Recombination Timescale

We simulate time evolutions of T_z in a RP by using the Neij model in SPEX. The parameters are the initial ionization temperature T_{z0}, the electron temperature T_e, and the recombination time $n_e t_{rec}$, where n_e and t_{rec} are the density of electrons and the elapsed time, respectively. We have tried many sets of (T_{z0}, t_{rec}) for fixed T_e of 0.4 keV following the best-fit value (table 8.3). We obtained similar best-fit T_z distribution from different parameter sets of T_{z0} and t_{rec} (see chapter C). We therefore constrain the parameter set within physically reasonable values.

One plausible case of T_{z0} =3 keV is given in figure 9.3a, which shows the simulated decrease of T_z with time ($n_e t_{rec}$). We find the best-fit recombination time to be $n_e t_{rec} = 10^{11.8}$ s cm^{-3}. The simulated T_z values after $10^{11.8}$ s cm^{-3}, is close to the observation with χ^2/d.o.f. of $\sim 21/4$. We caution that the χ^2/d.o.f. value is just for reference to compare a more complex simulation given in the next subsection, and should not be taken seriously, because the major uncertainty of the observed T_z is not statistic error but systematic one due to incomplete modeling and/or atomic data in the analyses.

This simulation is assumed that in the beginning, almost all of the elements are fully ionized. This condition may be satisfied with the photo-ionization by the strong X-ray afterglows after the γ-ray burst. Typical luminosity of 10^{44-45} erg s^{-1} is bright enough to make fully ionized atoms (Berger et al. 2003). On the other hand, rarefaction scenario may not be the case, because the shock heating in the dense CSM make ionization temperature different from

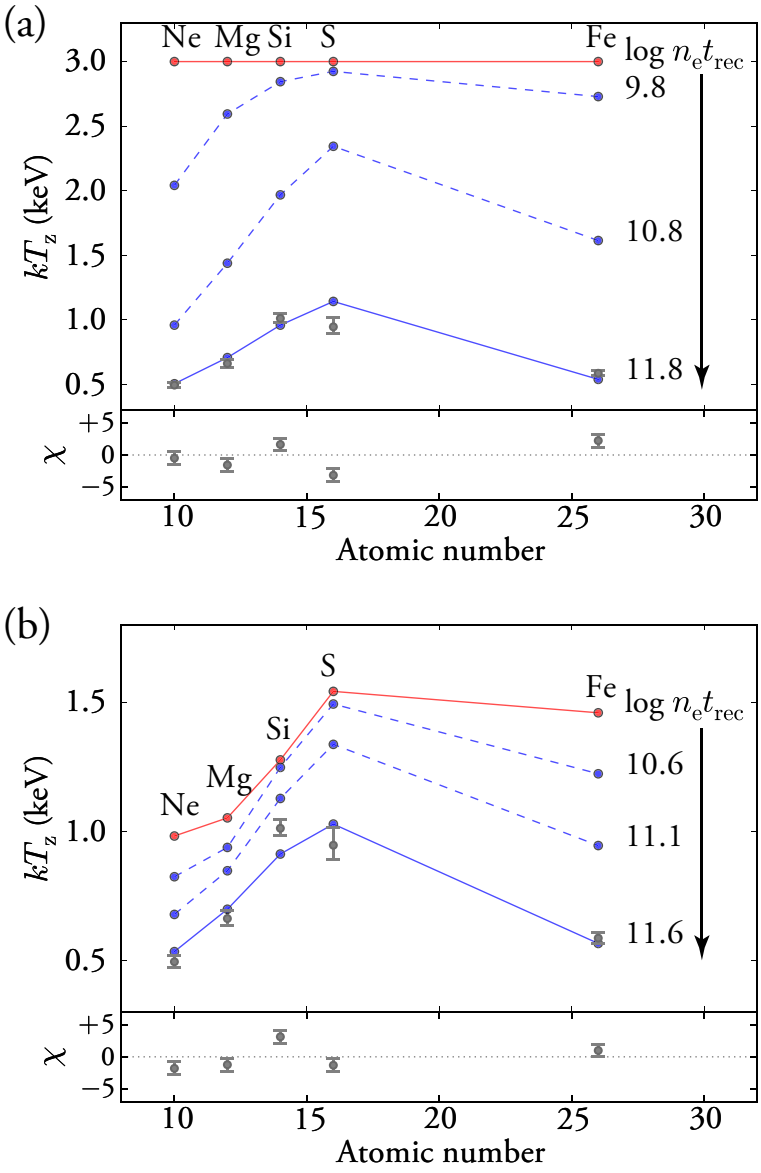

Fig. 9.3.—: Time evolution of T_z in RPs with the initial conditions of (a) $T_{z0} = 3.0$ keV for all elements and (b) T_{z0} realized by an IP with $T'_e = 10$ keV and $n_e t_{ioni} = 10^{11}$ s cm^{-3}. The gray circles with bars show the observed T_z with the 1-σ statistical errors. The direction of evolution as a function of $n_e t_{rec}$ is indicated by the vertical arrows. The solid lines in red and blue respectively show the initial and final states while the dashed blue lines show transitional states.

element to element. Thus the question is whether the initial condition of element-dependent T_z made by initial shock-heating, can give better fit to the observation or not. In the next subsection we move on this issue.

9.3.2 Initial Variation of $T_{\rm z}$

We simulate the time evolution of $T_{\rm z}$ with two steps. In the first step, we simulate the evolution of $T_{\rm z}$ in an IP. This gives the element-dependent $T_{\rm z0}$. Then using this result, we simulate the evolution of recombining process as was done in the previous subsection. The first step is only needed for the rarefaction scenario but not for the photo-ionization after a γ-ray burst. The relevant parameters are the electron temperature during the initial ionizing phase $T'_{\rm e}$, the ionization time $n_{\rm e}t_{\rm ioni}$, and the recombination time $n_{\rm e}t_{\rm rec}$. The electron temperature during the following recombining phase $T_{\rm e}$ is assumed to be 0.4 keV.

In figure 9.3b, we plot decrease of $T_{\rm z}$ during the recombining phase for the case of $T'_{\rm e} = 10$ keV and $n_{\rm e}t_{\rm ioni} = 10^{11.0}$ s cm^{-3}. The best-fit timescale is $n_{\rm e}t_{\rm rec} = 10^{11.6}$ s cm^{-3}, which is similar to the ages of typical SNRs with RP. This combined process gives a better fit to the observed $T_{\rm z}$, than that of the single relaxation process of RP (see subsection 9.3.1) with χ^2/d.o.f. of $\sim 17/4$. Thus we conclude that the rarefaction scenario is better than the photo-ionization scenario to explain the observed elemental variation of $T_{\rm z}$.

9.4 Origin of Recombining Plasma and Missing Branch

From a line of evidence given in the previous sections, we conclude the most plausible scenarios for RP is rarefaction.

Shimizu et al. (2012) extended the previous calculation of Itoh & Masai (1989) to non-symmetric cases and considered anisotropic (disk-like) CSM. In this model, the break-out occurs earlier in the polar direction than in the equatorial direction. Although the most drastic decrease of T_e occurs just after the break-out, the rarefaction continues with $n_e \propto t^{-3}$ and the electrons keep cooling with $T_e \propto t^{-2}$. Hence, the observed T_e becomes slightly lower in the polar direction due to the longer cooling time (the blue lines in figure 9.4). The spatial variation of T_z can also be caused by the anisotropic rarefaction. The sooner the break-out occurs, the sooner the recombination phase starts. Considering the difference of the break-out time in the directions, the ions in the polar direction experience longer recombination time. As the result, both the T_e and T_z in the polar direction are lower than those in the equatorial direction (the red lines in figure 9.4).

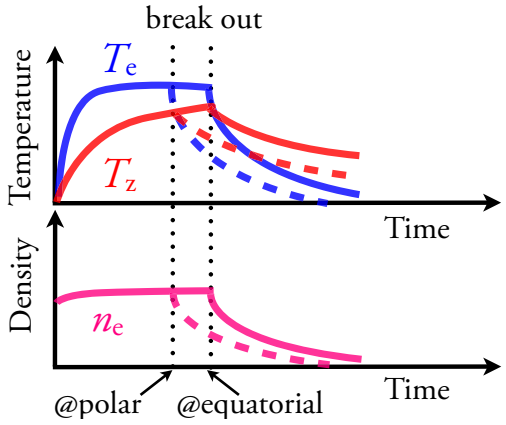

Fig. 9.4.—: Schematic view of the directional difference of T_e and T_z (upper) and n_e (lower). The blue and red lines in the upper panel respectively show the time evolutions of T_e and T_z. The evolution in the polar direction is shown by the dashed lines while that in the equatorial direction is shown by the solid lines.

If we observe such a remnant in an particular viewing angle (small slanting angle from the equatorial direction), the observed structure of the RP may be naturally explained. We give a schematic view of such an example in figure 9.5. The plasma in the equatorial direction with less cooled and recombined is concentrated near the center, while that in the polar direction with more cooled and recombined is distributed in the outer region. Shimizu et al. (2012) also found that centrally peaked X-ray morphologies are realized with anisotropic (disk-like) CSM

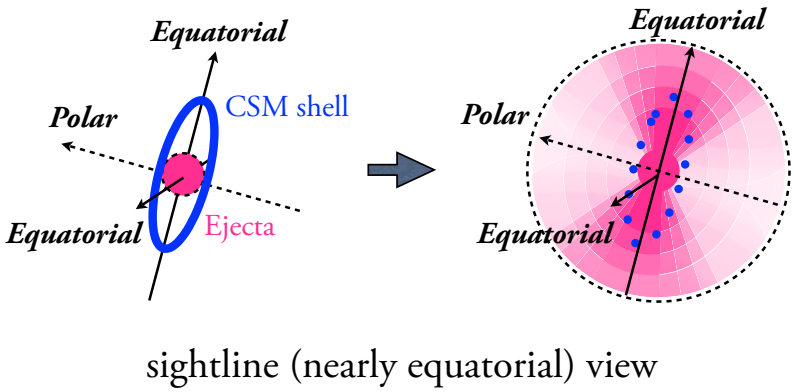

Fig. 9.5.—: Schematic view of spatial structure of the SNR before (left) and after (right) the shock break-out and the rarefaction. The red region indicates the shock-heated ejecta while the blue ellipse indicates the position of the CSM shell. The ejecta in the polar direction are more rarefied, and hence more cooled and recombined (shown in thick red region in the right panel) compared with those in the equatorial direction (shown in thin red region in the right panel).

when the line of sights are near the equatorial direction. The size of the X-ray emitting plasma is about a few 10 pc, which is consistent with the observation. Therefore, this scenario can explain all of the elemental and spatial structures of the RP, and the morphologies.

In summary, we propose that the origin of the recombining plasmas in MM SNRs is the adiabatic cooling due to shock break-out of anisotropic CSM. Since this process has not been involved in the standard SNR evolution, it can be called as “a missing branch of the SNR evolution”.

Chapter 10

Conclusion

We have investigated the plasma structures of the three non-standard SNRs in the GC region, G 1.2–0.0, G 357.7–0.1, and W 28, making use of the superior energy resolution and the large effective area of the XIS onboard the Suzaku satellite.

The X-ray morphologies of the three remnants are far from the standard shell-like structures: One has irregular shape like a blow-out from the adjacent H II region; another has a twin spherical plasma at the both ends of the elongated radio structure; the other has so-called "mixed-morphology", which is a combination of the centrally-peaked X-rays and the radio shell. All of these non-standard SNRs are located in the complex environments. The X-ray spectra have a variety of thermal structures. Among them, only the MM SNR W 28 show a clear recombining plasma based on the strong radiative recombination continua from Si and S.

Together with the previous discoveries, we confirm that the recombining plasma is selectively found in MM SNRs, if not all. Since the recombining plasma in SNRs cannot be realized in the standard thermal evolution, this result supports that some MM SNRs may have a missing branch in the evolution. We therefore search for and investigate the putative missing branch by the full-band spectroscopy in the center region and spatially resolved analyses with the recombining plasma model.

The spatial structure of the recombining plasma in W 28 show no significant correlation with the ambient molecular clouds nor with the TeV γ-ray emission. The concentration of the plasma density toward the center is revealed based on the X-ray surface brightness distribution. The outer low density region shows lower electron temperature, in good agreement with the adiabatic expansion into low density space. If the SN occurred in an equatorially dense CSM and break-out to a low density interstellar space, the apparent radial decrease both in the ionization and electron temperatures can be realized by a slanted viewing angle on this SNRs.

We found the spectrum composes of multi-ionization temperature with higher values for Si and S and lower for Ne, Mg, and Fe. These temperature variations are reproduced by a combination of the two processes; initial event to make a recombining plasma and relaxation (recombination) process to recover CIE. We found that the second phase, relaxation or recombination time, is comparable to the SNR age. This fact is consistent with either the rarefaction scenario or the photo-ionization scenario by an X-ray afterglow of a γ-ray burst. The initial condition of multi-ionization temperatures prefer the rarefaction scenario. We accordingly propose that the "missing branch" of the SNR evolution is the rarefaction process in the early stage. This missing branch makes both the mixed morphology and the recombining plasma.

Appendix A

Abbreviation

BI … back illumination

CCD … charge-coupled device

CIE … collisional ionization equilibrium

COR … cut-off rigidity

CSM … circumstellar matter

CTI … charge transfer inefficiency

CXB … cosmic X-ray background

EEF … encircled-energy fraction

EOB … extensible optical bench

FI … front illumination

FOV … field of view

FS … frame store

FWHM … full width at half maximum

GC … Galactic center

GDXE … Galactic diffuse X-ray emission

GMC … giant molecular cloud

HPD … half-power diameter

IA … imaging area

IP … ionizing plasma

ISM … interstellar medium

MC … molecular cloud

MM SNR … mixed-morphology SNR

NEI … non-equilibrium ionization

NXB … non–X-ray background

PSF … point spread function

PWN … pulsar wind nebula

QE … quantum efficiency

RP … recombining plasma

RRC … radiative recombination continua

SCI … spaced-row charge injection

SN … supernova

SNR … supernova remnant

Sgr … Sagittarius

XIS … X-ray imaging spectrometer

XRT … X-ray telescope

d.o.f. … degree of freedom

Appendix B

Spatially Resolved Spectra of W 28

In this chapter, we give the spatially resolved spectra of W 28. The best-fit single-T_z RP models for the fitting in the 1.7–5.0 keV band are also shown. The definition of the sector numbers are indicated in figure 8.5.

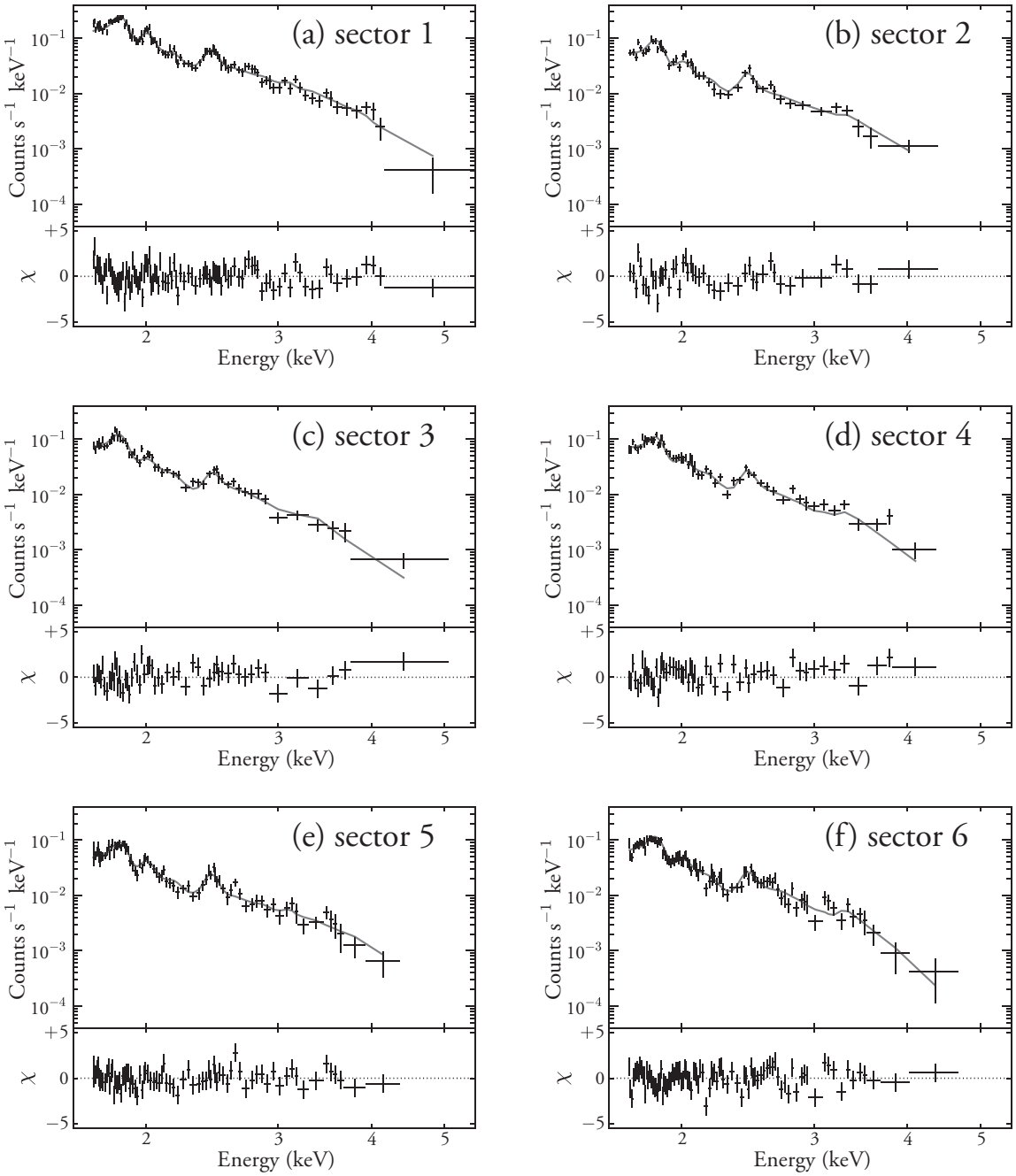

Fig. B.1.—: The background-subtracted spectra (crosses) and the best-fit models (curves) of the divided sectors (figure 8.5). The FI and BI spectra were simultaneously fitted for each sector, although only the data and model for FI are shown for simplicity. The data without vertical bars indicate the 1-σ upper limit.

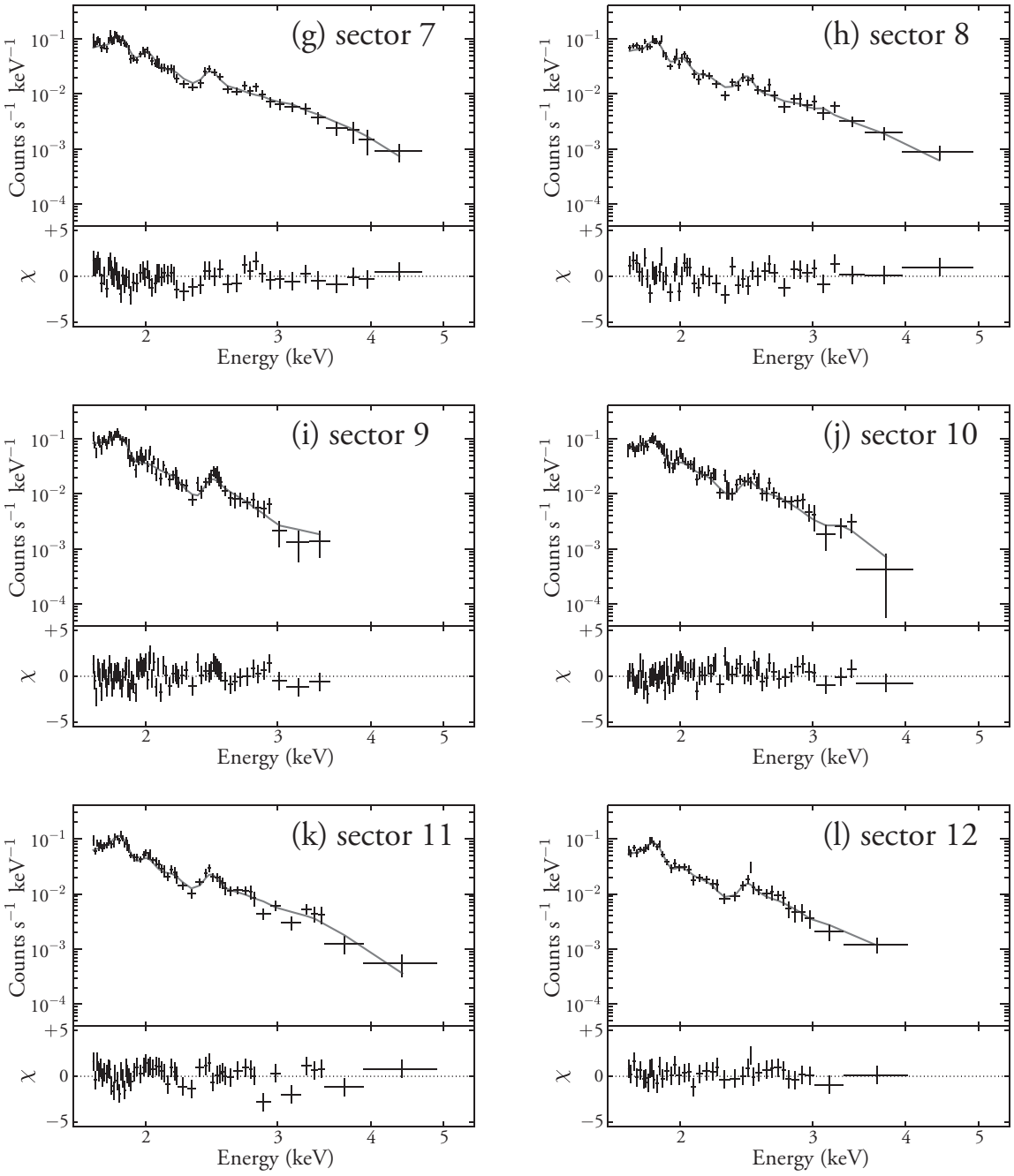

Fig. B.1.—: *Continued.*

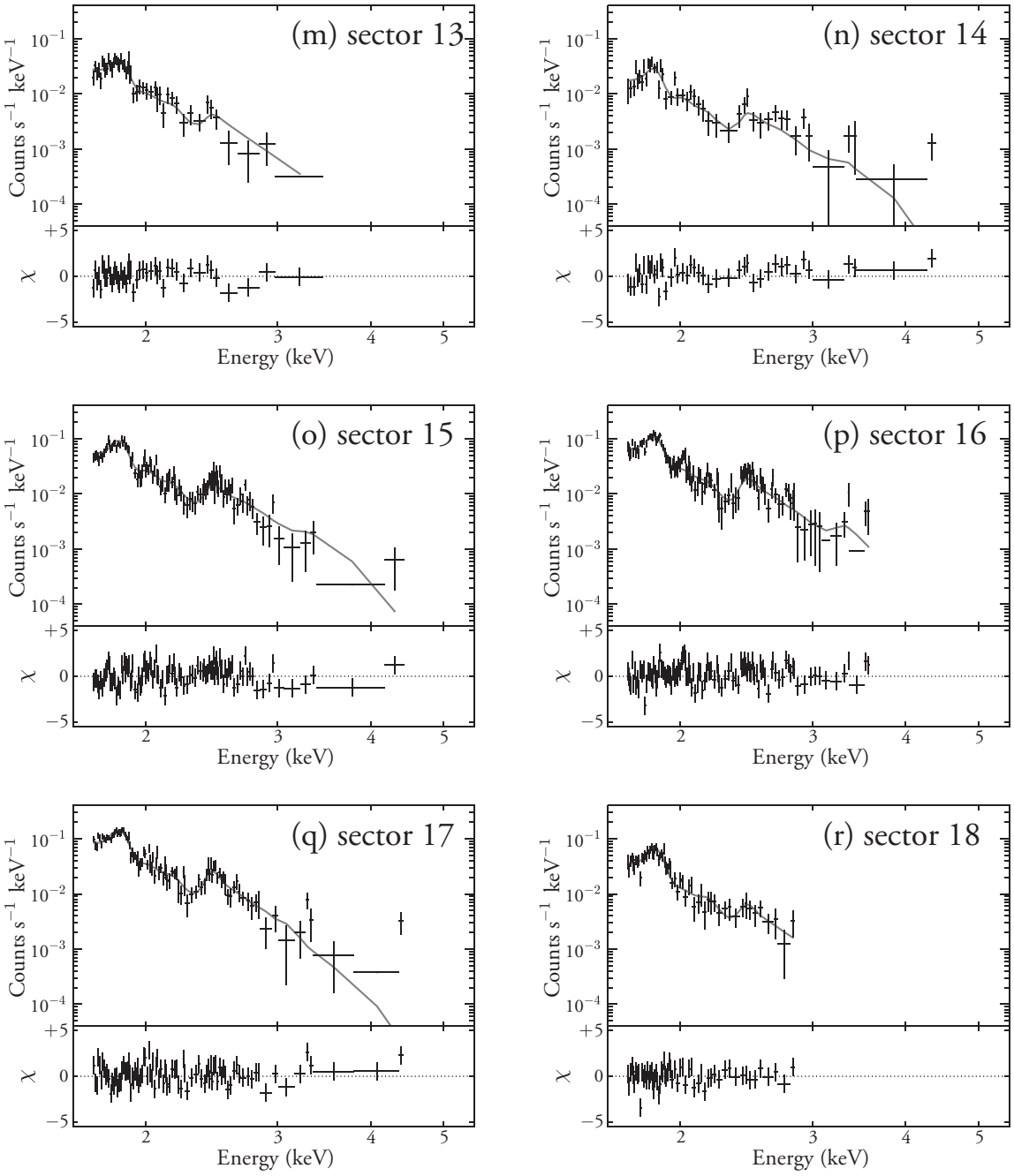

Fig. B.1.—: *Continued.*

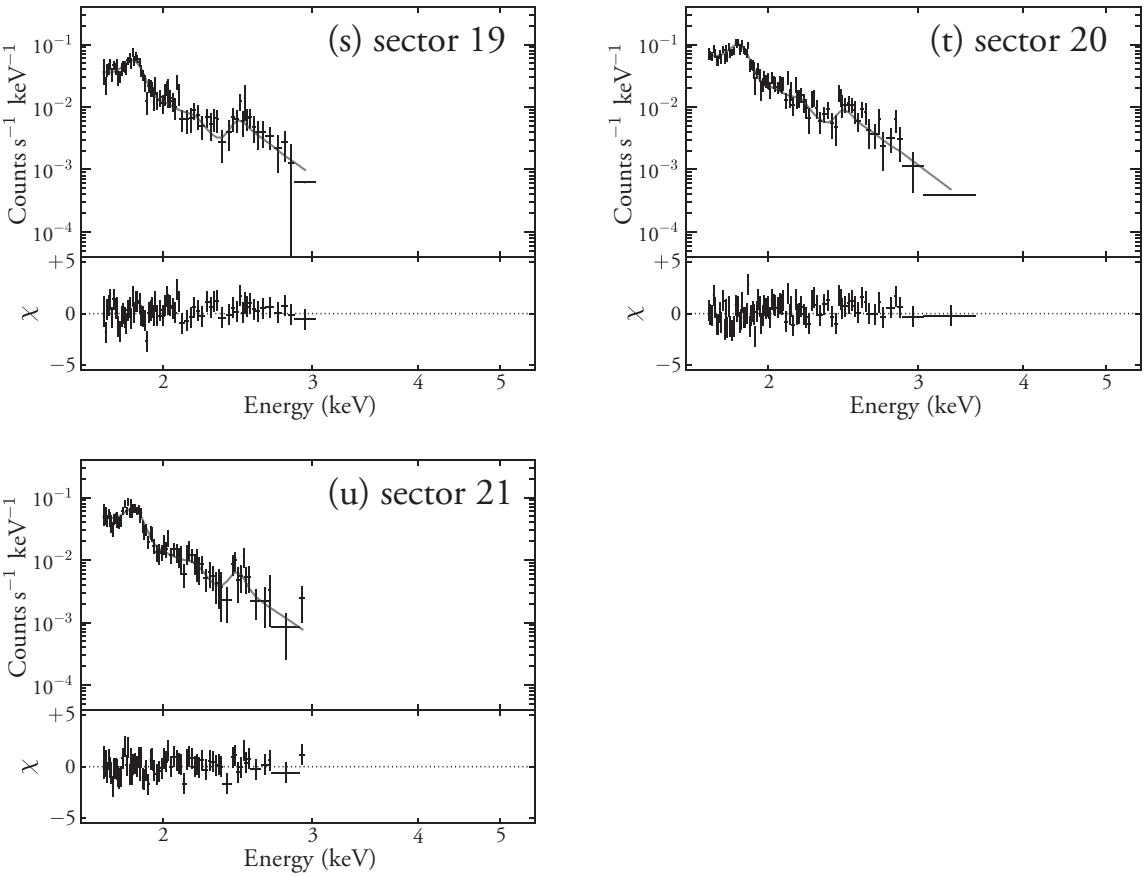

Fig. B.1.—: *Continued.*

Appendix C

Simulation of Ionization Temperatures

Contents

In this chapter, we give the simulations of ionization temperatures in ionizing and recombining plasmas (§ 4.3.3). For this purpose, we use the non-equilibrium ionization jump (Neij) model in the SPEX software. The brief description of the model is given in § C.1 and the results are in § C.2 and § C.3.

In the calculations, we use the SPEX version 2.02.02 with the solar abundance of Anders & Grevesse (1989) and the ionization balance tables from Arnaud & Raymond (1992) for Fe and Arnaud & Rothenflug (1985) for the other elements.

C.1 Non-Equilibrium Ionization Jump Model

We show a schematic view of the Neij model in figure C.1. The plasma is initially in CIE with a temperature of T_1, then instantaneously heated (ionizing case: figure C.1a) or cooled (recombining case: figure C.1b) to T_2. Under the constant electron temperature of $T_e = T_2$ and the uniform electron density of n_e, the ionization temperatures of ions gradually change from T_1 to T_2. The model calculates the ionization states and the spectrum after time t. The parameters are T_1, T_2, and $\tau = n_e t$. As already noted in § 4.3.3, the typical timescale to recover CIE is 10^{12-13} cm s^{-1}.

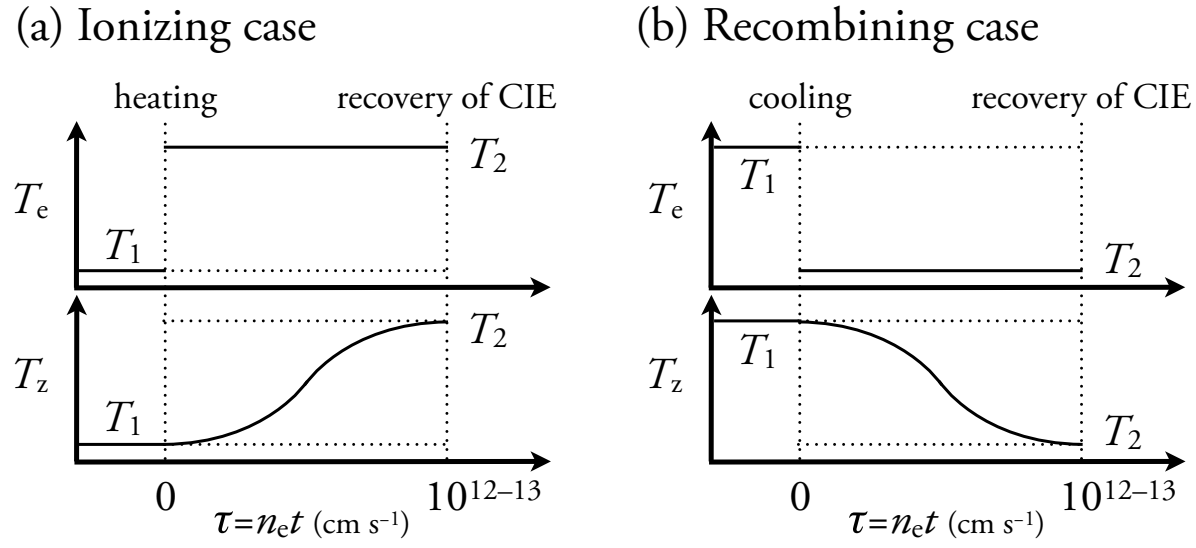

Fig. C.1.—: A schematic view of the Neij model for (a) ionizing plasmas ($T_1 < T_2$) and (b) recombining plasmas ($T_1 > T_2$).

Although the model can calculate the spectra and the ion concentrations, it does not directly derive the ionization temperatures. Hence, we need to convert the obtained ion concentrations to the ionization temperatures.

In the following sections (§ C.2 and § C.3), we first give the average charges in ionizing and recombining plasmas. The derived average charges are converted to the corresponding ionization temperatures by using figure 4.4.

C.2 Ionizing Plasmas

Ionizing plasmas are the characteristic of the standard SNR plasmas (see § 2.1 and § 4.3). Thus, we assume the cold and neutral initial conditions for ionizing plasmas ($T_1 \sim$0 keV).

The evolution of the average charges and ionization temperatures for several T_2 are given in figures C.2 and C.3, respectively. Each color in the figures show the equi-$n_e t$ lines. As shown in figure C.2, lighter elements have shorter timescales to reach to nearly CIE, because they have less electrons to be ionized (for example, see the green line in the lower-right panel of figure C.2).

In addition to this Z dependence, another trend of elemental difference exists. This is more clearly seen in figure C.3, the evolution of the ionization temperatures. In this figure, the equi-$n_e t$ lines become denser where the ionization process takes longer time. We see the ionization process takes longer time near the ionization states with the complete valence shells (Ne-like and He-like ions: for example, see the upper-left panel of figure C.3. the lines are denser near $T_z \sim$0.1 keV for O and $T_z \sim$0.15 keV for Si.) This is because of the higher ionization potentials at the complete valence shells.

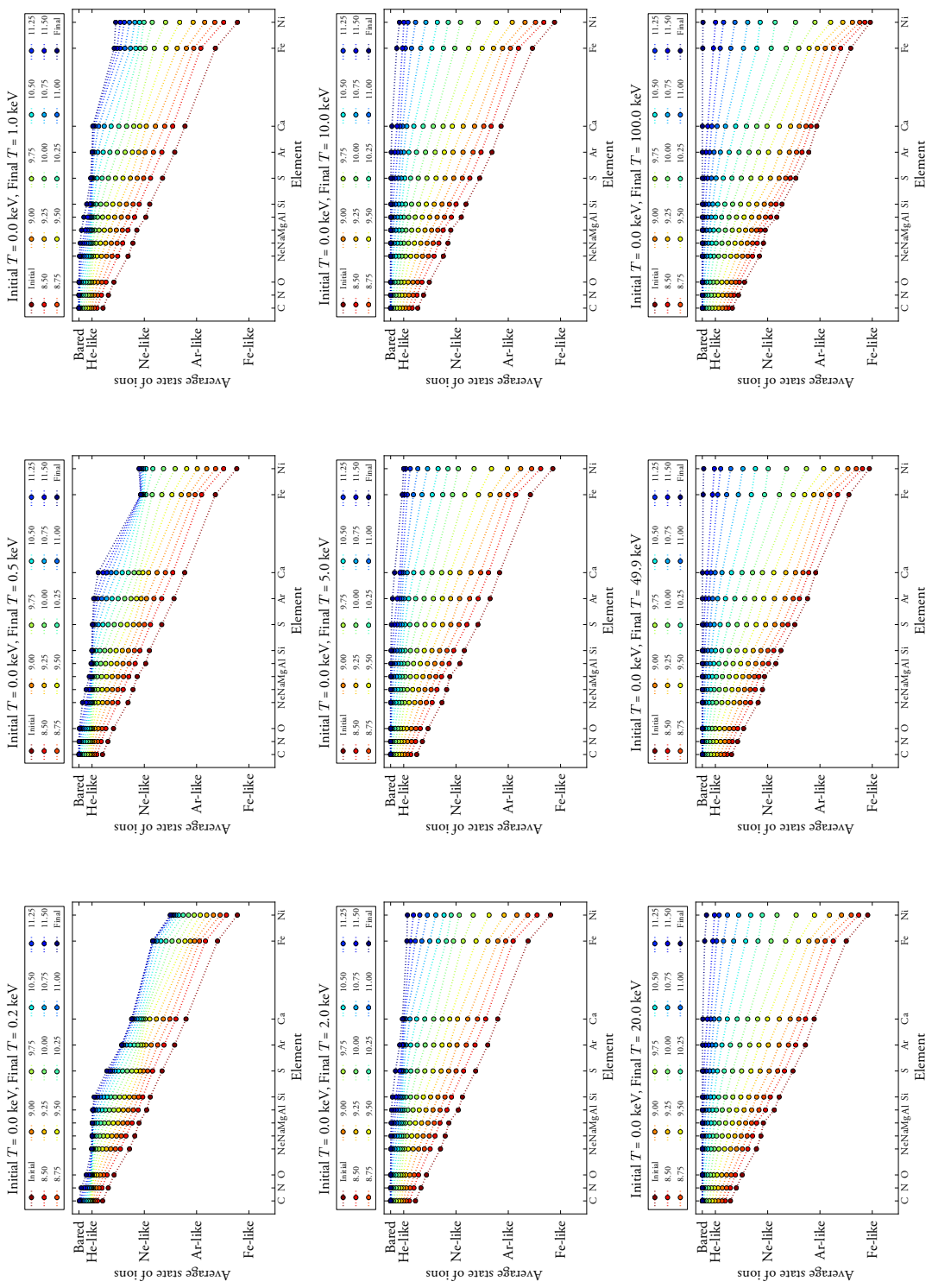

Fig. C.2.—: The evolution of average charges in ionizing plasmas. The initial temperatures (T_1) are assumed to be $\sim$0 keV. Each panel shows the result for different final temperature (T_2 = 0.2, 0.5, 1.0, 2.0, 5.0, 10.0, 20.0, 50.0, and 100.0 keV).

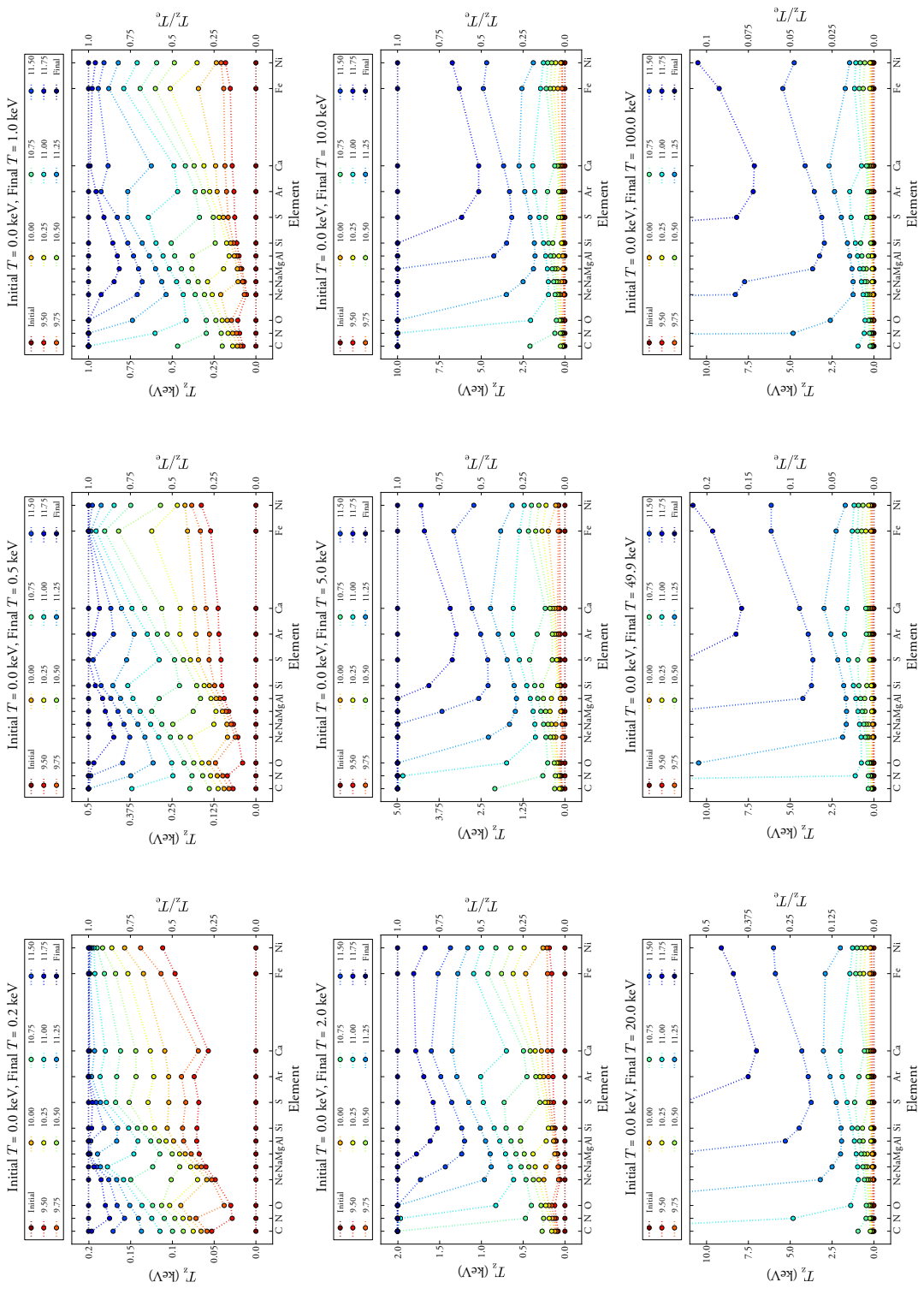

Fig. C.3.—: Same as figure C.2 but for the evolution of the ionization temperatures. For $T_2 > 10$ keV, we restrict the vertical range to be $T_z \lesssim 10$ keV for display.

C.3 Recombining Plasmas

As the initial and final conditions of recombining plasmas are not obvious, we simulate several sets of different T_1 and T_2 values. The evolution of the average charges and ionization temperatures are given in figures C.4 and C.5, respectively. Similar to the ionization timescale, the recombination timescale basically shows the trend that it is shorter for lighter elements and longer for heavier elements, because the heavier elements can recombine more electrons.

The elemental difference is much more complicated in the evolution of the ionization temperatures (figure C.5). The change of T_z in unit time ($n_e t$) becomes large at specific ranges of T_z, depending on the elements. For example, in the upper-right panel of figure C.5, the equi-$n_e t$ lines of Mg and Fe are sparser than that of S near T_z=0.4 keV. At this ionization temperature, the average ionization states of Mg and Fe are He-like and Ne-like (see figure 4.4). Because the ionization potentials of the complete–valence-shell ions are high, the drops of T_z per one capture is large for these ions than those for the ions of the other ionization states. Hence, the apparent changes of T_z becomes larger when the ions pass through the Ne-like and He-like ionization states. We see the elemental difference of the evolution of T_z does not depend much on the boundary conditions (T_1 and T_2) in the transitional phases.

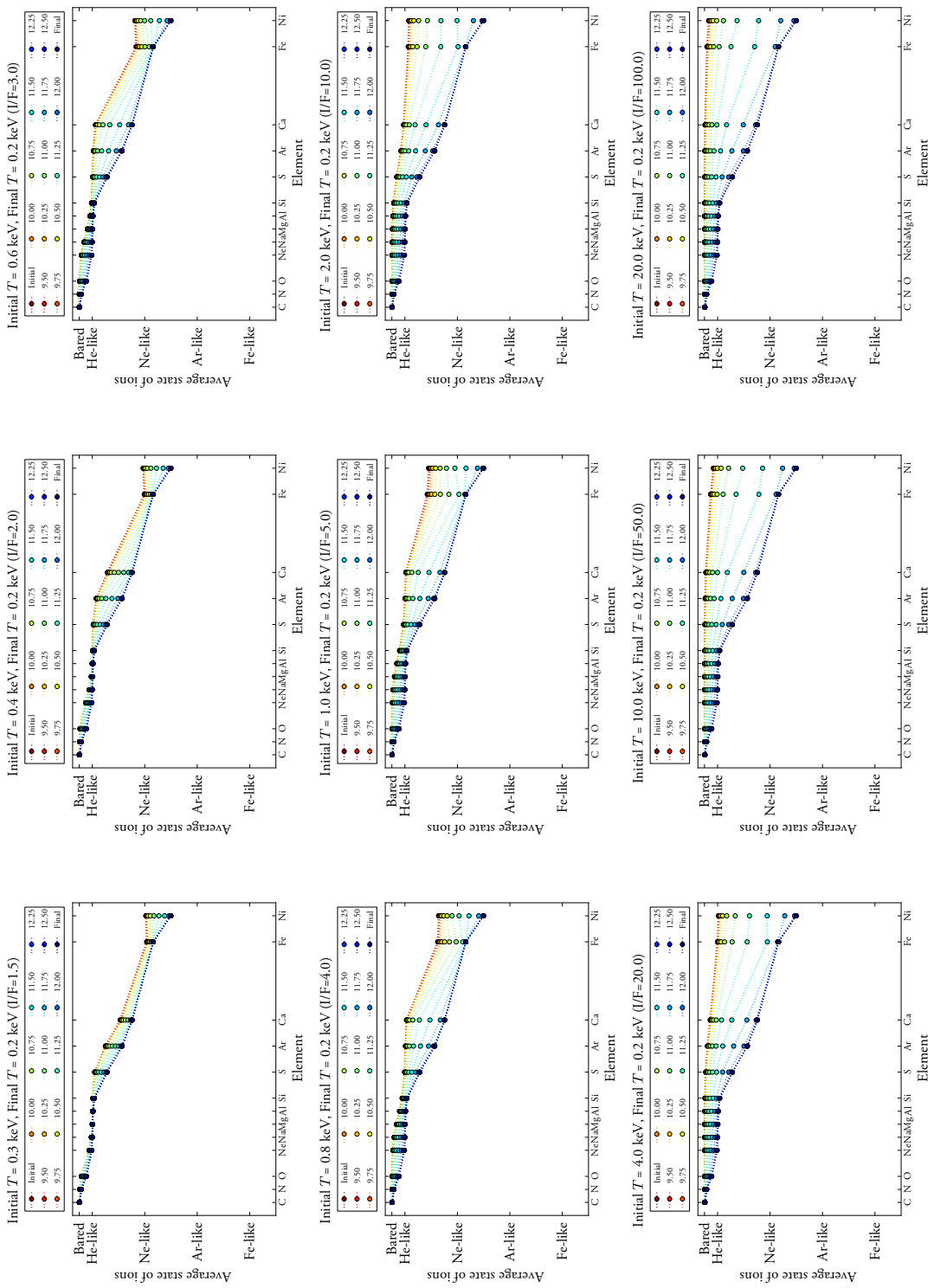

Fig. C.4.—: The evolution of average charges in recombining plasmas. Each panel shows the result for different combination of the initial and final temperatures. The results of $T_1/T_2 = 1.5$, 2.0, 3.0, 4.0, 5.0, 10.0, 20.0, 50.0, and 100.0 are shown. (a) $T_2 = 0.2$ keV.

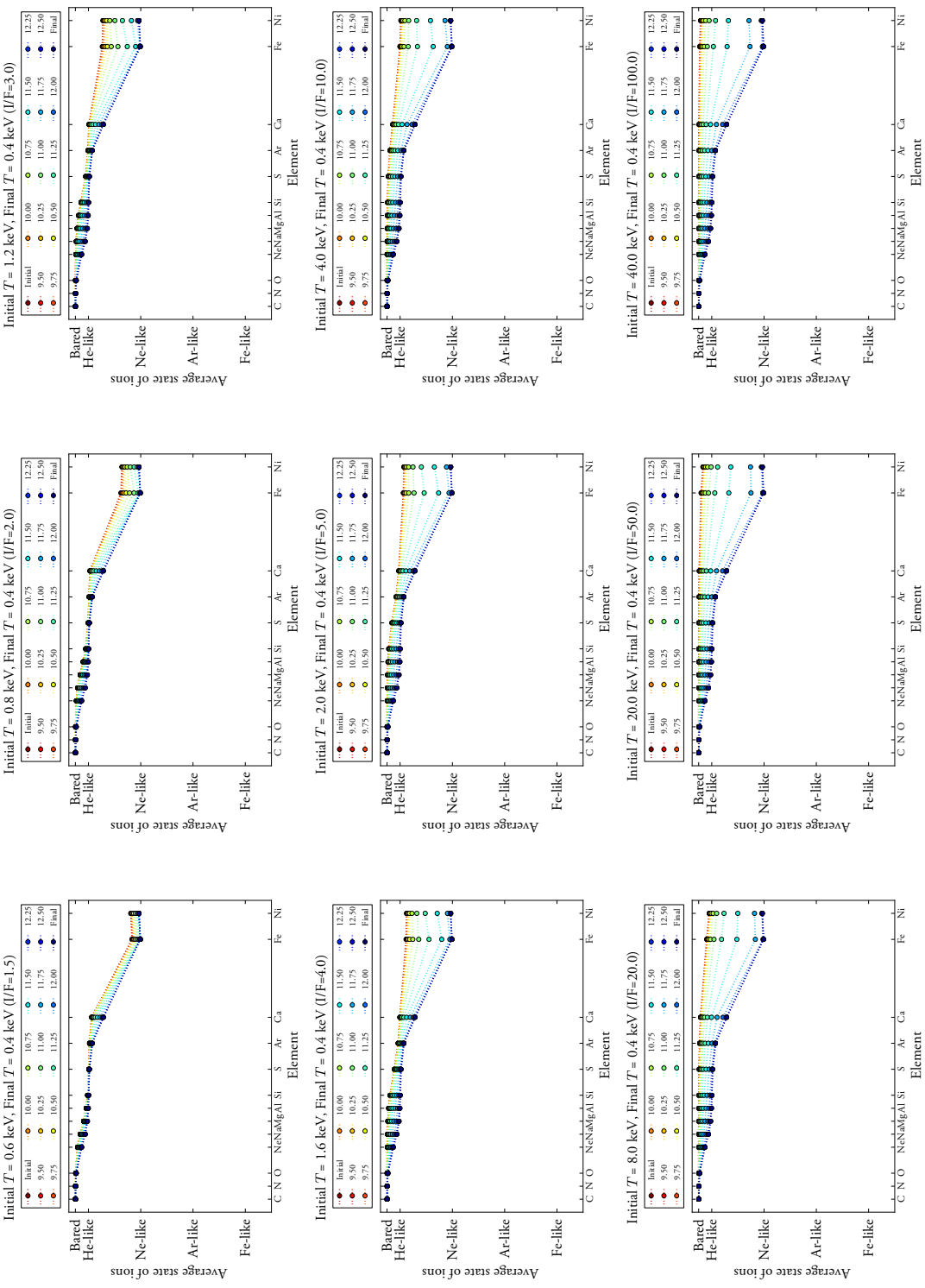

Fig. C.4.—: *Continued.* (b) $T_2 = 0.4$ keV

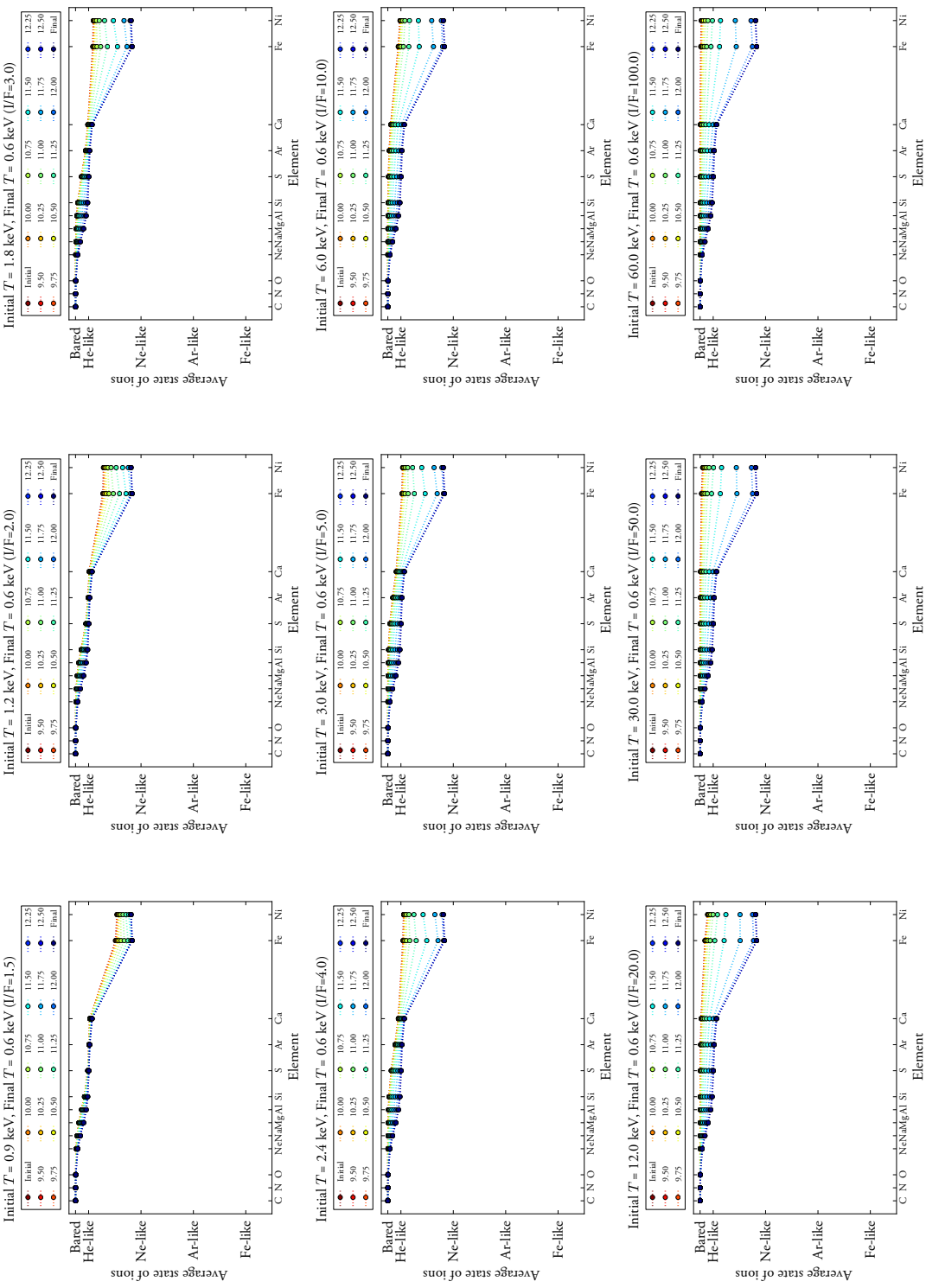

Fig. C.4.—: *Continued.* (c) $T_2 = 0.6$ keV

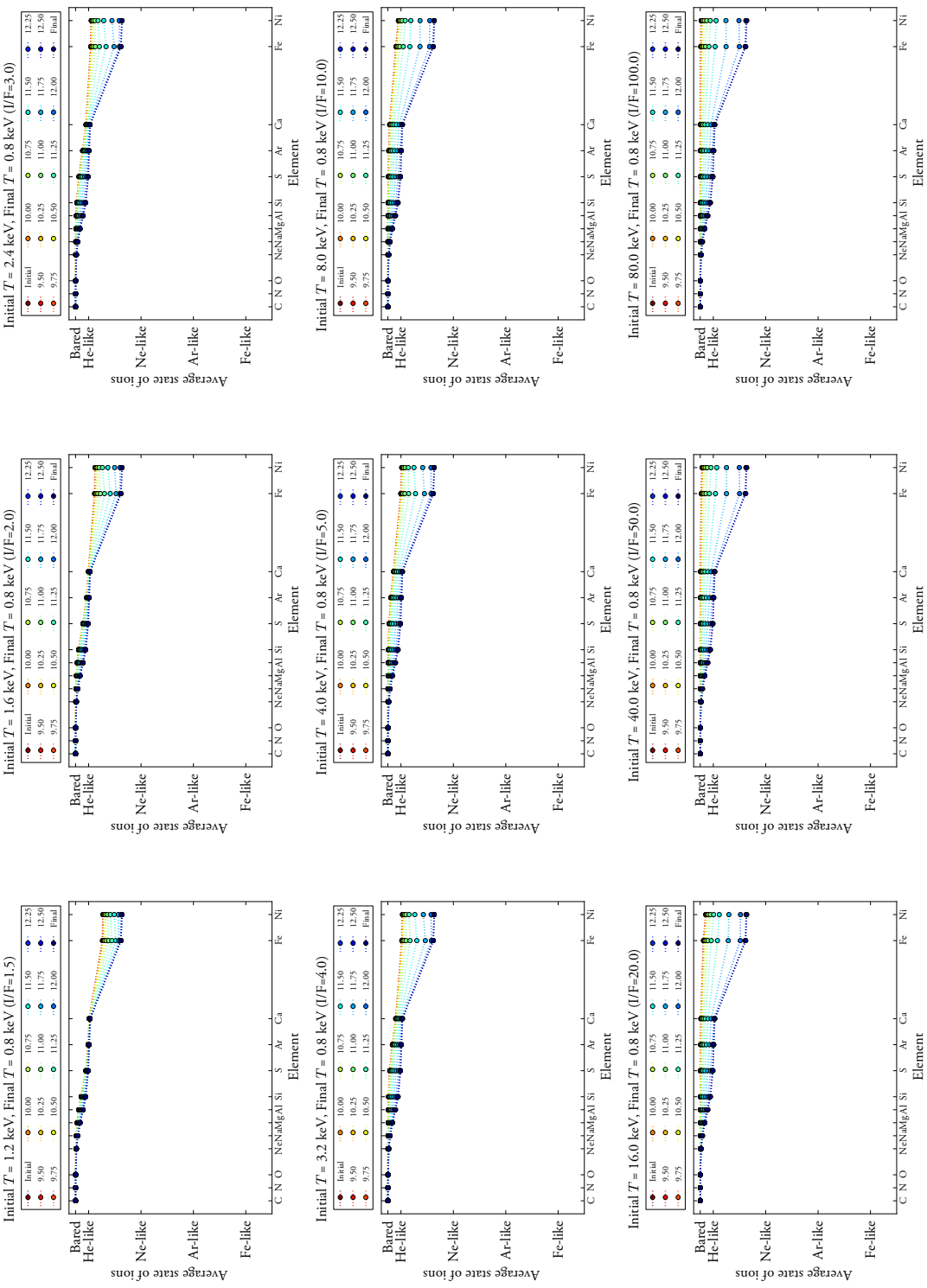

Fig. C.4.—: *Continued.* (d) $T_2 = 0.8$ keV

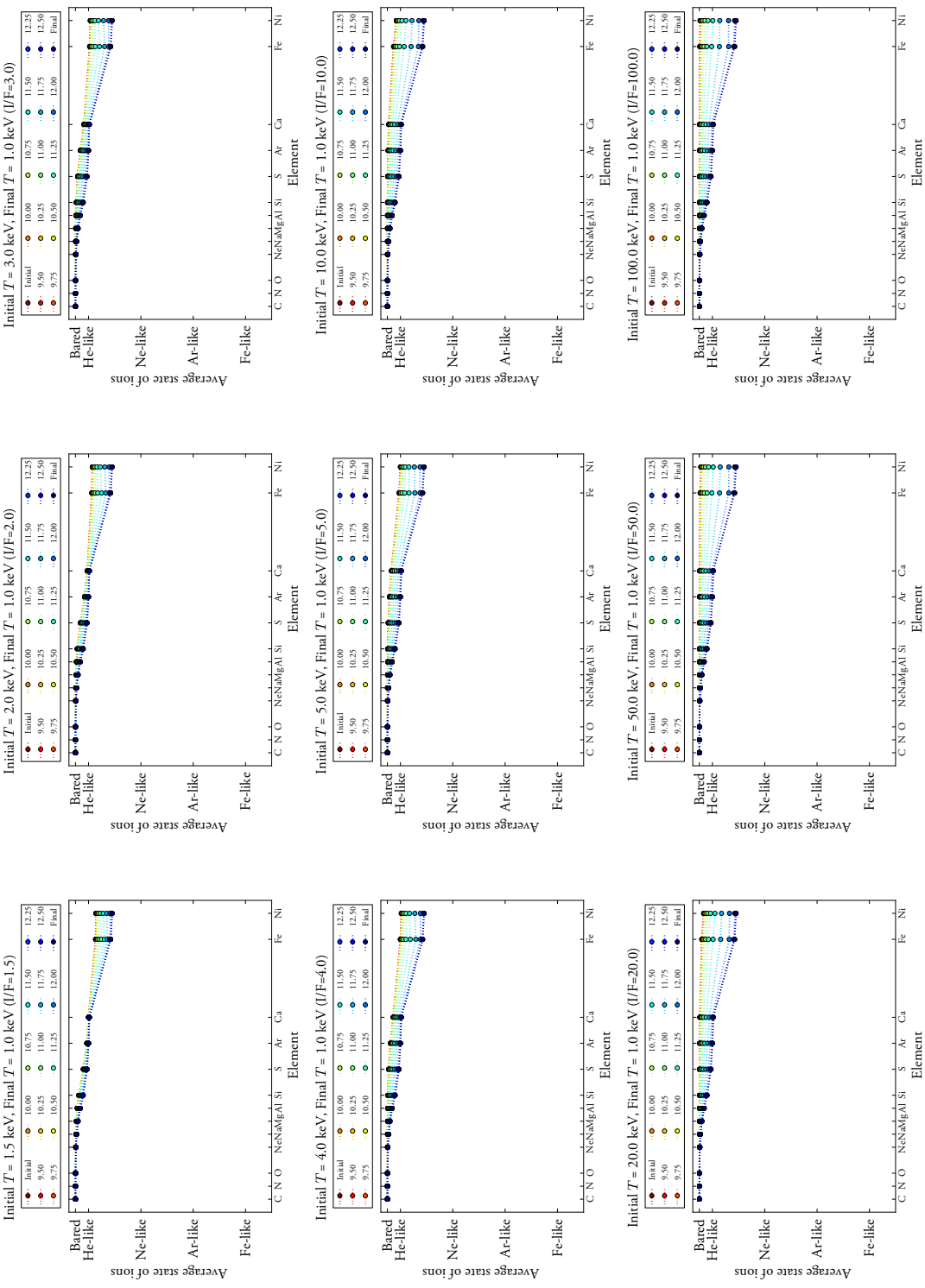

Fig. C.4.—: *Continued.* (e) $T_2 = 1.0$ keV

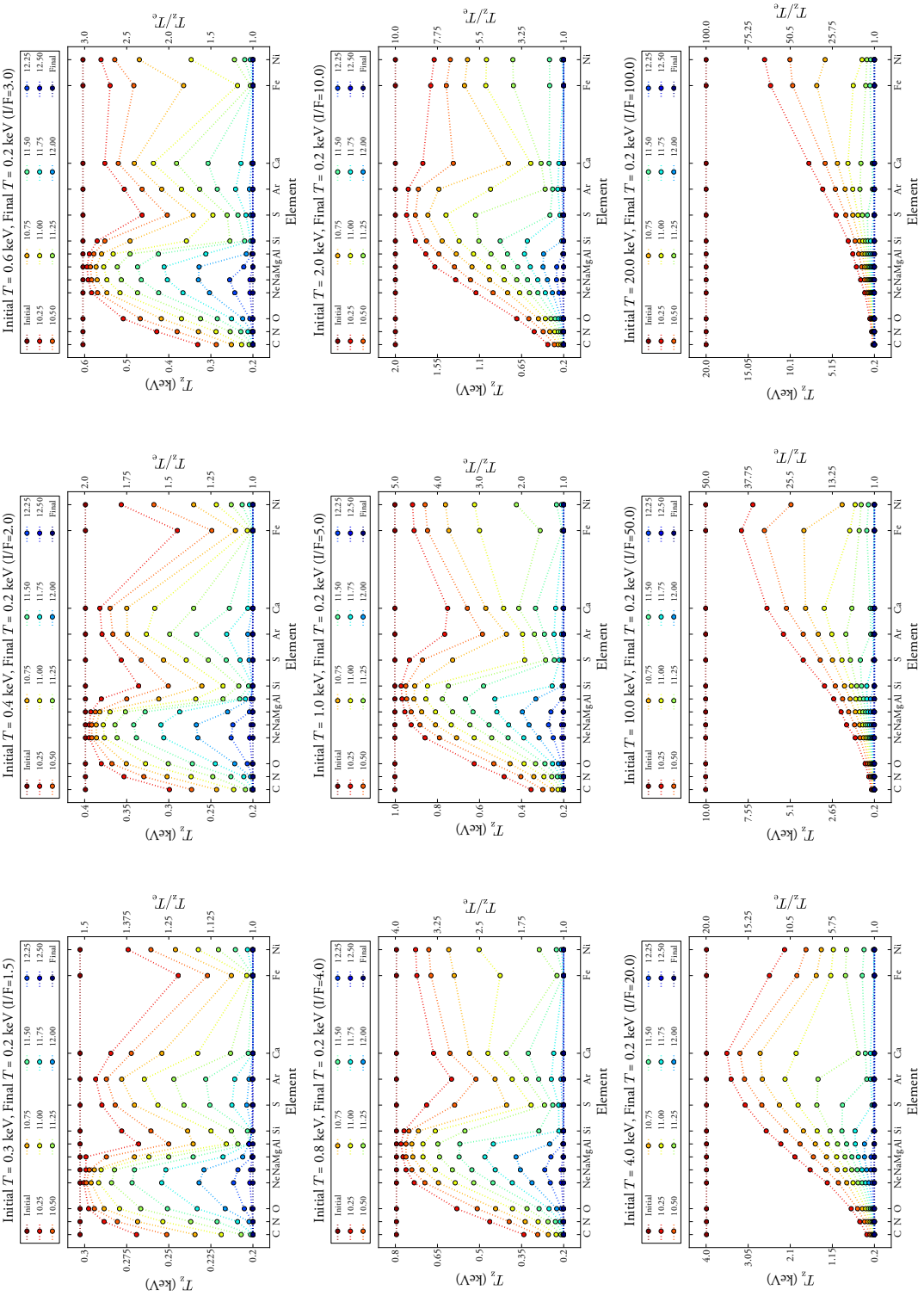

Fig. C.5.—: Same as figure C.4 but for the evolution of the ionization temperatures. (a) $T_2 = 0.2$ keV.

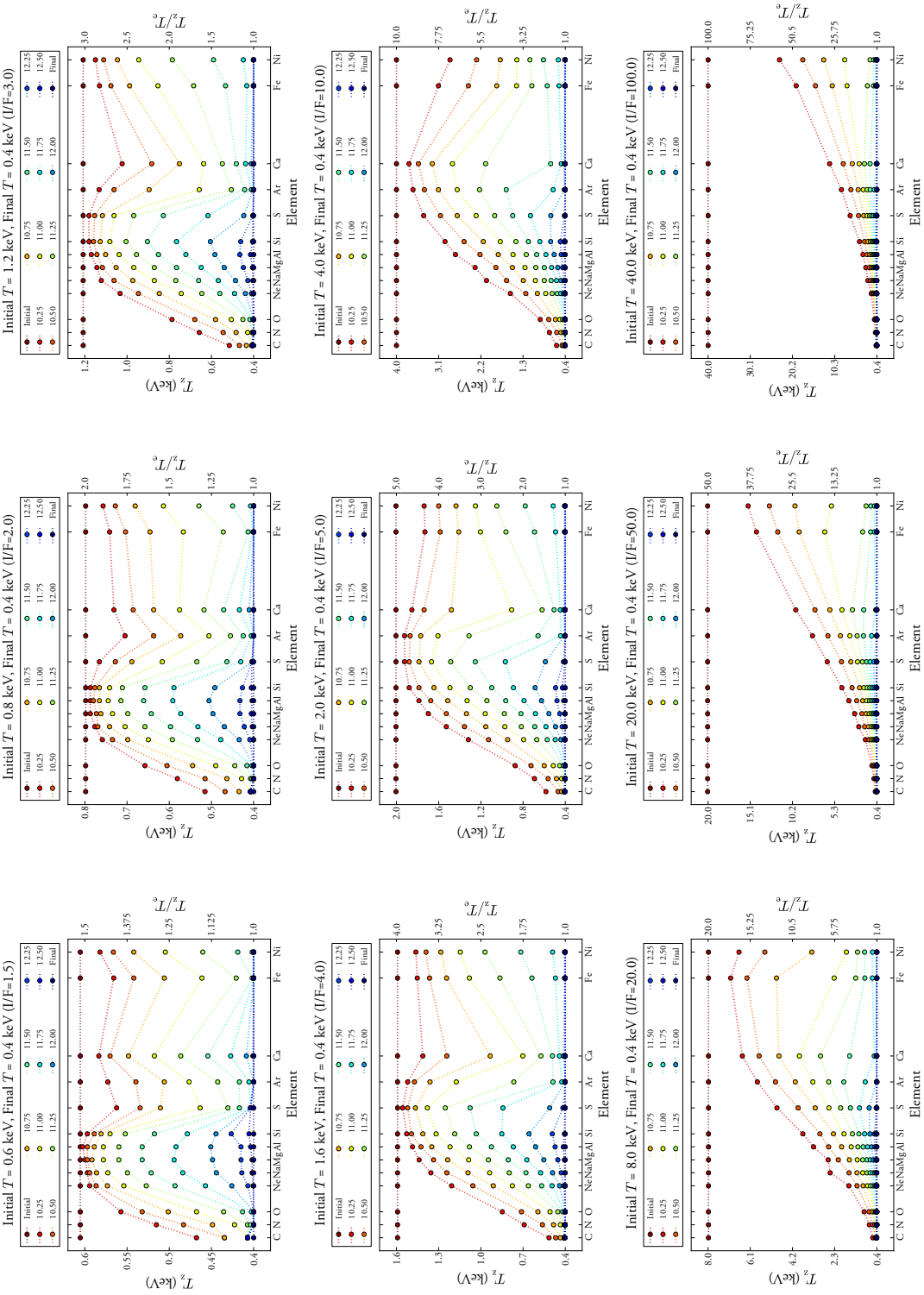

Fig. C.5.—: *Continued.* (b) $T_2 = 0.4$ keV.

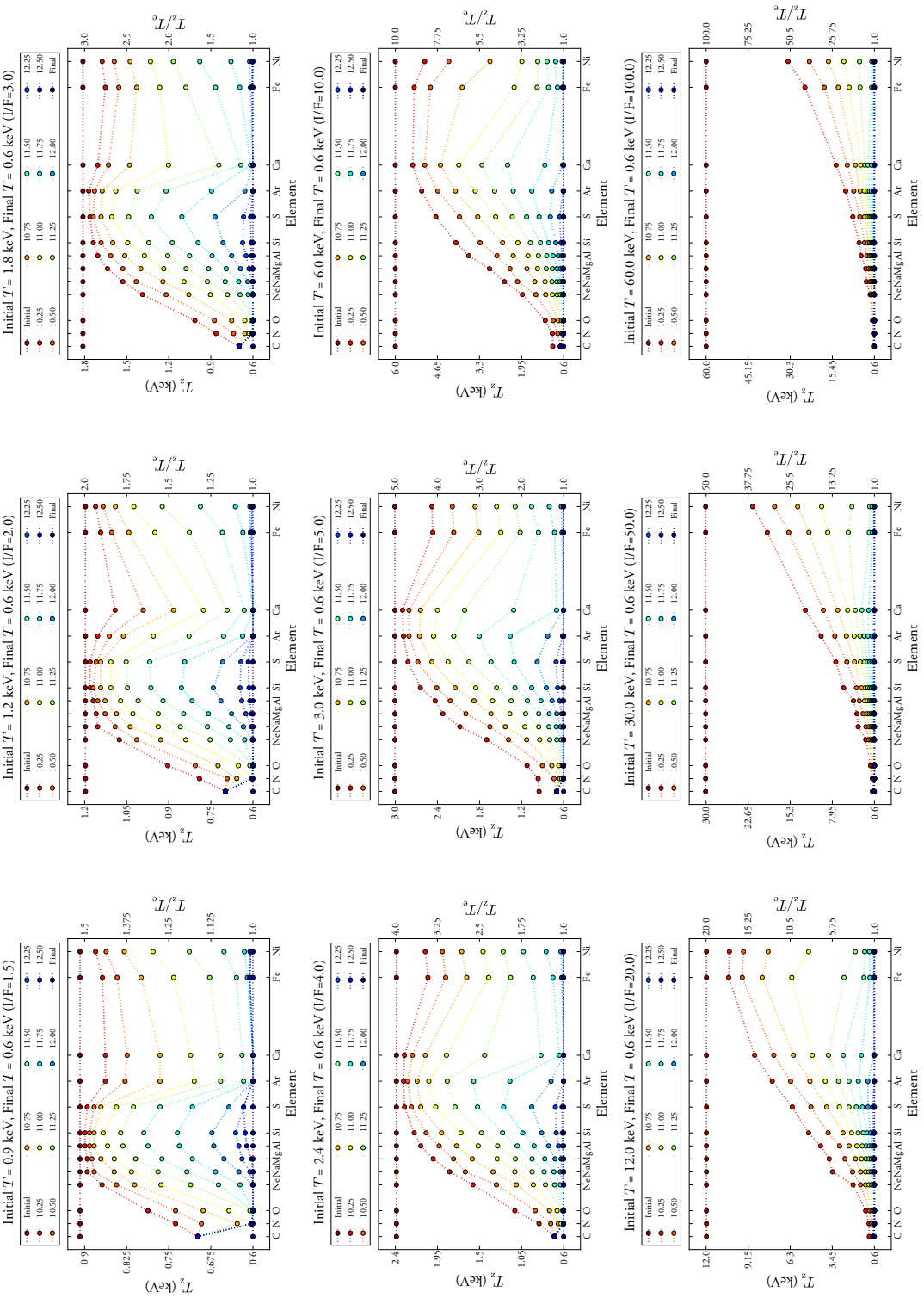

Fig. C.5.—: *Continued.* (c) $T_2 = 0.6$ keV.

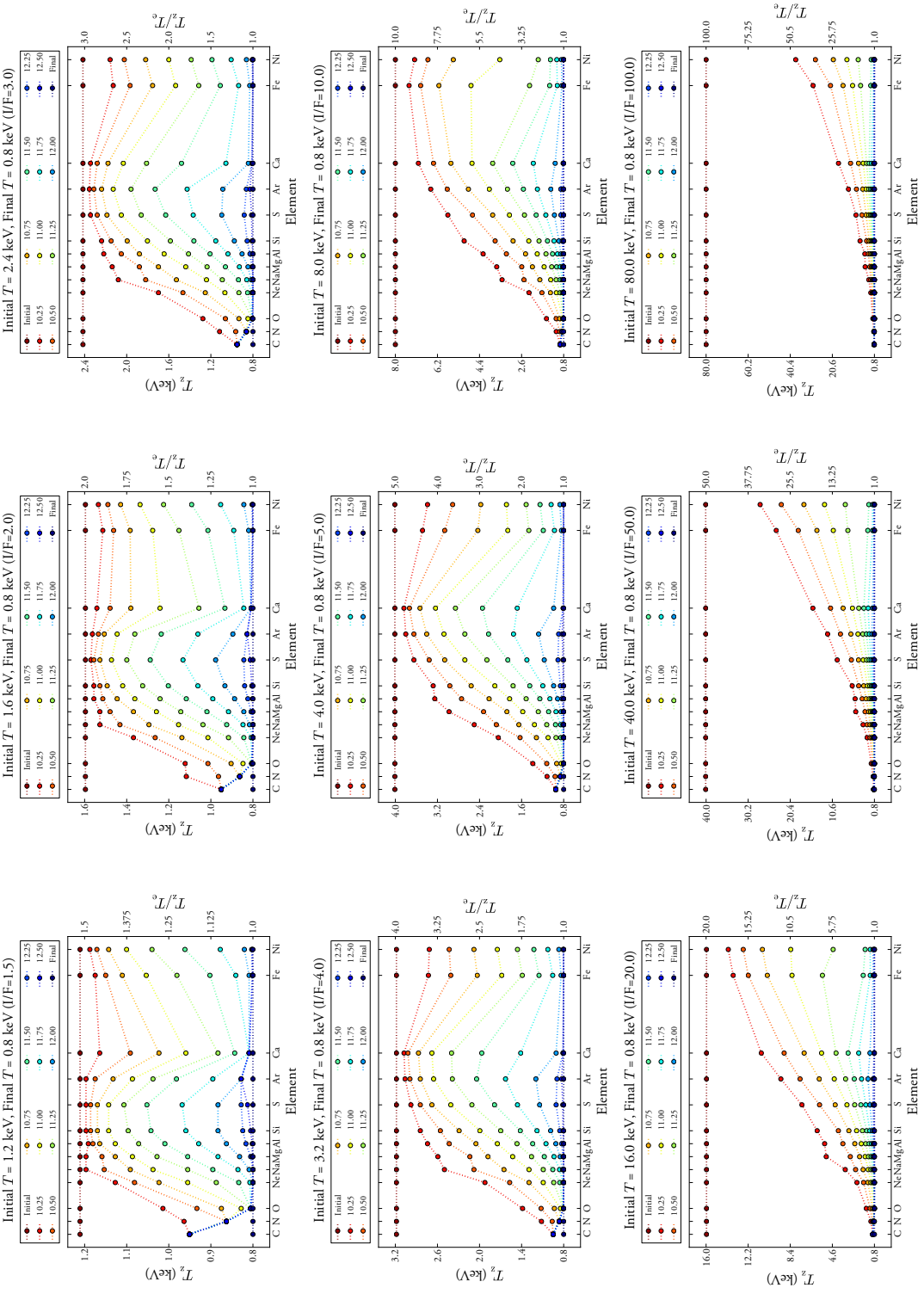

Fig. C.5.—: *Continued.* (d) $T_2 = 0.8$ keV.

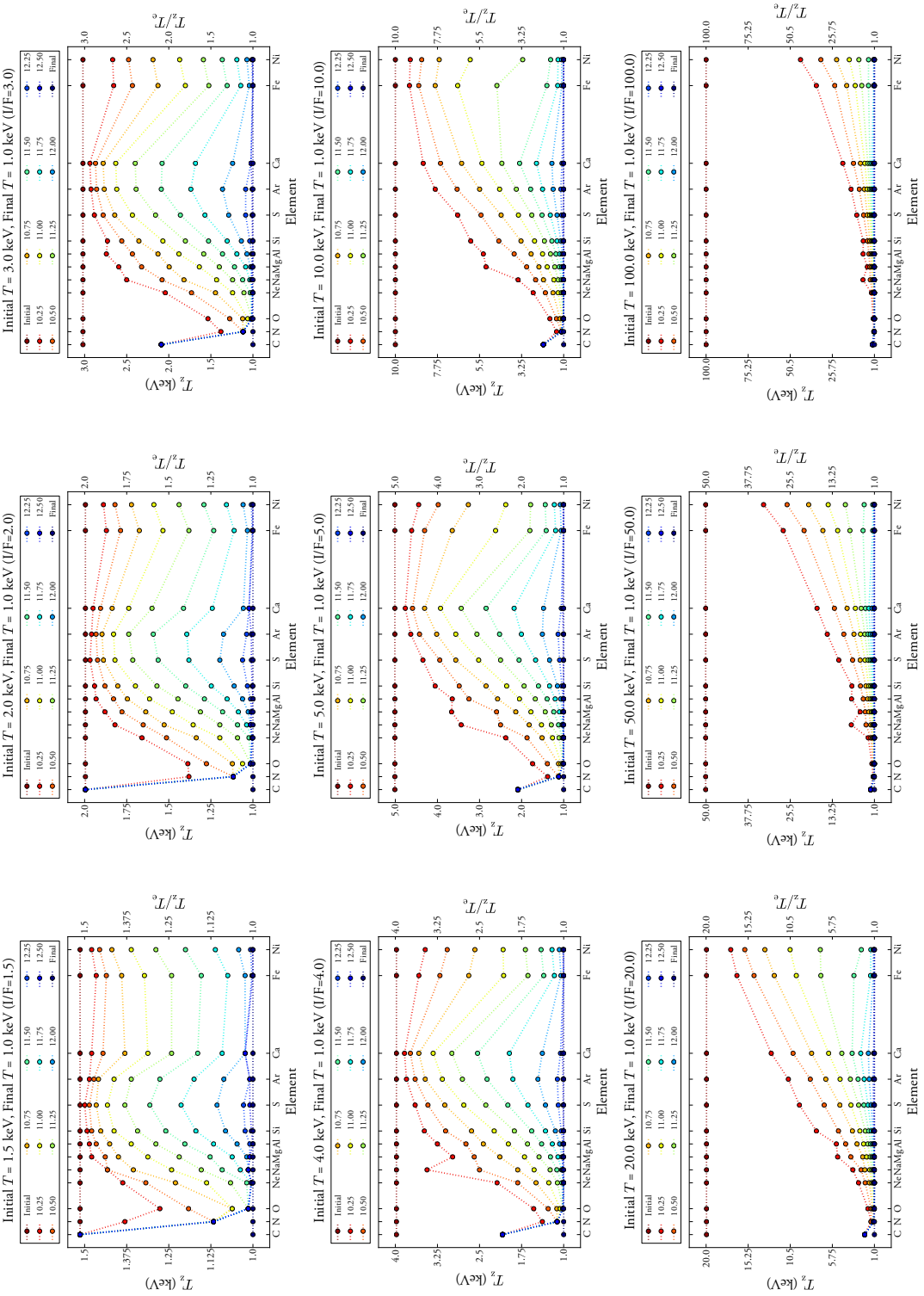

Fig. C.5.—: *Continued.* (e) $T_2 = 1.0$ keV.

References

Abdo, A. A., Ackermann, M., Ajello, M., et al. 2010a, ApJ, 712, 459

Abdo, A. A., Ackermann, M., Ajello, M., et al. 2010b, ApJ, 718, 348

Aharonian, F., Akhperjanian, A. G., Bazer-Bachi, A. R., et al. 2008, A&A, 481, 401

Anders, E., & Grevesse, N. 1989, Geochim. Cosmochim. Acta, 53, 197

Angelini, L., & White, N. E. 2003, ApJ, 586, L71

Arikawa, Y., Tatematsu, K., Sekimoto, Y., & Takahashi, T. 1999, PASJ, 51, L7

Arnaud, M., & Rothenflug, R. 1985, A&AS, 60, 425

Arnaud, M., & Raymond, J. 1992, ApJ, 398, 394

Arnaud, K. A. 1996, Astronomical Data Analysis Software and Systems V, 101, 17

Baganoff, F. K., et al. 2003, ApJ, 591, 891

Bautz, M. W., Kissel, S. E., Prigozhin, G. Y., LaMarr, B., Burke, B. E., & Gregory, J. A. 2004, Proc. SPIE, 5501, 111

Becker, R. H., & Helfand, D. J. 1985, Nature, 313, 115

Becker, R. H., Smith, B. W., White, N. E., Holt, S. S., Boldt, E. A., Mushotzky, R. F., & Serlemitsos, P. J. 1979, ApJ, 234, L73

Berger, E., Kulkarni, S. R., & Frail, D. A. 2003, ApJ, 590, 379

Blum, R. D., & Damineli, A. 1999, ApJ, 512, 237

Borkowski, K. J., Lyerly, W. J., & Reynolds, S. P. 2001, ApJ, 548, 820

Brickhouse, N. S., Dupree, A. K., Edgar, R. J., et al. 2000, ApJ, 530, 387

Brogan, C. L., Gelfand, J. D., Gaensler, B. M., Kassim, N. E., & Lazio, T. J. W. 2006, ApJ, 639, L25

Caswell, J. L., Kesteven, M. J., Bedding, T. R., & Turtle, A. J. 1989, Proceedings of the Astronomical Society of Australia, 8, 184

Chevalier, R. A. 1974, ApJ, 188, 501

Cioffi, D. F., McKee, C. F., & Bertschinger, E. 1988, ApJ, 334, 252

Claussen, M. J., Goss, W. M., Frail, D. A., & Desai, K. 1999, ApJ, 522, 349

Cunha, K., Sellgren, K., Smith, V. V., Ramirez, S. V., Blum, R. D., & Terndrup, D. M. 2007, ApJ, 669, 1011

Dickel, J. R., Milne, D. K., Kerr, A. R., & Ables, J. G. 1973, Australian Journal of Physics, 26, 379

Dickey, J. M., & Lockman, F. J. 1990, ARA&A, 28, 215

Downes, D., & Maxwell, A. 1966, ApJ, 146, 653

Downes, D., Goss, W. M., Schwarz, U. J., & Wouterloot, J. G. A. 1979, A&AS, 35, 1

Dubner, G. M., Velázquez, P. F., Goss, W. M., & Holdaway, M. A. 2000, AJ, 120, 1933

Dutra, C. M., Ortolani, S., Bica, E., Barbuy, B., Zoccali, M., & Momany, Y. 2003, A&A, 408, 127

Dwarkadas, V. V., & Chevalier, R. A. 1998, ApJ, 497, 807

Evans, I. N., et al. 2010, ApJS, 189, 37

Ezoe, Y., Kokubun, M., Makishima, K., Sekimoto, Y., & Matsuzaki, K. 2006, ApJ, 638, 860

Frail, D. A., Goss, W. M., Reynoso, E. M., Giacani, E. B., Green, A. J., & Otrupcek, R. 1996, AJ, 111, 1651

Gaensler, B. M., Fogel, J. K. J., Slane, P. O., Miller, J. M., Wijnands, R., Eikenberry, S. S., & Lewin, W. H. G. 2003, ApJ, 594, L35

Goudis, C. 1976, Ap&SS, 40, 91

Green, D. A. 2009, Bulletin of the Astronomical Society of India, 37, 45

Gu, M. F., Chen, H., Brown, G. V., Beiersdorfer, P., & Kahn, S. M. 2007, ApJ, 670, 1504

Helfand, D. J., & Becker, R. H. 1985, Nature, 313, 118

Hewitt, J. W., Yusef-Zadeh, F., & Wardle, M. 2009, ApJ, 706, L270

Hughes, J. P., & Helfand, D. J. 1985, ApJ, 291, 544

Hyodo, Y., Tsujimoto, M., Hamaguchi, K., Koyama, K., Kitamoto, S., Maeda, Y., Tsuboi, Y., & Ezoe, Y. 2008, PASJ, 60, S85

Ioka, K., Kobayashi, S., & Mészáros, P. 2004, ApJ, 613, L17

Ishisaki, Y., et al. 2007, PASJ, 59, S113

Itoh, H., & Masai, K. 1989, MNRAS, 236, 885

Jansen, F., et al. 2001, A&A, 365, L1

Jiang, B., Chen, Y., Wang, J., et al. 2010, ApJ, 712, 1147

Kaastra, J. S., Mewe, R., & Nieuwenhuijzen, H. 1996, UV and X-ray Spectroscopy of Astrophysical and Laboratory Plasmas, 411

Kaastra, J. S., Paerels, F. B. S., Durret, F., Schindler, S., & Richter, P. 2008, Space Sci. Rev., 134, 155

Kallman, T. R., & McCray, R. 1982, ApJS, 50, 263

Kaspi, V. M., Lyne, A. G., Manchester, R. N., et al. 1993, ApJ, 409, L57

Kawasaki, M. T., Ozaki, M., Nagase, F., et al. 2002, ApJ, 572, 897

Kawasaki, M., Ozaki, M., Nagase, F., Inoue, H., & Petre, R. 2005, ApJ, 631, 935

Kelley, R. L., Mitsuda, K., Allen, C. A., et al. 2007, PASJ, 59, 77

Kinugasa, K., & Tsunemi, H. 1999, PASJ, 51, 239

Kokubun, M., Makishima, K., Takahashi, T., et al. 2007, PASJ, 59, 53

Koo, B.-C., Lee, J.-J., & Seward, F. D. 2002, AJ, 123, 1629

Koyama, K., Awaki, H., Kunieda, H., Takano, S., & Tawara, Y. 1989, Nature, 339, 603

Koyama, K., et al. 2007a, PASJ, 59, S23

Koyama, K., Inui, T., Hyodo, Y., et al. 2007b, PASJ, 59, S221

Koyama, K., et al. 2007c, PASJ, 59, S245

Kundu, M. R., Velusamy, T., & Hardee, P. E. 1974, AJ, 79, 132

Kushino, A., Ishisaki, Y., Morita, U., Yamasaki, N. Y., Ishida, M., Ohashi, T., & Ueda, Y. 2002, PASJ, 54, 327

LaRosa, T. N., Kassim, N. E., Lazio, T. J. W., & Hyman, S. D. 2000, AJ, 119, 207

Law, C., & Yusef-Zadeh, F. 2004, ApJ, 611, 858

Law, C. J., Yusef-Zadeh, F., Cotton, W. D., & Maddalena, R. J. 2008, ApJS, 177, 255

Lazendic, J. S., Wardle, M., Burton, M. G., Yusef-Zadeh, F., Green, A. J., & Whiteoak, J. B. 2004, MNRAS, 354, 393

Lis, D. C. 1991, ApJ, 379, L53

Liszt, H. S. 1992, ApJS, 82, 495

Little, A. G. 1974, in IAU Symp. 60, Galactic Radio Astronomy, ed. F. J. Kerr & S. C. Simonson III (Dordrecht: Reidel), 491

Manchester, R. N. 1987, A&A, 171, 205

Masai, K. 1984, Ap&SS, 98, 367

Masai, K. 1994, ApJ, 437, 770

Masai, K., Dogiel, V. A., Inoue, H., Schönfelder, V., & Strong, A. W. 2002, ApJ, 581, 1071

McDonnell, K. E., Wardle, M., & Vaughan, A. E. 2008, MNRAS, 390, 49

McKee, C. F. 1974, ApJ, 188, 335

McKee, C. F., & Ostriker, J. P. 1977, ApJ, 218, 148

Mehringer, D. M., Goss, W. M., Lis, D. C., Palmer, P., & Menten, K. M. 1998, ApJ, 493, 274

Mewe, R. 1972, Sol. Phys., 22, 459

Miceli, M., Decourchelle, A., Ballet, J., et al. 2006, A&A, 453, 567

Miley, G. 1980, ARA&A, 18, 165

Mills, B. Y., Slee, O. B., & Hill, E. R. 1960, Australian Journal of Physics, 13, 676

Mitsuda, K., et al. 2007, PASJ, 59, S1

Mitsuda, K., Kelley, R. L., Boyce, K. R., et al. 2010, Proc. SPIE, 7732,

Moffat, A. F. J., et al. 2002, ApJ, 573, 191

Mori, H., Tsuru, T. G., Hyodo, Y., Koyama, K., & Senda, A. 2008, PASJ, 60, S183

Morrison, R., & McCammon, D. 1983, ApJ, 270, 119

Muno, M. P., et al. 2004, ApJ, 613, 326

Muno, M. P., Baganoff, F. K., Brandt, W. N., Morris, M. R., & Starck, J.-L. 2008, ApJ, 673, 251

Murakami, H., Koyama, K., Sakano, M., Tsujimoto, M., & Maeda, Y. 2000, ApJ, 534, 283

Nakajima, H., Yamaguchi, H., Matsumoto, H., et al. 2008, PASJ, 60, 1

Nesterov, V. V., Kuzmin, A. V., Ashimbaeva, N. T., Volchkov, A. A., Röser, S., & Bastian, U. 1995, A&AS, 110, 367

Nobukawa, M., et al. 2008, PASJ, 60, S191

Odenwald, S. F., & Fazio, G. G. 1984, ApJ, 283, 601

Ohnishi, T., Koyama, K., Tsuru, T. G., et al. 2011, PASJ, 63, 527

Oka, T., Nagai, M., Kamegai, K., Tanaka, K., & Kuboi, N. 2007, PASJ, 59, 15

Ozawa, M., Uchiyama, H., Matsumoto, H., et al. 2009, PASJ, 61, 1

Ozawa, M., Koyama, K., Yamaguchi, H., Masai, K., & Tamagawa, T. 2009, ApJ, 706, L71

Pauls, T., & Mezger, P. G. 1975, A&A, 44, 259

Radhakrishnan, V., Goss, W. M., Murray, J. D., & Brooks, J. W. 1972, ApJS, 24, 49

Reach, W. T., Rho, J., & Jarrett, T. H. 2005, ApJ, 618, 297

Reid, M. J. 1993, ARA&A, 31, 345

Reynolds, S. P. 1996, ApJ, 459, L13

Rho, J., & Borkowski, K. J. 2002, ApJ, 575, 201

Rho, J., & Petre, R. 1998, ApJ, 503, L167

Rybicki, G. B., & Lightman, A. P. 1986, Radiative Processes in Astrophysics, by George B. Rybicki, Alan P. Lightman, pp. 400. ISBN 0-471-82759-2. Wiley-VCH , June 1986.

Roberts, M. S. E., Michelson, P. F., Cominsky, L. R., Marshall, F. E., Corbet, R. H. D., & Smith, E. A. 1996, IAU Circ., 6302, 2

Ryu, S. G., Koyama, K., Nobukawa, M., Fukuoka, R., & Tsuru, T. G. 2009, PASJ, 61, 751

Sakano, M., Koyama, K., Murakami, H., Maeda, Y., & Yamauchi, S. 2002, ApJS, 138, 19

Sandstrom, K. M., Bolatto, A. D., Stanimirović, S., van Loon, J. T., & Smith, J. D. T. 2009, ApJ, 696, 2138

Sawada, M., Tsujimoto, M., Koyama, K., et al. 2009, PASJ, 61, 209

Seaton, M. J. 1959, MNRAS, 119, 81

Sedov, L. I. 1959, Similarity and Dimensional Methods in Mechanics, New York: Academic Press, 1959

Serlemitsos, P. J., et al. 2007, PASJ, 59, S9

Shaver, P. A., Salter, C. J., Patnaik, A. R., van Gorkom, J. H., & Hunt, G. C. 1985, Nature, 313, 113

Shimizu, T., Masai, K., & Koyama, K. 2012, PASJ, 64, accepted.

Shull, J. M., Fesen, R. A., & Saken, J. M. 1989, ApJ, 346, 860

Sidoli, L., Mereghetti, S., Treves, A., Parmar, A. N., Turolla, R., & Favata, F. 2001, A&A, 372, 651

Sidoli, L., Mereghetti, S., Favata, F., Oosterbroek, T., & Parmar, A. N. 2006, A&A, 456, 287

Skrutskie, M. F., et al. 1997, The Impact of Large Scale Near-IR Sky Surveys, 210, 25

Slee, O. B., & Dulk, G. A. 1974, Galactic Radio Astronomy, 60, 347

Smith, R. K., & Hughes, J. P. 2010, ApJ, 718, 583

Smith, R. K., Brickhouse, N. S., Liedahl, D. A., & Raymond, J. C. 2001, ApJ, 556, L91

Snowden, S. L., Freyberg, M. J., Plucinsky, P. P., et al. 1995, ApJ, 454, 643

Spitzer, L. 1962, Physics of Fully Ionized Gases, New York: Interscience (2nd edition), 1962

Stewart, R. T., Haynes, R. F., Gray, A. D., & Reich, W. 1994, ApJ, 432, L39

Strüder, L., et al. 2001, A&A, 365, L18

Sutherland, R. S., & Dopita, M. A. 1993, ApJS, 88, 253

Swarup, G., Gopal-Krishna, & Sarma, N. V. G. 1974, Galactic Radio Astronomy, 60, 499

Takahashi, T., Abe, K., Endo, M., et al. 2007, PASJ, 59, 35

Tarter, C. B., Tucker, W. H., & Salpeter, E. E. 1969, ApJ, 156, 943

Tawa, N., et al. 2008, PASJ, 60, S11

Townsley, L. K., Feigelson, E. D., Montmerle, T., Broos, P. S., Chu, Y.-H., & Garmire, G. P. 2003, ApJ, 593, 874

Troja, E., Bocchino, F., Miceli, M., & Reale, F. 2008, A&A, 485, 777

Truelove, J. K., & McKee, C. F. 1999, ApJS, 120, 299

Tsuboi, M., Handa, T., & Ukita, N. 1999, ApJS, 120, 1

Tsujimoto, M., Hyodo, Y., & Koyama, K. 2007, PASJ, 59, S229

Tsuru, T. G., Nobukawa, M., Nakajima, H., et al. 2009, PASJ, 61, 219

Turner, M. J. L., et al. 2001, A&A, 365, L27

Uchiyama, H. 2010, Ph.D. Thesis, Kyoto University

Uchiyama, H., et al. 2007, Proc. SPIE, 6686, 66860P

Uchiyama, Y., et al. 2008, PASJ, 60, S35

Uchiyama, H., et al. 2009, PASJ, 61, S9

Uchiyama, H., Nobukawa, M., Tsuru, T. G., Koyama, K., & Matsumoto, H. 2011, PASJ, 63, S903.

Velázquez, P. F., Dubner, G. M., Goss, W. M., & Green, A. J. 2002, AJ, 124, 2145

Wang, Q. D., Dong, H., & Lang, C. 2006, MNRAS, 371, 38

Watson, M. 2007, Astronomy and Geophysics, 48, 30

Weiler, K. W., & Panagia, N. 1980, A&A, 90, 269

Werner, M. W., et al. 2004, ApJS, 154, 1

Wolk, S. J., Bourke, T. L., Smith, R. K., Spitzbart, B., & Alves, J. 2002, ApJ, 580, L161

Yamaguchi, H., Ozawa, M., Koyama, K., et al. 2009, ApJ, 705, L6

Yamauchi, S., & Koyama, K. 1993, ApJ, 404, 620

Yamauchi, S., Kawada, M., Koyama, K., Kunieda, H., & Tawara, Y. 1990, ApJ, 365, 532

Yusef-Zadeh, F., Goss, W. M., Roberts, D. A., Robinson, B., & Frail, D. A. 1999, ApJ, 527, 172

Yusef-Zadeh, F., Law, C., Wardle, M., Wang, Q. D., Fruscione, A., Lang, C. C., & Cotera, A. 2002, ApJ, 570, 665

Yusef-Zadeh, F., Wardle, M., Rho, J., & Sakano, M. 2003a, ApJ, 585, 319

Yusef-Zadeh, F., Wardle, M., & Roberts, D. A. 2003b, ApJ, 583, 267

Yusef-Zadeh, F., Hewitt, J. W., & Cotton, W. 2004, ApJS, 155, 421

Acknowledgement

I am deeply grateful to Prof. Takeshi Go Tsuru and Prof. Emer. Katsuji Koyama for their continuous guidance and encouragement throughout the five years of my graduate school period. This thesis would not have been possible unless their supports. I also acknowledge Masayoshi Nobukawa whose meticulous comments were of enormous help.

Hiroya Yamaguchi, Midori Ozawa, Hiroyuki Uchida, Aya Bamba, Takao Ohnishi, Masahiro Tsujimoto, and Yoshiaki Hyodo gave me insightful comments and suggestions for the X-ray observational studies on thermal plasmas in SNRs and star-forming regions. I would also like to show my gratitude to Kuniaki Masai and Takafumi Shimizu for their invaluable comments on theoretical works on SNRs.

My gratitude is also for Jelle Kaastra and Jelle de Plaa for their suggestions on spectral modeling and Tomoharu Oka, Casey Law, and Crystal Brogan for providing the radio data.

I would like to thank Hironori Matsumoto, Hideki Uchiyama, Shinya Nakashima, and the XIS team for their great help on the XIS calibration. I thank all the members of the Suzaku team for their constant efforts.

I am indebted to my friends and family for their understanding and kind supports.